NEW PHOTOPLASTIC FABRICATION TECHNIQUES AND DEVICES BASED ON HIGH ASPECT RATIO PHOTORESIST

THÈSE N^{O} 2421 (2001)

PRÉSENTÉE AU DÉPARTEMENT DE MICROTECHNIQUE

ÉCOLE POLYTECHNIQUE FÉDÉRALE DE LAUSANNE

POUR L'OBTENTION DU GRADE DE DOCTEUR ÈS SCIENCES TECHNIQUES

PAR

Grégoire GENOLET
Ingénieur en microtechnique diplômé EPF
de nationalité suisse et originaire de Hérémence (VS)

acceptée sur proposition du jury:

Prof. N. De Rooij, directeur de thèse
Dr F. Marquis Weible, rapporteur
Prof. A. Stemmer, rapporteur
M. P. Vettiger, rapporteur

Lausanne, EPFL
2001

A mes parents

Abstract

This thesis deals with the development of microfabrication technologies based on photoplastic structuring by lithographic and molding techniques. These technologies, combined with an original releasing method, allow for the simple fabrication of pseudo three-dimensional, soft, photoplastic microstructures with features and shapes that are difficult to obtain with standard micromachining. The photoplastic material used is the SU-8 photoresist, a material that is used increasingly in the growing field of micro-electro-mechanical systems (MEMS). Photoplastic SU-8 microstructure fabrication is based on a combination of multi-layer spin-coating, molding and photolithographic processing of the resist on a prestructured silicon substrate. The final product is obtained by release of the structure from the substrate. This thesis describes several SU-8 microstructures which have been developed with an emphasis on atomic force microscopy (AFM) and scanning-near field optical microscopy (SNOM) probes.

Scanning probe microscopy is a well-established technique for surface analysis, but batch-fabricated, low-cost probes still remain a challenging issue. Using a polymer for the cantilever facilitates the realization of mechanical properties that are difficult to achieve with classical silicon technology. The design, fabrication and testing of single lever and cassettes of multiple single-lever probes are presented and demonstrates the potential for fabrication structures with complicated shape and features. The fabrication process for SU-8 AFM probes is a simple batch process in which the integrated tips and the levers are defined in one photolithography step. Tip radii of curvature smaller than 15 nm have been obtained. The cantilever thickness depends on the spin-coating parameters, hence it can be very well controlled over a full wafer. Photoplastic cantilevers with thicknesses ranging from 1 to 6 μm have been produced. Imaging soft, condensed matter with photoplastic levers, which uses laser beam deflection sensing, exhibits a resolution that compares well with that of commercially available silicon cantilevers. Lateral resolution of 5–6 nm has been estimated from imaging DNA-plasmid molecules. A vertical resolution of the order of 0.1 nm has been found.

A similar fabrication technique was also developed to fabricate photoplastic tips for SNOM that are to be attached to optical fibers. This technique allows optical apertures to be integrated at the end of the well-defined tip directly by probe fabrication, without the need for any post-processing for the aperture formation. Sub-100 nm aperture have been fabricated using this technique. Simple fabrication, as well as topographical and optical imaging demonstrate the potential of photoplastic-based probes for both AFM and SNOM applications, as well as for future combined probes development.

In addition, the fabrication of functional microstructures by using SU-8 processing needs to be combined with other microfabrication techniques. Simple releasing of the molded structures from the substrate is especially of great importance. A sacrificial layer technique based on electrochemical etching enhancement has been developed and combined with the fabrication of the different photoplastic SU-8 probes presented. This technique allows the fast releasing of large microstructures and has been demonstrated by releasing other SU-8 photoplastic microfabricated devices.

Résumé

Ce travail traite du développement de technologies de microfabrication basées sur la mise en forme d'un matériau photoplastique en utilisant des techniques de photolithographie et de moulage. Ces technologies, combinées avec une méthode originale de libération, permettent la fabrication de microstructures pseudo–tridimensionnelles à faible module d'élasticité ayant des éléments de tailles et de formes qui sont difficiles à obtenir avec les procédés standards de microfabrication. Le matériau photoplastique utilisé est la résine photosensible SU-8. Ce matériau est de plus en plus utilisé dans le domaine en expension des systèmes micro–électro–mécaniques (MEMS, Micro-Electro-Mechanical Systems). La fabrication de microstructures en SU-8 est basée sur une combinaison de séquences de dépôt de couches, de moulage et d'étapes photolithographiques sur un substrat préstructuré. Plusieurs microstructures en SU-8 ont été développées, avec un accent particulier mis sur les sondes pour la microscopie à force atomique (AFM, Atomic Force Microscopy) et la microscopie optique en champ proche (SNOM, Scanning-Near Field Optical Microscopy).

La microscopie à sonde proche est une technique bien établie pour l'analyse des surfaces. Pourtant, la fabrication en grande série de sondes bon marché reste un problème à résoudre. L'utilisation d'un polymère comme matériau pour le levier de la sonde facilite l'obtention de propriétés mécaniques difficiles à atteindre avec les technologies classiques du silicium. La conception, la fabrication et l'utilisation de sondes avec des leviers simples, ainsi que de cassettes contenant plusieurs leviers simples sont présentées et démontrent le potentiel de cette méthode pour la fabrication de structures avec des formes et des éléments compliqués. Le procédé qui permet la fabrication à grande échelle de sondes pour microscopie à force atomique est un procédé durant lequel les pointes et les leviers sont définis lors de la même étape photolithographique. L'épaisseur des leviers dépend des paramètres d'étalement de la résine, et peut ainsi être très bien contrôlée sur toute la surface d'un substrat. Des leviers ayant des épaisseurs de 1 à 6 microns ont ainsi été produits. L'imagerie d'échantillons biologiques avec les sondes en photoplastique montre une résolution comparable à celle obtenue avec des sondes commerciales en silicium. Une résolution latérale de 5–6 nanomètres pour une résolution verticale de l'ordre de 0.1 nanomètre a été estimée à partir d'images de molécules d'ADN.

Une technique de fabrication similaire a également été développée pour fabriquer des pointes pour SNOM devant être attachées à des fibres optiques. Cette technique permet d'intégrer des ouvertures optiques au sommet des pointes directement durant la fabrication des sondes, sans nécessiter d'étapes supplémentaires à la fin de la fabrication. Des ouvertures plus petites que 100 nanomètres ont été fabriquées en utilisant cette technique. Un procédé de fabrication simple ainsi que l'imagerie topographique et optique d'échantillons démontrent le potentiel des sondes en photoplastique autant pour la microscopie à force atomique que pour des applications liées à l'imagerie optique en champ proche.

L'utilisation de la technologie SU-8 pour la fabrication de microstructures fonctionnelles nécessite d'être combinée avec d'autres techniques de microfabrication. La libération des structures moulées, par exemple, est d'un intérêt tout particulier. Une technique de couche sacrificielle améliorée utilisant un effet électrochimique a été développée et intégrée dans la fabrication des différentes sondes en SU-8 présentées. Cette technique permet la libération rapide de grandes microstructures et a également été utilisée pour libérer du substrat d'autres structures en SU-8.

Contents

Chapter 1

Introduction

1.1 Micromachining Technologies

Microfabrication or micromachining is a key element in the development of a very large number of new technologies. It consists of many engineering disciplines which are used to create small three–dimensional (3D) structures with dimensions ranging from millimeters to nanometers, involving sensors, actuators or other microdevices or microsystems. In a narrower sense, it comprises the use of a set of manufacturing tools based on thin and thick film batch fabrication techniques derived originally from the integrated electronic circuit industry. The term micromachining broadly refers to the use of lithographic and other precision techniques to carry out such fabrication including dedicated techniques for fabricating three–dimensional free-standing structures.

Micromachining is the basis for many product innovation opportunities and their applications can lead to exciting synergies. A very broad range of devices has resulted from the use of these technologies. A large number of examples can be found in Ref. [1, 2]. Use of micromachining enabled the fabrication of devices with function and capabilities that were not possible to achieve with conventional machining. In many cases, miniaturization offers benefits that are beyond the obvious decreases of volume and weight. Increased performance, reliability and speed combined with decreased costs are some of the best-known advantages of miniaturization. High integration also provides multiple functionality for the devices. In addition, small dimensions of systems can be crucial for applications in specific fields like medicine or space exploration. Table 1.1 [3] summarizes some of the advantages of micromachining in product development.

Micromachining technologies have opened up the field to the fabrication of new and sophisticated "nanotools" of particular interest that permit one to provide a nearly indispensable bridging technology to observe, modify, or create physical or chemical interactions at the nanometer scale. Scanning Probe Microscopies (SPMs) are a good example of investigation methods and instrumentation whose developments were stimulated by micromachining techniques. This technology took advantage of the possibilities given by the reliable and well-controlled fabrication of micromachined probes. Hence, a lot of activity is being made in searching for new fabrication technologies, and in finding new applications for Micro/Nano-Electro-Mechanical systems (M(N)EMS) or micro/nanodevices. Future application development of MEMS-based products is foreseen in a broad range of fields such as Atomic Force Microscopy (AFM) based mass data storage [4], optical telecommunications networking [5, 6], parallel nanolithography [7, 8], molecular analysis [9, 10], microfluidic networks for medical testing [11, 12], and radio frequency (RF) systems [13].

1.2 Materials for Micromachining

Micromechanical structures fabricated using micromachining are primarily based on single-crystal silicon [14]. Its superior mechanical and electrical properties, combined with the existing expertise and fabrication tools in the successful and well-established silicon-based electronics industry are probably the main reasons for this dominance. General MEMS fabrication technologies

Table 1.1: Why Use Micromachining ? [3]

- Minimizing of energy and materials consumption during manufacturing
- Redundancy and arrays
- Integration with electronics, simplifying systems (e.g., single point vs. multipoint measurement)
- Reduction of power budget
- Faster devices
- Increased selectivity and sensitivity
- Wider dynamic range
- Exploitation of new effects through the breakdown of continuum theory in the microdomain
- Cost/performance advantages
- Improved reproducibility
- Improved accuracy and reliability

distinguish between *bulk micromachining* and *surface micromachining*, depending on the way the material is structured. Bulk micromachining relates to processes which typically craft device components from the bulk of the silicon wafer. Bulk micromachining is mainly concerned with single crystal silicon, as this is the dominant substrate material. This technique exploits differences in etch rates between the crystallographic directions of silicon and various wet etchants to form features that follow crystal planes [15], anisotropic high etch rates during plasma etching [16], and silicon electrochemical etching [17]. Surface micromachining refers to processing "above" the substrate, using the latter more as a support or anchor than as a structural material. The cycle of deposition, patterning and etching of each material can be repeated several times to build up multilayer structures with a wide variety of feature shapes. Either of these two methods presents its own set of advantages and disadvantages which need to be weighed in any particular application. Additive films and materials to be deposited on the substrate for subsequent surface micromachining can be formed from conductors, semiconductors or insulators. Possible materials include a large variety of species: silicon (single crystal, polycrystalline, amorphous), silicon compounds (Si_xN_y, SiO_2, SiC, etc.), ceramics (Al_2O_3, PZT, etc.), metals (Au, Cu, Cr, Ni, Al, etc.), organics (polymers, diamond, DNA, etc.). As devices become more complex and are made from multiple components, both bulk and surface micromachining fabrication techniques are combined. Nevertheless, microstructures obtained using standard micromachining of classical materials usually have some limitations in their shape and size. In particular, surface micromachined mechanical parts are usually limited to a few microns in thickness when using thin film materials deposited onto the silicon substrate [18]. On the other hand, bulk micromachining usually involves long etching times to remove large parts of the substrate, and adds handling and structuration complexity (e.g. double side processing). As it will be described later, photoplastic structuring turns out to be a good alternative for surface micromachining of thick layers (several 100-μm) using simple processing, in addition to being a material with interesting mechanical properties.

1.3 Plastic Micromachining

Due to the expanding interest in microsystem techniques, today's trend is towards the exploration of non-silicon based materials and combinations of materials allowing more freedom of device design. Novel materials and processes are getting more attention, driven by the prospects of new sensor and device concepts together with possibly cheaper manufacturing processes [19]. Moreover, micromechanical structures with a high degree of three dimensionality, or HARMS (High Aspect Ratio Microstructures) are desired for many applications, but are very difficult to fabricate with standard micromachining techniques. LIGA (LIthographie, Galvanoformung and Abformung) [20] is a technique developed in the 1980's allowing creation of highly three dimensional structures with aspect ratios as high as 100:1, using x-ray lithography. This approach has not made its way into large scale industrial applications, mainly because of the very expensive synchrotron source needed to expose the photoresist mask. However, recently developed low-cost optical lithography based LIGA with interesting aspect ratios looks to be a very promising approach for many practical applications, allowing low-cost HARMS technology to evolve. It uses thick photoresist as mold for electroplating with no need of an x-ray source. One form of this technique is based on a novel, near–ultraviolet–sensitive resist technology that allow fabrication of high (up to 20:1) aspect ratio structures with standard lithography tools [21]. The photoresist used in this technique is the negative-tone, near–ultraviolet–sensitive epoxy-based EPON® SU-8 [22]. The main drawback of this technology is that it is very difficult to remove the crosslinked resist, so that its success for through mask plating is limited. On the other hand, it turns out that this resist is a very promising material for microstructures due to its good mechanical, thermal and chemical stability. Hence, low-cost micromechanical structures with sub-micrometers features can be fabricated using this resist and standard photolithography steps. Combined with appropriate sacrificial layer techniques, 3D microstructures can be batch fabricated on a wafer-scale, and then released from the substrate. The low Young's modulus of this resist makes it especially suitable for mechanical structures where low-stiffness parts with non-critical dimensions are needed such as AFM cantilever probes. This SU-8 technology establishes a intermediate solution and find a niche between the low-cost, high volume fabrication provided by injection molding and the fine, controlled features characteristic given by silicon technologies.

1.4 Outline of the Thesis

The purpose of the present thesis is to explore the possibilities given by the SU-8 photoresist as structural material for fabricating micromechanical devices. Simple photolithographic steps combined with other silicon technologies can be used to fabricate plastic microstructures with nanometer features and complicated shapes that are not possible or at least much more difficult to achieve with standard silicon technologies. This work will focus on the technology development for fabricating and release such SU–8 based microstructures on a wafer-scale. The expertise in the fabrication of probes for scanning force microscopy, as well as the pioneering developments of SU-8 for MEMS at the IBM Zurich Research Laboratory naturally lead towards an investigation for the fabrication of such probes in SU-8.

SU-8 photoresist is presented in *Chapter 2*. Its processing and properties are discussed with an emphasis towards its use as structural material. Advantages and limitations are examined from a manufacturing perspective.

For the fabrication of functional microstructures, SU-8 processing needs to be combined with other microfabrication techniques. Sacrificial layer techniques that allow the simple releasing of a fabricated structures from a substrate without excessive complications are especially of great interest. Centimeter-size structures are, however, very difficult to lift-off with conventional sacrificial techniques. An enhanced sacrificial layer technique developed for the general releasing of microstructures fabricated with thick layers of add-on materials such as SU-8 on a substrate is introduced in *Chapter 3*.

Chapter 4 starts with a basic description of atomic force microscopy (AFM) principles. A brief history of probes for scanning force microscopy demonstrates how micromachining was one of the key technology in the fast development of this field, allowing the transition from hand–made to batch–fabricated, reliable probes. Entire SU-8 photoplastic probes for AFM are then presented. Design, fabrication and characterization of such probes are described. Advantages and drawbacks of plastic probes versus conventional probes are discussed.

Chapter 5 deals with a more advanced SU-8 probe for scanning force microscopy. A cassette of cantilevers is described, which demonstrates the possibilities of this material for fabricating structures with complicated shapes. A cassette of cantilevers allows spare cantilevers to be integrated on the same chip as the one used to scan the sample. The design, fabrication and testing of this device is presented.

Chapter 6 reports on the use of SU-8 technology for the fabrication of a microfabricated probe for scanning near-field optical microscopy (SNOM). The technique presented, micromachining combined with the sacrificial layer described in chapter 3, allows the well-controlled and batch fabrication of probes with integrated apertures so that no post-processing is needed. Design, fabrication and testing of such probes are reported.

Besides probes for SPM, other microstructures can also be fabricated using SU-8 technology. Some of such devices are presented in *Chapter 7*.

Chapter 8 concludes this work. Results obtained in the previous chapters are considered in view of possible further developments and new applications.

Chapter 2

SU-8 Photoplastic Material

2.1 Introduction

The material used to fabricate the photoplastic microstructures is SU-8, an epoxy-based, negative-tone, near-UV sensitive photoresist invented and developed at IBM Research [22, 23, 24]. The development of this material was triggered by the increased activity in micromachining and the need for high aspect ratio thick film resist systems. High aspect ratio lithography on ultrathick resist ($> 50\ \mu$m) has shown added dimensionality and flexibility in the design and building of tall, high aspect ratio microstructures for micromachine and packaging applications. An example of this is the X–LIGA process where very high aspect ratio microstructures are built by electroplating onto a very thick polymethylmethacrylate (PMMA) template patterned by synchrotron x–ray lithography. It has also been demonstrated that SU-8 has great potential for high aspect ratio (up to 20:1) and tall (millimeter height) structures with standard UV contact lithography [21]. Hence, this photoplastic material is used increasingly in the growing field of MEMS as a photoresist for low-cost LIGA applications, as well as a structural material [25]. The high thermal stability of fully cured SU-8 allows it to be used as a mask for prolonged reactive-ion etching (RIE) [23]. In micromachining, SU-8 has been used as template for nickel electroplating [26, 27], in the fabrication of planar embedded copper coils [28], as material for shaped spacers in miniature electrochemiluminescence and micro-enzymatic reactors [29], and for the fabrication of three-dimensional, submillimeter wave components [30]. SU-8 multilayer structures used in UV-LIGA have also been combined with microstereolithography for the addition of more complicated features [31]. SU-8 embedded micro-channels have been fabricated using multilayers of the photoresist [32] or by direct writing with proton beams of different exposure doses [33]. In addition, SU-8 photoresist structures with aspect ratios as high as 100:1 have been demonstrated using x-ray lithography [34].

In addition, SU-8's small Young's modulus, and the associated new design space this allows, makes this photoresist a very promising material for the fabrication of plastic micromechanical structures where a high compliance is required. We will see that this material is well-suited for the simple, low-cost fabrication of photoplastic AFM probes with integrated tips (see chapter 4). The possibility of combining SU-8 technology with standard silicon technology also allows more complex devices such as photoplastic-based SNOM probes with integrated optical apertures to be batch fabricated (see chapter 6).

2.2 Properties

2.2.1 SU-8 Composition

SU-8 is a negative-tone, epoxy-type, near-UV photoresist. It is prepared from commercially available components by dissolving an EPON® SU-8 resin (from Shell Chemical) in an organic solvent like γ-butyrolacton (GBL). The quantity of the solvent determines the viscosity which permits the range of the possible resist thicknesses to extend from tens of nm to mm. The resin is photosensitized with triaryl sulfonium salt (e.g. CYRACURE® UVI from Union Carbide, 10 % of the EPON SU-8 weight). The SU-8, with eight epoxy sites per monomer, is the photoresist with the highest epoxide functionality per molecule commercially available, Figure 2.1.

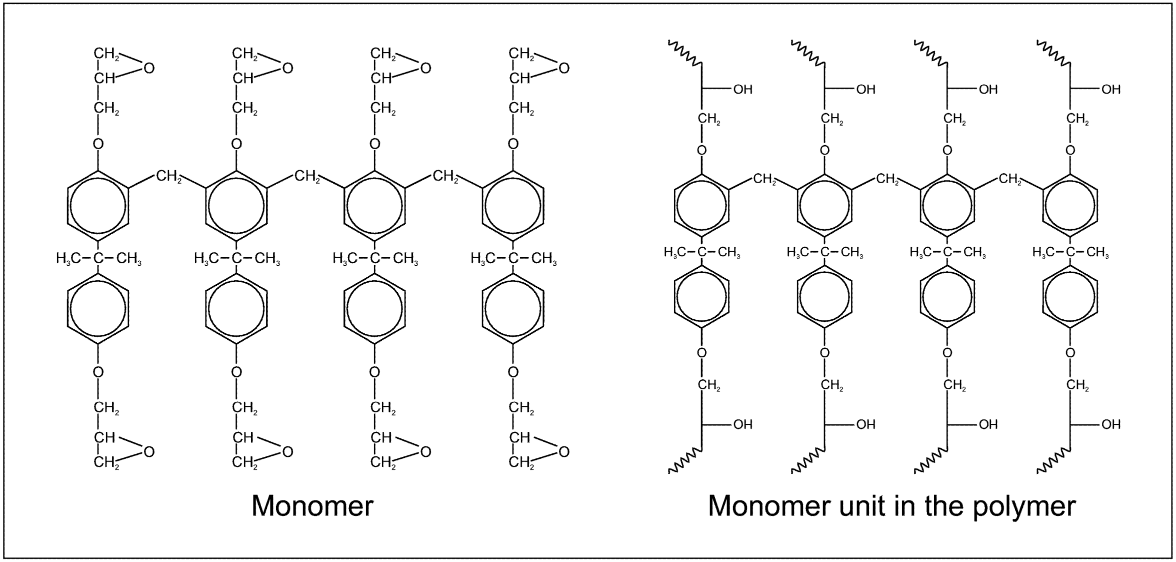

Figure 2.1: *Molecular structure of EPON SU-8. The monomer and the monomer unit in the crosslinked polymer are shown.*

The highly crosslinked structure induced by ultraviolet exposure gives SU-8 its high thermal stability and good chemical resistance. In the crosslinking process, the epoxide monomers, stimulated by the curing agent, are transformed from a low-molecular weight melt to a highly crosslinked network.

2.2.2 Chemical Reactions in SU-8

Polymerization of SU-8 is based on chemical amplification. A single photo-event, also known as protolysis, initiates a cascade of subsequent chemical reactions that induce the crosslinking. The chemical reactions in SU-8 involve the use of a cationic photoinitiator (triaryl sulfonium salt), which generates a strong acid upon UV-exposure, as shown in Figure 2.2(a). This photoacid acts as a catalyst in the subsequent crosslinking reaction that takes place during a post-exposure bake step. The crosslinking is initiated by the cationic ring opening of epoxy groups by the acid, Figure 2.2(b). The acid is not consumed in the initiation process and can function to initiate several chains. The crosslinking process yields a dense, stable network where each epoxy monomer is connected to 7 others on the average.

2.2.3 SU-8 Physical Properties

As a material, SU-8 material has been extensively investigated. The most interesting mechanical and chemical properties for the fabrication of microstructures are summarized in Table 2.1. The photoinitiator in SU-8 photoresist has peaks of UV light absorption at 310 nm and 230 nm. Hence, protolysis occurs in the wavelength range of conventional broadband mask aligners.

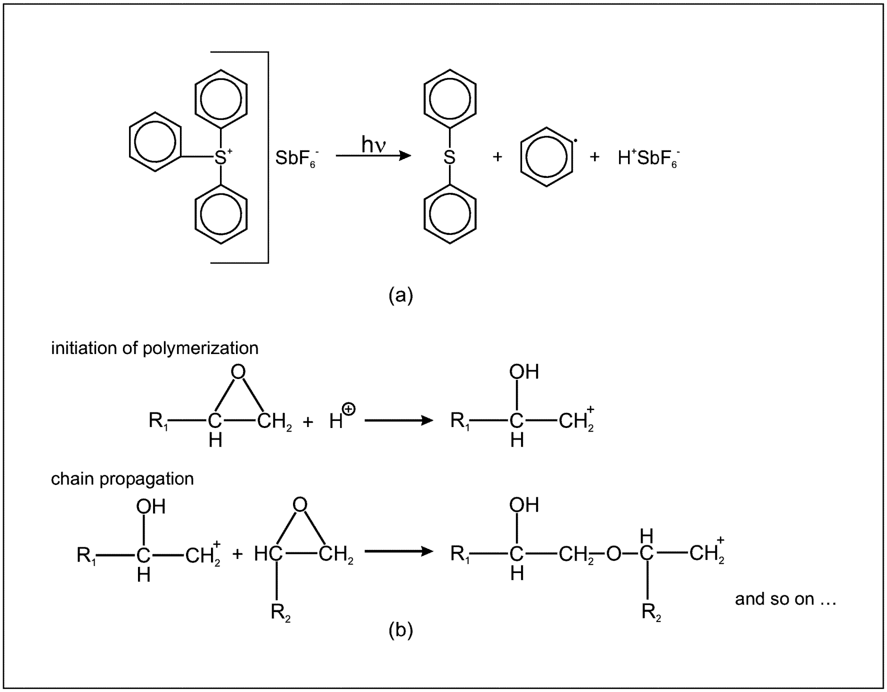

Figure 2.2: *(a) Protolysis of the triaryl sulfonium hexafluorantimonium which generates an acid that induces the crosslinking. (b) Opening of the epoxy group and reaction propagation.*

Table 2.1: Physical Properties of SU-8 Photoresist

Property	Value	Ref.
Young's Modulus E	4.02 GPa (Postbake @ 95°C)	[35]
	4.95 ± 0.42 GPa (Hardbake @ 200°C)	[36]
Bi-axial Modulus of Elasticity $E/(1-\nu)$	5.18 ± 0.89 GPa	[37]
Film Stress	16–19 MPa (Postbake @ 95°C)	[37]
Max. Stress	34 MPa (Hardbake @ 200°C)	[36]
Friction Coefficient μ	0.19 (Postbake @ 95°C)	[35]
Glass Temperature T_g	$\sim 50°C$ (unexposed)	[22]
Glass Temperature T_g	$> 200°C$ (fully crosslinked)	[22]
Degradation Temperature T_d	$\sim 380°C$ (fully crosslinked)	[22]
Thermal Expansion Coefficient TEC	52 ± 5.1 ppm/K (Postbake @ 95°C)	[37]
Polymer Shrinkage	7.5 %	[32]

2.3 SU-8 Processing

2.3.1 Introduction

SU-8 photoplastic material is processed as a negative photoresist with an additional post-exposure step where crosslinking occurs. Processing steps include spin-coating, prebake, exposure, post-exposure and development performed as shown in Figure 2.3. For multilayer structuring, spin-coating of additional layers can be performed after post-exposure bake or development of the previous layers. Post–development spin-coating is limited by the topography present in the previous layers.

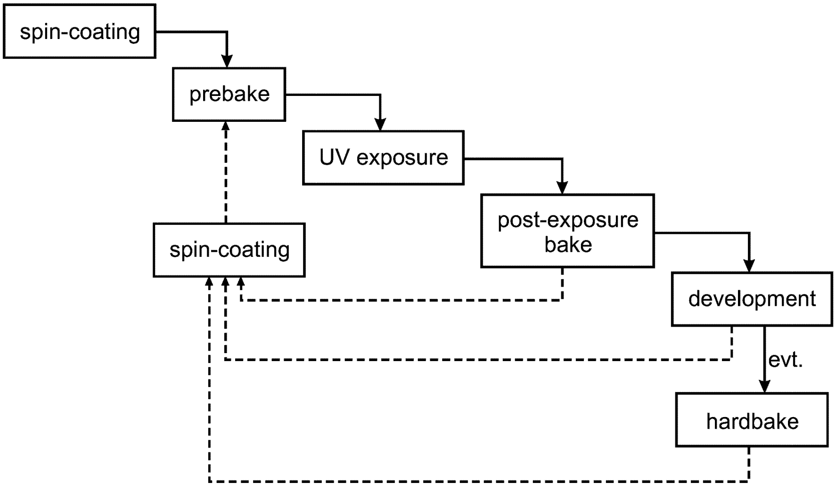

Figure 2.3: *Schematic of the processing steps for SU-8 technology. Dash lines show alternatives for multi-layers spin-coating. Hardbaking is not a mandatory step.*

2.3.2 Spin-Coating

SU-8 is spun in thickness ranges determined by the viscosity of the resist and by the spin-coating parameters of speed and time. For thick layers, final thickness also depends on the quantity of photoresist initially placed on the substrate. In order to obtain reproducible results for the work in this thesis, the same amount of material was used for every wafer. A quantity of 4 ml for a 4–in. Si wafer was used.

Thick layer spin-coating produces an edge bead which degrades the contact conditions between mask and resist during exposure. This edge bead can be minimized by leaving the wafer for more than 10 min on a leveled surface at room temperature, just after spin-coating and before prebaking. The solvent present in the resist causes a reflow of the material and reduces the edge bead. The edge bead can also be eliminated by using a dedicated edge bead removal step.

2.3.3 Prebake (PB)

Baking is necessary for removing solvent from the resist layer after spin-coating. Prebake (PB) is performed on a hotplate at a temperature of $95°C$. PB time depends on the thickness of the SU-8 layer. For 5-μm thick SU-8, a 6–min prebake time is sufficient. For a 200-μm thick layer, 3 h are needed. Experiments have shown that overbaking is much less critical than underbaking. For very thick layers, a combination of heating with a hotplate and an infra-red (IR) lamp has given the best results. As PB temperature of SU-8 is greater than the glass transition temperature, reflow of the resist occurs during the first minutes of the PB. This reflow is important for reducing the edge bead. Hence, it is very critical to have a leveled hotplate in order to produce smooth, uniformly coated substrates.

2.3.4 Exposure

Exposure to UV-light induces crosslinking of the SU-8 photoresist. The exposure is done using a broadband mask aligner with soft or low-vacuum contact modes. The exposure time is calculated using the intensity value of the 365-nm spectrum line of the mask aligner. The exposure dose depends on the layer thickness. Overexposure is not very critical for microstructure fabrication: it has only the small influence of broadening the size of the final structures.

2.3.5 Post-Exposure Bake (PEB)

SU-8 crosslinking occurs during the post–exposure bake (PEB) only in regions that contain acid catalyst generated during exposure. The bake is necessary because very little reaction can take place in the solid state where molecular motion is effectively frozen. PEB must be carried out at temperatures greater than T_g (about $55°C$ in the solid resist film) in order to be effective. As crosslinking occurs, the resist film properties will change in several ways: some shrinking will occur due to densification during crosslinking formation and outgasing of the solvent, and T_g will rise as the film becomes increasingly crosslinked. As crosslinking proceeds and the network gradually approaches completion, the crosslinking reaction will slow down and eventually stop. Thus, the final T_g of the material is dependent on the PEB temperature. Typically, PEB is performed on a hotplate at a temperature of $95°C$ for 15 min. To minimize internal film stress, the wafer is slowly heated to PEB temperature; cooling is performed by a slow temperature ramp to $70°C$.

2.3.6 Development

Photoresist development is performed in propylene glycol methyl ether acetate (PGMEA). Reduced developing time and increased efficiency is obtained by agitation. Development is terminated with a short dip in a fresh bath of PGMEA to remove residues. Spray and puddle techniques can improve drastically the development efficiency, especially for deep trenches. Final rinsing is done with isopropanol. Figure 2.4 shows a developed tubular SU-8 structure on a silicon substrate. Controlled processing can lead to structures with well-defined, near-vertical sidewalls.

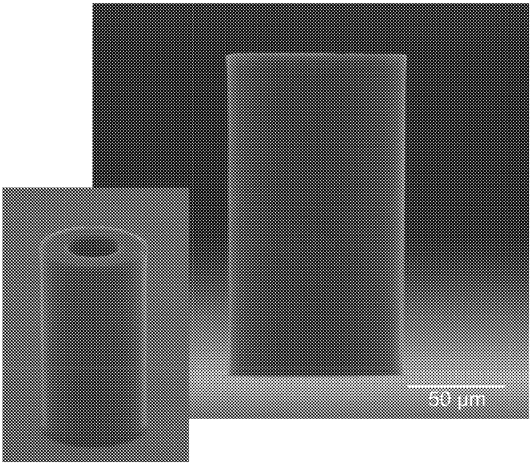

Figure 2.4: *SEMs of a fabricated SU-8 tubular structure. The height of the structure is 160 μm, the external diameter is 92 μm on top, and the hole diameter is 45 μm. Controlled processing leads to a structure with near-vertical sidewalls. The structure has an angle with the substrate of ∼90.5°.*

2.3.7 Hardbake (HB)

A post baking step of the developed structures in an oven at $200°C$ will lead to very hard material. Crosslinking can continue until total completion. This step has to be performed carefully, because high temperature build strong internal stress. After hardbaking, stress due to resist polymerization is negligible, but the stress introduced by the difference between the linear thermal expansion coefficients of the substrate and the resist during hardbake treatment is significant. In this thesis, this step was done only for thin layers (< 10 μm). Figure 2.5 shows the time evolution of the stress after hardbaking

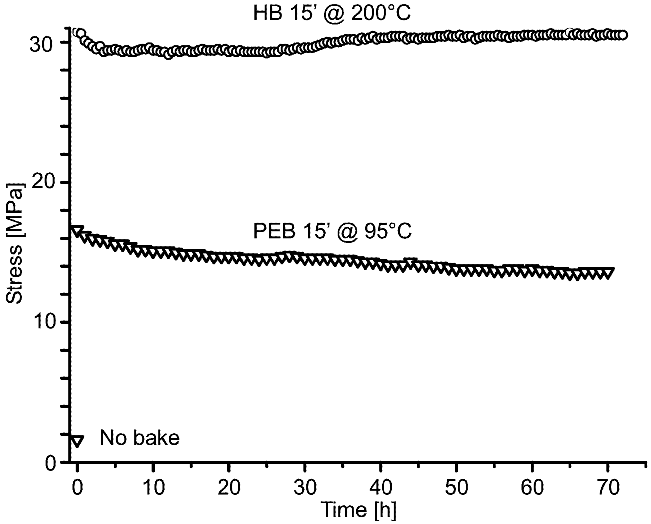

Figure 2.5: *SU-8 stress time monitoring. After PEB @95°C for 15 min, a stress of 16.6 MPa has been measured. After 72 h, stress relaxation occurred and a remanent stress of 13.6 MPa was measured. After HB @200°C for 15 min, monitoring of the stress during 72 h showed no relaxation, demonstrating that polymer was fully cured. Values of 30±0.8 MPa have been found.*

of a 7-μm thick SU-8 layer on a 4–in. Si wafer at 200°C for 15 min. Stress was measured using a Tencor FLX-2320 thin film stress measurement system at room temperature. A slight relaxation is visible in the first few hours, but no further relaxation of the stress is visible after 72 h. This demonstrates that SU-8 is fully cured after 15 min of HB. A value of 30±0.8 MPa has been determined for the stress after HB. On the other hand, stress relaxation occurs after PEB (15 min @ 95°C) when no HB is performed. In this case, SU-8 is not fully crosslinked and polymer chains can rearrange themselves to release internal stress. A stress of 16.6 MPa has been measured directly after PEB, while of stress of 13.6 MPa was observed after 72 h.

2.3.8 Stripping

Crosslinked SU-8 is insoluble in most chemicals and therefore very difficult to remove. Several alternatives have been proposed, but no universal solution has been found. Long etching time, high temperature, poor selectivity or use of non-standard or hazardous chemicals are the main problems encountered. Hot NMP (1-methyl-2-pyrrolidone), nitric acid (100 %) or piranha (H_2O_2 : H_2SO_4) have been used to dissolve SU-8, with mixed results. A high pressure water jet is a mechanical solution which gives good results but needs to be well controlled and is not applicable to fragile devices. Other techniques include oxygen/fluorin plasma etching [26] or KrF excimer laser micromachining [38]. In this work, the stripping problem is bypassed by using the SU-8 as the structural material.

2.3.9 Acidic Diffusion

In advanced chemically amplified systems, the photolithographic performance is strongly influenced by diffusion of acid and base additives [39]. In multilayer SU-8 processing, diffusion of the catalytic acid plays a role in dimension control. Acid generated in the exposed regions can diffuse into the non-exposed regions and induce undesired crosslinking. This acidic diffusion leads to an increase in the dimension of the underlying structures and is determined by the process conditions. For SU-8, the long prebaking time for thick layers is a dominant cause of acidic diffusion.

For AFM probes, the final thickness of the cantilever may be different from the thickness measured after structuring the lever layer. Acidic diffusion during prebaking of the chip body may induce an increase of this first layer. In order to determine the thickness increase of the lever layer, a 5-μm thick layer was spin coated, exposed, post-exposure baked, developed and hardbaked. After HB, the thickness was measured with a profilometer. A thick SU-8 layer was then spin coated and prebaked for different times. After removal of this layer, the lever thickness was measured. This experiment showed that cantilever thickness increased slightly, but by an amount not greater than 900 nm, even after 6 hours baking time. In fact, the maximum diffusion was reached after 30 min of baking, and little change was observed after that. It was observed that this thickness increase depended on the structure of the original layer.

2.4 Photoplastic Microstructures Fabrication

Microstructures fabricated using SU-8 as a material are based on the spin-coating, exposure and development of this photoresist on a substrate. Figure 2.6 shows a basic outline for the fabrication of a 3-level SU-8 microstructure. The first SU-8 layer is spin coated onto the substrate. After mask exposure and post-exposure bake steps, a second layer is spin coated, exposed and post-exposure baked. These steps are repeated for the remaining layers forming the microstructure. Non-exposed SU-8 is then removed during a development step prior to releasing of the microstructure. In Figure 2.6, development is made after all layers have been exposed. This is not a requirement when structuring thin layers. If thick layers are structured, it is better to develop the photoresist at the end so that new–layer spin–coating occurs on a planar surface, instead of on the topography of a developed layer.

Free-standing structures (e.g. cantilevers) can be obtained by turning the released structure upside down. The feasibility of complex photoplastic microstructure fabrication is demonstrated by making cantilever arrays. Levers are first lithographically defined on the substrate, while the chip body is formed by a second, thicker layer on top of the first one. Figure 2.7 shows SEMs of a fabricated two-level SU-8 microstructure after release from the substrate. They are composed of a 2 × 8 array of levers attached to a holding part.

SU-8 microstructures fabricated using the add-on method described in Figure 2.6 are made by adding smaller parts onto larger surfaces in the x-y plane. Fabrication of direct overhanging structures is possible by depositing a metallic layer onto unexposed photoresist to avoid irradiation of the underlaying resist during exposure. Development of the layers followed by a planarization step with a non-photosensitive material (e.g. SU-8 without

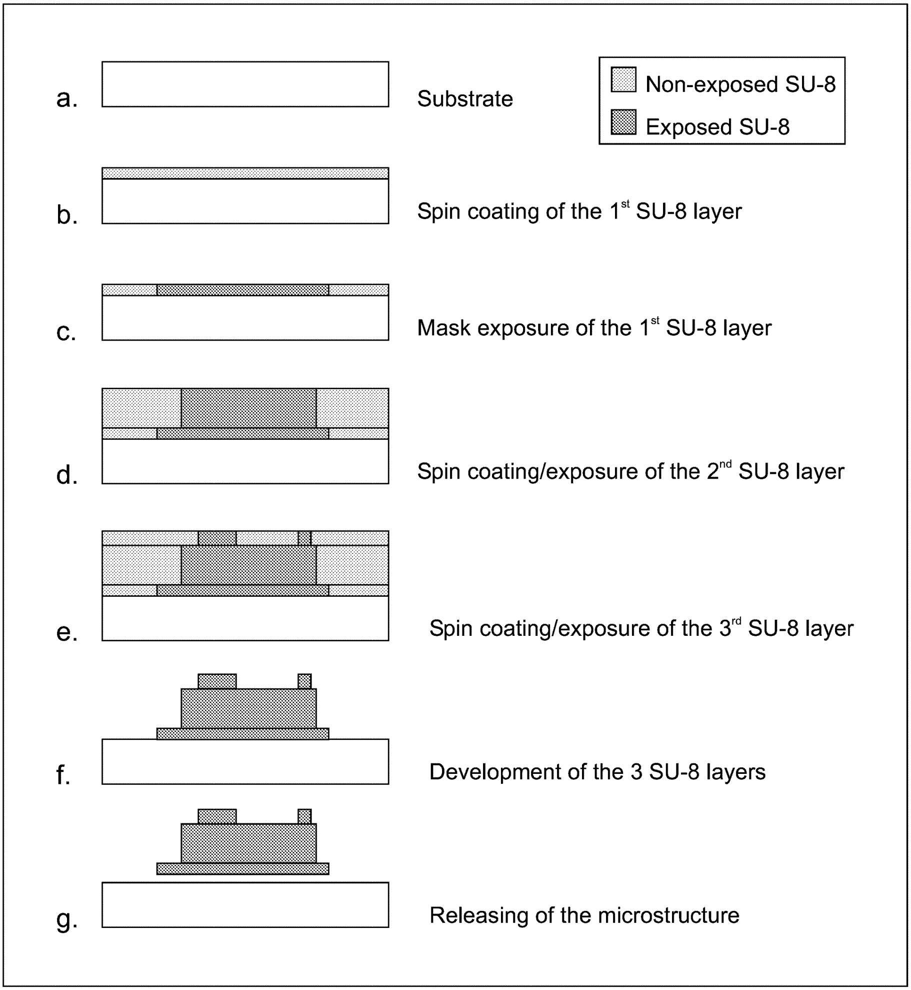

Figure 2.6: *Basic process for the fabrication of a multi-level SU-8 photoplastic microstructures. Fabrication is based on the building up of structured layers prior to releasing.*

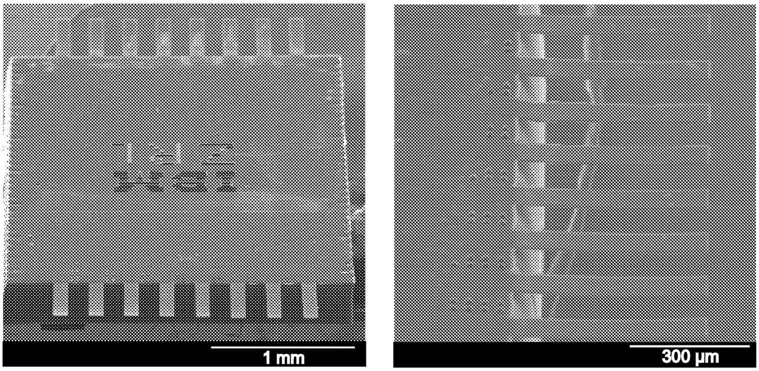

(a) **(b)**

Figure 2.7: *SEMs of fabricated SU-8 photoplastic cantilever arrays. Levers were first defined on the substrate. Thickness, width, and length of the levers are 5, 100, and 500 μm, respectively. Chip body is 2.5 mm × 3.5 mm, and 300 μm thick.*

photoinitiator) before spin-coating of the next layer is also a solution that has been proposed to fabricate embedded SU-8 microchannels [32]. Direct write using proton beam exposure with different exposure doses also allows the fabrication of multi-level microstructures with direct overhanging parts from a single SU-8 layer [40].

Chapter 3

Enhanced Sacrificial Layer

3.1 Introduction

In MEMS fabrication, a common process involves the use of sacrificial (or temporary) layers to realize free–standing structures or to release structures from the substrate. A structural layer is deposited on top of an already deposited sacrificial layer. Subsequent chemical wet or dry etching techniques with high selectivity between the structural and the sacrificial layer are used to remove the sacrificial material. Etching of silicon dioxide as a sacrificial layer in order to release the mechanical parts of sensors and actuators is a very common surface micromachining technique [118]. Different types of metallic sacrificial layers have also been used, such as titanium, aluminum, copper and chromium [119, 120, 121]. Use of conventional photoresists as a sacrificial layer has also been reported [122]. They provide a low–cost, easy to coat, easy to dissolve alternative, but limit the processing possibilities of further fabrication steps. Processes which are based on polymer sacrificial layers and dry release in oxygen plasma have recently been introduced [123, 124]. An advantage of the dry–release step is the elimination of any sticking problem which can occur with wet release methods during drying. Unfortunately, in order to get high underetching rates, a high power, high pressure plasma is needed, which leads to relatively high temperatures and thus limits the application range.

Sacrificial layer techniques are also used in the particular case where microstructures need to be completely detached from the substrate. Standard sacrificial layer techniques rely on isotropic etching, so that lateral underetching of the microstructure depends strongly on the thickness of the sacrificial layer. In general, long etching times are needed, which can lead to the risk of corroding the device to be released. This is even worse in the case of thin sacrificial layers where diffusion issues reduce the underetching efficiency. A solution for the lifting–off of large microstructures is provided by diffusion etch holes etched through the device to be released which help underetching. Porous sacrificial layers such as porous silicon material have proven to be a useful sacrificial layer material when long etch distances are needed due to a fast etching rate [125]. Hence, a combination of porous silicon etching and diffusion etch holes has allowed the underetching of mm-sized microstructures [126]. In the particular case of photoplastic microstructures, photoresist sacrificial layers which are easy to dissolve are very difficult to use due to the long baking times occurring during SU-8 processing. In addition, the outgasing of remaining solvent in the sacrificial photoresist damages photoplastic devices.

An alternative for microstructure releasing is based on the reduction of adhesion at the interface between device and substrate. Lifting-off is then simply performed by pulling off the device. Self–assembled monolayers (SAMs) have been proposed as anti–adhesion coatings to assist the removal of photoplastic microstructures [127]. However, control of the specific adhesion level at an interface is difficult because adhesion must, on the one hand, be good enough for processing the structure before lift-off, and, on the other hand, still be weak enough to enable releasing of the structure. Moreover, specific adhesion control is extremely sensitive to process parameters. Figure 3.1 shows an attempt to use an intermediate, structured, thin teflon (PTFE) layer for anti–adhesion between silicon dioxide and SU-8. The anti–adhesion property of teflon is so large that it has even been impossible to subsequently spin coat an homogeneous layer of SU-8 onto the wafer. SU-8 has remained confined in regions where no teflon had been deposited, preventing further processing.

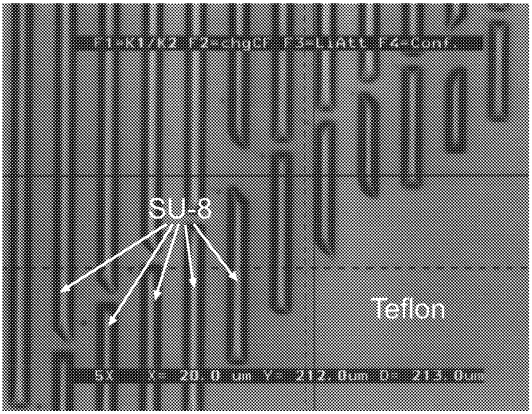

Figure 3.1: *Use of a teflon layer as anti–adhesion layer. Optical micrograph of a zone of a wafer with a prestructured teflon layer and SU-8 photoresist. Spin coated SU-8 does not remain on the substrate where teflon is present. It is confined in locations where no teflon has been deposited.*

In order to release large photoplastic microstructures, a sacrificial layer technique where the sacrificial layer is rapidly etched over long distances has been developed.

3.2 Enhanced Sacrificial Layer

3.2.1 Overview

The Enhanced Sacrificial Layer (ESL) technique permits the release of large microstructures from the substrate in a short time, without the need of diffusion etch holes. It is based on an electrochemical etching enhancement technique, but without the need for an external power supply source [128].

The enhanced etching is provided by means of an electroetching produced by a natural galvanic cell formed at the sacrificial layer interface. In addition, the thickness of the sacrificial etch layer can be arbitrarily set from about 20 nm to as thick as needed for controlling structure gaps. The technique allows the release of several millimeter–large, arbitrarily shaped structures .

In standard sacrificial layer etching, the initial etch velocity may slow down due to diffusion limitations. The first-order reaction kinetics is generally described by the Deal–Grove model. The overall reaction is divided into diffusion of the reactants and products to and from the proceeding etch front, and the chemical reaction itself, taking place at the etch front. The diffusive flux J_{diff} is proportional to the concentration difference in reacting species inside and outside the etch channel, thus

$$J_{diff} = D\frac{C_b - C_s}{\delta} \tag{3.1}$$

where C_b and C_s are the reactant concentration at the bulk and the surface, respectively, D denotes the diffusion coefficient and δ the underetched distance. In steady–state, J_{diff} equals the reaction rate providing the substance exchange required for the etching. For a long underetched distance δ, the concentration difference $C_b - C_s$ can be very small due to the difficulty of providing fresh etching solution to the interface.

The concept underlying the ESL process is shown in Figure 3.2. ESL is composed of two metals with a high electronegativity difference, forming the anode and the cathode of an internal battery cell when dipped in an electrolyte. Induced voltage produces an additional driving force supplied to the reactants at the interface of the sacrificial layer and the etchant. Hence, this anodically driven etch process is not inherently diffusion limited. Moreover, the internal battery provides a high corrosion current, enabling the sacrificial anode to be etched much faster than under normal conditions. The electrolytic corrosion occurring at the interface and in the channel is in general very complicated and is in need of further study. However, the concept underlying ESL is fairly general and a number of different etchant and sacrificial layer systems can be developed to exploit this effect.

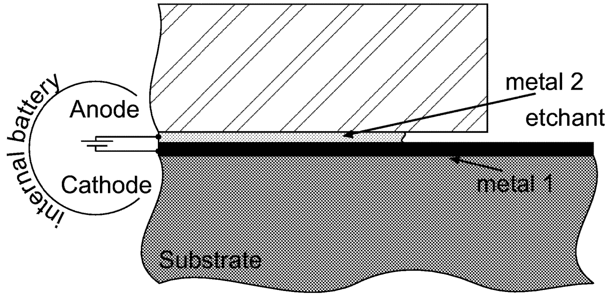

Figure 3.2: *Concept of ESL. The sacrificial layer is composed of two metals with a high electronegativity difference. They form the anode and the cathode of an internal battery. This battery provides an increased corrosion current, allowing the anode to be etched much faster.*

3.2.2 ESL Characterization

The sacrificial layer used for the releasing of photoplastic microstructures is composed of a 50–nm thick Au layer for the cathode on top of which a 20–nm Cr layer which plays the role of the anode. A 5–nm thick Cr layer was first deposited onto the substrate to enhance Au adhesion. Both metals were deposited on a 4–in. Si wafer using a magnetron sputtering technique. Etching behavior was monitored by measuring the underetching of thin SU-8 structures fabricated on top of the Cr layer. Figure 3.3 displays the underetching length of 1–μm thick SU-8 structure using the above mentioned ESL, compared to the underetching using a single 20–nm thick Cr sacrificial layer. Etching was performed in cer(IV)ammoniumnitrat–based chromium etchant[1]. Underetching was measured with an optical microscope through the transparent SU-8 layer. An etch rate of the Cr in the Au/Cr combined

---

[1] This Cr etchant is composed of 1000 ml H_2O, 200 g $Ce(NH_4)_2(NO_3)_6$, 35 ml acetic acid.

layer of ~35μm/min has been found, compared to only ~170 nm/min for Cr alone. The Au/Cr combination layer gives an underetching enhancement factor of ~200. It should be noted that the normal etch rate for Cr in the etchant used is ~100 nm/min. Hence, the Cr layer seems to be etched by more than the side of the channel. We suspect that the Cr/SU-8 interface etches slightly faster due to adhesion reduction at the etching interface.

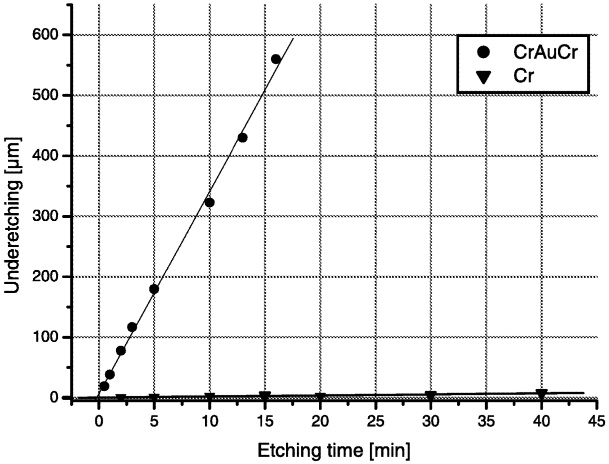

Figure 3.3: *Etching comparison of Cr and Au/Cr sacrificial layers. Underetched structures are formed by a 1-μm thick SU-8 layer. In this case, the Au/Cr layer provides an etching rate enhancement for the Cr of about 200 times.*

As described in paragraph 2.3.7, SU-8 layers are subject to stress. Tensile stress of 30 MPa has been found for hardbaked SU-8 layers (see Figure 2.5). The magnitude of the intrinsic force tending to pull the photoplastic microstructure off the substrate is dependent on the layer thickness. This lifting–up force tends to give better access to the etching solution: reduced adhesion provides a larger sacrificial surface area in contact with the etchant. Hence, thicker photoplastic microstructures are more quickly underetched and released. Figure 3.4 demonstrates the effect of the SU-8 thickness on underetching. A 1–μm thick and a 7–μm thick SU-8 layer have been structured and underetched. An etch rate of ~35μm/min for the 1–μm thick SU-8 layer and an increasing etch rate of 100–150 μm/min for the 7–μm thick layer was found.

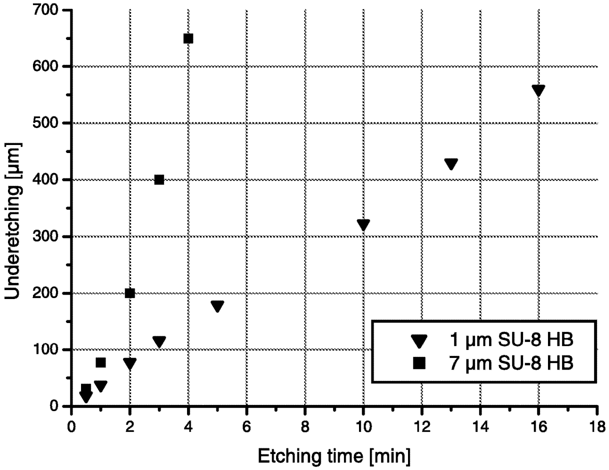

Figure 3.4: *Effect of the intrinsic stress in the layer to be underetched on the etching behavior. Pulling force is larger for thicker SU-8 layers resulting in a much faster underetching of the structure.*

ESL is a wet etching process. Despite the very fast microstructure underetching, it remains a controlled isotropic process. The isotropy of ESL is shown in Figure 3.5. Etching has been stopped before complete etching of the sacrificial Cr.

3.3 Conclusions

The enhanced sacrificial layer technique has proven to be essential for the complete releasing of microstructures. It consists of simple metallic layers undergoing electrolytic corrosion which can be easily deposited on a wafer level.

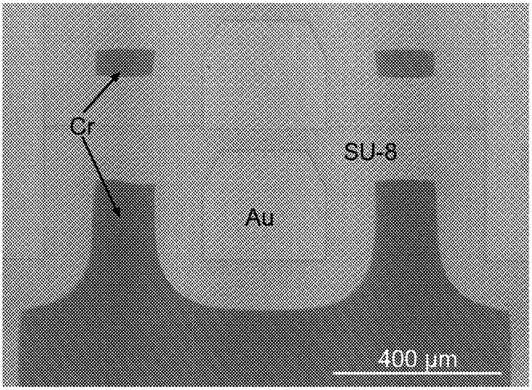

Figure 3.5: *Isotropic behavior of ESL etching.*

This technique has shown to be particularly well–suited for the releasing of photoplastic–based microstructures. SNOM probes presented in Chapter 6, for example, have been released from the mold using this method. An aluminum coating layer has been completely underetched, so that its transfer from the mold onto the photoplastic tip was performed without problem. Hence, this sacrificial layer method is not restricted to flat structures on flat substrates showing that this technique is versatile. Etch rate selectivity which depends both on bath chemistry and built–in potential can be modified.

As adhesion is kept strong between the substrate, the sacrificial layer and the microstructure to be released, further robust processing of the device is possible. ESL is a wet process, and as for the other wet sacrificial layer techniques, stiction still causes a problem. However, this is much less important in this case as structures are meant to be completely released from the substrate.

Chapter 4

Photoplastic AFM Probes

4.1 Introduction

Scanning Probe Microscopy (SPM) is a recently developed family of techniques that has become revolutionary tools for surface analysis and object manipulation at the nanometer scale. Invented in 1981 by G. Binnig, H. Rohrer and co-workers, the scanning tunneling microscope (STM) is the ancestor of all SPMs. It allows imaging of individual surface atoms with unprecedented resolution [41]. In STM, a sharp tip is brought in such close proximity with a conducting sample that the tunneling of electrons between them can occur. By scanning the tip over the surface and measuring the tunneling current, one obtains an image of the electronic structure of the sample surface with atomic resolution. The success of the STM has stimulated the development of other scanning probe microscopes [42] which have in common that they rely on mechanically scanning a sharp tip over a sample surface while measuring some interaction between the tip and the sample.

The atomic force microscope (AFM, also called scanning force microscope, SFM) [43], is one of the most widely used of all SPMs. In AFM, imaging is obtained by detecting the short–range forces occurring between a stylus and the sample. Hence, this technique is independent of the conductivities of the tip and the sample, so that insulating surfaces can also be investigated.

The most common applications of AFM are the topographic imaging of surfaces and the study of the nature of long and short–range forces between tip and surface [44]. Other common SPM–derived techniques include Magnetic Force Microscopy (MFM), Lateral Force Microscopy (LFM), Electrostatic Force Microscopy (EFM), or Scanning Capacitance Microscopy (SCM), for example. MFM images the spatial variation of magnetic interaction near a sample surface. For MFM, the tip is coated with a ferromagnetic thin film. The system operates in non-contact mode, detecting changes in the resonant frequency of the cantilever induced by the magnetic field's dependence on the tip-to-sample separation [45]. LFM measures lateral deflections (twisting) of the cantilever that arise from forces on the cantilever parallel to the plane of the sample surface. This technique is useful for imaging variations in sample surface friction [46]. In EFM, a voltage is applied between the tip and the sample while the cantilever hovers above the surface without touching it. The cantilever deflects when it scans over static charges, thus mapping the locally charged domains of the sample surface [47]. Similarly to EFM, SCM images spatial variations in capacitance by inducing a voltage between the tip and the sample [48]. The tip of an AFM is also widely used as a nanotool for chemical or physical surface modification at the nanometer scale. Scanning probe lithography (SPL), for example, is an emerging area of research in which the AFM tip is used to pattern nanometer-scale features [49]. When a voltage bias is applied between a sharp probe tip and a sample, an intense electric field is generated in the vicinity of the tip. This concentrated field can be used to cause a local oxidation of silicon [50] or metals [51], or for the electron exposure of resist materials [52]. AFM-based techniques have also proven interesting as an alternative for high density data storage, e.g. by using heat for the nanoindentation of polymer surfaces [53], or to locally switch phase change materials [54], or ferroelectric thin films [55]. However, the data rate achievable using a single cantilever is limited so that a massively parallel operation of AFM probes is required to enable the combination of high data densities with competitive data rates [56].

The concept of an array of AFM probes, which allows parallel operation, is subject to strong research efforts. Parallelism provides not only a solution to the limited single–probe operation speed, but also expands the possible imaging area. For certain applications, simple 1-D array arrangements of cantilevers are already interesting by providing several probes in the same fabrication–level chip unit: defective cantilevers can be replaced without change and extensive realignment of the entire chip. This is of special importance when operating the AFM in non-conventional environments where cantilever replacement is difficult or impossible. Such a concept has been developed in an AFM meant to be used in space exploration [57]. The applications mentioned above are only a few examples of areas in which AFM techniques are used. One can expect that in the future, AFM, and in particular arrayed AFM, will play an increasingly important role in such fields as for example molecular analysis, biology or medicine, for example [9, 58, 59].

4.2 Basics of AFM

4.2.1 Introduction

The basic setup of an AFM is depicted in Figure 4.1. A sharp tip attached to a usually cantilever–like spring probes the surface of a sample. Forces between the tip and the sample surface cause the cantilever to bend, or deflect. A detector measures the cantilever deflection z as the tip is either scanned over the sample in the x-y plane, or the sample is scanned under the tip. By use of Hook's law, $F = - k \cdot z$, with k the spring constant of the cantilever, the measured deflection is translated to a measure of the forces acting between the tip and the sample. This measure is then used to construct an image of the appropriate surface property (e.g. topography of the sample).

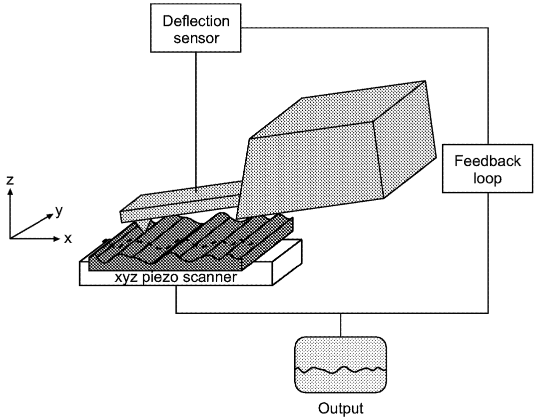

Figure 4.1: *AFM setup. A sample is scanned in the x-y plane relative to the tip. Probe deflection is detected as a function of the x-y position. Deflection is translated to an image of the surface properties.*

4.2.2 Detection Techniques

Several methods can be used to sense the deflection of the cantilever. Electron tunneling between a tunneling tip and the backside of the cantilever was the method employed in the first AFM set-ups [43]. This technique had the advantage of being extremely sensitive, but proved difficult to handle. Optical detection schemes are divided into two basic types: interferometry [60, 61] and beam deflection [62]. Interferometric systems measure the cantilever deflection using interferences between a reference beam and light reflected by the cantilever. In a typical beam-deflection AFM, a laser beam is reflected off the backside of the cantilever onto a position-sensitive photodiode. This very simple technique is the most commonly used in commercial systems. Optical deflection read-out offers a very good sensitivity, but suffers from certain disadvantages: optical sensors make up a large fraction of the size and complexity of the apparatus. They also require alignment to the cantilever that must be maintained during scanning. This is usually achieved by scanning the sample while holding the probe and detector at fixed positions, which however limits the sample size. Moreover, operation in special environments such as low temperature or ultra high vacuum is very difficult. A more compact, capacitive readout can be implemented by mounting a rigid counter electrode very close to the backside of the cantilever [63, 64], a deflection of the cantilever resulting in a capacitance change.

Integrating sensors directly with the AFM probe leads to very compact systems that do not necessitate the alignment of elements, and is also desirable where several probes need to be operated in parallel. An improved ease of scanning and mounting of the probe are also advantages of integrated detection schemes, which may be capacitive, piezoelectric or piezoresistive. Micromachined probes with capacitive read-out have been developed and used for imaging [65], but the very high sensitivity to noise has limited successful applications. A piezoelectric layer may be used to sense cantilever deflection [66, 67]: micromachined probes with piezoelectric read-out have been fabricated using a zinc oxide film deposited on one side of a micromachined cantilever [68, 69]. The main advantage of this technology is that a single layer may be used simultaneously as a sensor and as an actuator. Alternatively, the strong dependence of the bulk resistivity of silicon on applied stress (piezoresistive effect) has also been exploited to fabricate integrated deflection sensors in cantilevers [70, 71]. Integrated piezoresistors are connected to a Wheatstone bridge, allowing cantilever movements to be detected. The piezoresistive effect has also been used to generate variations in the channel carrier mobility of a MOS transistor integrated at the base of a cantilever. Changes in the source-drain current allowed the sensing of the cantilever deflection [72]. Integrated piezoresistive silicon sensors and integrated piezoelectric zinc oxide actuators have also been implemented on the same cantilever [73].

Another detection method which has been demonstrated recently is thermal sensing [74]. It is based on measuring the change in thermal conductance through air between a heated resistor on the cantilever and the sample as a function of the spacing between the two. This method is only applicable for certain kinds of samples to be investigated, and has been used so far only for the readback of nanoindented pits in AFM-based thermomechanical data storage [53, 75].

4.2.3 Operation Modes

Atomic force microscopes can be operated in several scan modes depending on the working distance between tip and sample. They are equivalent to the different force regimes present. Three modes of operation are most commonly used: *contact*, *non-contact*, and *intermittent contact* modes. The different force regimes between the tip and sample are described in the force-distance curve of Figure 4.2. When the tip approaches the sample, it first explores mainly attractive van der Waals forces, and when the distance becomes lower than 2 nm, one has mainly repulsive forces due to the repulsion of the electronic clouds of the atoms of the tip and of the sample. The tip-sample interactions forces can be divided into two classes—long ranges forces and short range forces—and are also dependent on the experimental conditions. These long and short range forces are listed in table 4.1.

Table 4.1: Forces in AFM

Short Range Forces (at 2 nm)	Long Range Forces (at 15 nm)
• Tip and sample electronic clouds: repulsive	• van der Waals: attractive
• Covalent forces: attractive	• Capillarity due to the thin water film: attractive
• Deformation forces: due to tip and sample plasticity	• Magnetic forces
• Friction forces: lateral forces on the tip (repulsive)	• Electrostatic forces (dominant in liquids)

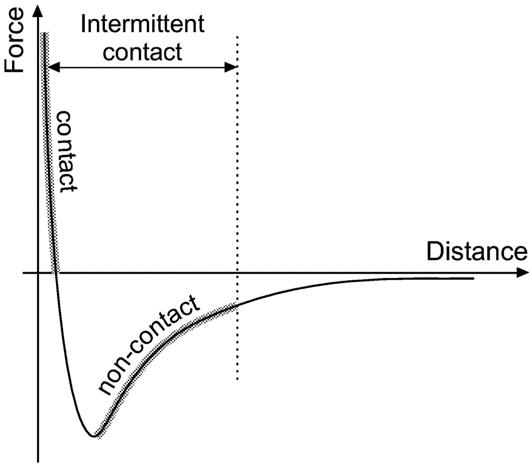

Figure 4.2: *Qualitative representation of force versus distance to a sample surface. Contact mode is made in the regime of repulsive forces. Non contact-mode is in the attractive forces regime.*

In *contact mode*, the tip is in physical contact or in close proximity with the sample (less than a few Å). The force applied on the tip is measured directly by the deflection induced on the cantilever. The force is maintained constant by keeping this deflection constant with the feedback loop, thereby giving a direct topography image of the sample. A low spring constant (typically 0.01 N/m to 1 N/m) of the cantilever is desired to avoid pressure on the sample, which may result in unwanted scratches. The total forces acting between the tip and the sample are repulsive in this mode of operation and are typically between 10^{-7} to 10^{-6} N.

In *non-contact* mode, the tip is kept at a short distance from the sample, usually around 10 nm, and vibrates near its natural resonant frequency. The presence of the force, or more precisely the gradient of the force, $\partial F_z/\partial z$ acts to modify the effective spring constant k of the cantilever according to

$$k = k_0 + \frac{\partial F_z}{\partial z} \tag{4.1}$$

where k_0 is the spring constant of the isolated cantilever. If the sample exerts an attractive force on the cantilever, the spring constant will effectively soften, causing a decrease of the resonant frequency. This decrease if then detected by measuring the amplitude, phase or frequency change of the vibration. The total force between the tip and the sample is very low, generally about 10^{-12} N. This low force is advantageous for studying soft or fragile samples. In this mode of operation, a high spring constant (1 N/m to 100 N/m) of the cantilever is preferred, as soft cantilever tend to be attracted to the sample by van der Waals interactions. The resonant frequency of the cantilevers must be high enough (a few kHz) so that the probe is not a limiting factor in the speed of response to surface topography. A high Q-factor[1] is also desirable, as the sensitivity of this technique is proportional to the Q [76].

In an intermediate mode known as *intermittent contact*, the cantilever is vibrated near its mechanical resonant frequency, and brought very close to the sample, so that at the bottom of its travel it just barely hits, or "taps" the sample. In this mode, a high force constant (> 10 N/m) is required so that the cantilever has enough potential energy to retract from the sample after having tapped it.

Depending on the structure of the surface and the scan mode to be used, probes with different mechanical characteristics and tip shapes should be chosen. Hence, there is no universal probe for every purpose. Applications should drive the fabrication of the probes, but a high degree of flexibility in the design and fabrication of the tip and cantilever are also desired in order to avoid too specific probes.

4.3 AFM Probes

The cantilever together with the tip at its free end (also called the AFM probe) is a key component of the atomic force microscope. The tip needs

---

[1] The Q-factor (quality factor) is a measure of the sharpness of the resonance peak. It is equal to the ratio between the resonant frequency and the frequency span between the -3 dB points.

to be sharp enough to record the investigated sample with high lateral resolution. The cantilever must also have appropriate mechanical characteristics that are in compliance with the type of operation selected, i.e. contact or non-contact mode. The original atomic force microscope used a handmade cantilever spring cut from a piece of gold foil approximately 1 mm long. A small diamond stylus glued to the foil served as the tip [43]. The requirements for a low spring constant (less than 5 N/m) and a high resonant frequency (greater than 10 kHz) led to miniaturization and hence to microfabrication technologies. Miniaturization of the probes is a simple way to reduce the effective mass m_0 that loads the spring, though keeping the ratio k/m_0 large, as the spring constant k decreases. Moreover, the use of silicon micromachining techniques allowed the fabrication of sharper tips than the one obtained by electrochemical etching techniques, for example. Silicon micromachining also opened the way to batch fabrication. Hundreds of probes can be produced at the same time on the same wafer. This guarantees a higher degree of reproducibility in the mechanical properties of the cantilevers while decreasing the fabrication price. In addition, microfabrication enabled the fabrication of integrated deflection sensing and of cantilever arrays.

Several different micromachining processes have been used to make AFM cantilevers, depending on the material used and the shape desired. The two most commonly used cantilever materials are silicon and silicon nitride. Tip shapes are usually conical or pyramidal.

Silicon AFM cantilevers are fabricated using bulk micromachining. The tip and cantilever are first defined from the front side of the wafer using chemical dry or wet etching techniques. The cantilever is then made free-standing by etching the substrate from the backside using anisotropic wet etchants and etch stop techniques. Silicon cantilevers with integrated tips were first fabricated using several steps of anisotropic wet etching [77]. Figure 4.3.1 shows a typical method for fabricating highly boron doped silicon cantilevers. The conical tip is made by first patterning a circular silicon dioxide dot on a silicon wafer. Subsequently, the silicon is etched, usually by plasma etching. As the silicon is etched vertically, it is also etched laterally under the oxide mask, depending on plasma parameters. The etching is terminated just before the silicon has been totally undercut beneath the silicon dioxide dot, Figure 4.3.1(a). The silicon is then oxidized so that a tip is formed after removal of the oxide, Figure 4.3.1(b). The silicon is then doped with boron in the region that will become the cantilever, Figure 4.3.1(c). The substrate is finally etched from the backside yielding a free-standing boron-doped single crystal silicon cantilever with integrated tip, Figure 4.3.1(d). Boron doping is used in this case as an etch-stop technique and produces conductive cantilevers. Figure 4.4 shows a scanning electron micrograph (SEM) of commercially available silicon AFM cantilever fabricated using wet etching techniques.

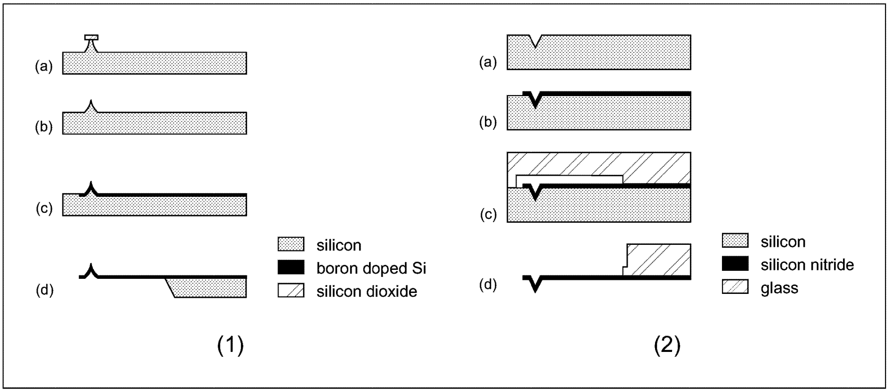

Figure 4.3: *Process flows for the standard fabrication of (1) highly boron doped silicon cantilever with conical tip, and (2) silicon nitride cantilever with pyramidal tip, using microfabrication techniques.*

Silicon oxide or silicon nitride cantilevers with add-on or integrated tips are based on the deposition of thin films onto a silicon substrate [78, 79]. Cantilevers are made free-standing by etching a window through the silicon

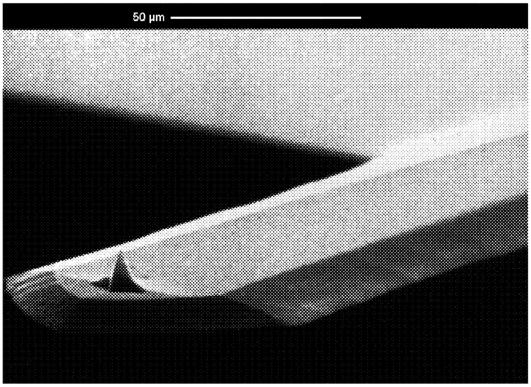

Figure 4.4: *Commercially available silicon cantilever with silicon tip. Image courtesy of Nanosensors GmbH & Co. KG*

substrate from the backside of the wafer or by bonding the cantilever to a glass substrate before completely dissolving the silicon substrate. Figure 4.3.2 shows a typical manufacturing process to fabricate silicon nitride cantilevers with pyramidal tips. A square pyramidal pit of a few microns on a side is first etched in a ⟨100⟩ silicon substrate using anisotropic wet etchant such as potassium hydroxide (KOH), Figure 4.3.2(a). The pit is then used as a mold for the silicon nitride, which is deposited by a low-pressure chemical vapor deposition (LPCVD) technique. The thickness of the deposited film will be the final thickness of the cantilever. The silicon nitride is then photolithography patterned in the desired cantilever shape, Figure 4.3.2(b), and a glass substrate is anodically bonded to the wafer, Figure 4.3.2(c). The glass is then saw to provide clearance for the cantilever, and the silicon is removed in a chemical etchant, Figure 4.3.2(d).

The most common way to obtain cantilevers with different materials is to coat standard silicon or silicon nitride cantilevers with the material of choice. Coatings are usually done by evaporation or sputtering.

Batch fabrication of AFM cantilevers has permitted the fabrication and characterization of specialized tips for a variety of experiments. However, simple fabrication of low-cost probes with a small spring constants still remains a challenging issue. Moreover, silicon and silicon nitride cantilevers fabrication involves either a partial or complete etching of the 0.5-mm thick silicon substrate, leading to very long etching times.

4.4 Photoplastic AFM Probes

4.4.1 Introduction

As described in paragraph 4.3, micromachining technologies have enabled the batch fabrication of AFM probes made of silicon, silicon nitride, or silicon oxide. Such conventional probe fabrication however demands expensive tools (oxidation oven, plasma etcher, thin film deposition tools) that add to the cost of the probes. While exploring cheaper alternatives, we are also interested in obtaining certain mechanical properties that are difficult to achieve with classical silicon technology. The main characteristics that have to be fulfilled by a cantilever probe are a low stiffness, a high resonant frequency, and a fairly high Q factor, together with a sharp tip. The property of softness of the cantilevers (spring constant < 5 N/m), which can be problematic conventionally, is made achievable by using a material with a small Young's modulus, such as for example a polymer. Pechmann *et al.* [80] reported the fabrication of very soft cantilevers using a novolak resist as material. The process used was nevertheless complex, involving silicon etching from the backside. Moreover, the tip was placed on the lever by electron-beam deposition (EBD). This chapter reviews how a fabrication method similar to that used for the fabrication of silicon nitride cantilevers can be used in combination with a low Young's modulus epoxy material to obtain soft probes with soft integrated tips.

4.4.2 Cantilever Design

As mentioned above, the design of a cantilever probe for AFM has to fulfill specific mechanical requirements. A large anchor piece should support the cantilever for handling purposes. The spring constant of a cantilever is defined as the ratio between the force applied at its free end and the deflection at this point. It can be calculated in close analytical form from basic mechanics for most cantilever shapes [81]. The spring constant in the z direction k_b of a cantilever beam having a rectangular cross section is given by

$$k_b = \frac{Ewt^3}{4l^3} \tag{4.2}$$

while the torsional spring constant k_t is given

$$k_t = \frac{Gwt^3}{3hl^2} \tag{4.3}$$

where w, t, and l denote the width, thickness, and length of the lever, h the height of the tip, E and G the Young's modulus and shear modulus, respectively, of the cantilever's material (see Figure 4.5)

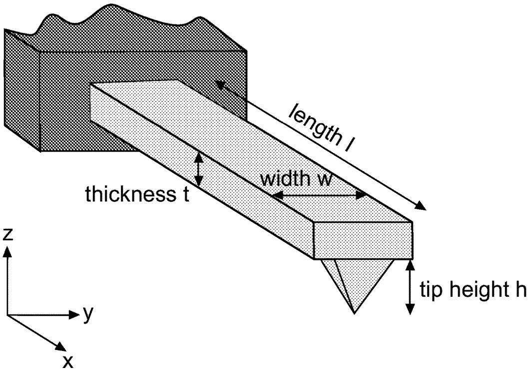

Figure 4.5: *Dimensions for a single–side clamped cantilever with a rectangular cross section.*

The resonance frequency of an oscillating cantilever can be calculated by solving the equations of motion for the cantilever and by finding the eigenvalues (for details, see Appendix A). The resonant frequency f_b of a rectangular type cantilever can be expressed by:

$$f_b = \frac{1}{2\pi}\sqrt{\frac{k_b}{m^*}} = \frac{3.51}{2\pi l^2}\sqrt{\frac{EI}{\rho S}} = 0.162\frac{t}{l^2}\sqrt{\frac{E}{\rho}} \tag{4.4}$$

where k_b is the spring constant of the lever, m^* is the effective mass of the cantilever, ρ the density of mass of the cantilever's material and I the moment of inertia. The effective mass is related to the mass of the beam, m_b, through the relation $m^* = n \cdot m_b$, where n is a geometric parameter. For the case of a rectangular bar, n is 0.24 [82]. The formula above also yields good approximations for triangular–shaped cantilevers.

When an optical beam deflection is used to measure the cantilever's motion, the sensitivity of the detection system is inversely proportional to the length of the cantilever. Unfortunately, as can be seen from equation 4.2, short levers are a drawback if a low spring constant is required. A certain width of the cantilever is also necessary for sufficient reflection and simple alignment of the laser beam. Normally, silicon nitride and silicon oxide cantilevers have a thickness below 1 μm, while silicon cantilevers typically have a thickness above 1 μm. Often the cantilever thickness is fixed and the spring constant and resonance frequency are adjusted by varying the length as seen from equations 4.2 and 4.4. Typically, a rectangular cantilever beam is 20-50 μm wide, 200-400 μm long, and 1-5 μm thick, depending on the applications foreseen [83]. Silicon and silicon nitride have a high Young's modulus E (190 and 385 GPa, respectively [14]). With such materials, the only way to obtain a low spring constant cantilever at short lengths ($l < 200$ μm) is to reduce the thickness of the cantilever. But very small thicknesses ($t < 1$ μm) are difficult to achieve with silicon. Alternatively, one can use a material with a low Young's modulus to fabricate soft cantilevers, providing their dimensions are not too critical.

SU-8, with a Young's modulus of 4 GPa, is well–suited for the fabrication of such soft cantilevers. Figure 4.6 compares the calculated spring constants of silicon, silicon nitride, and SU-8 rectangular cantilever beams of equal length and width as a function of thickness. It clearly shows that very low spring constants can easily be achieved with SU-8 thicknesses of several micrometers. In contrast, levers with the same spring constant made of silicon must be very thin, which is difficult to achieve and control on a wafer level. This difference between the curves comes from the large relative magnitudes of the respective Young's modulus of each material.

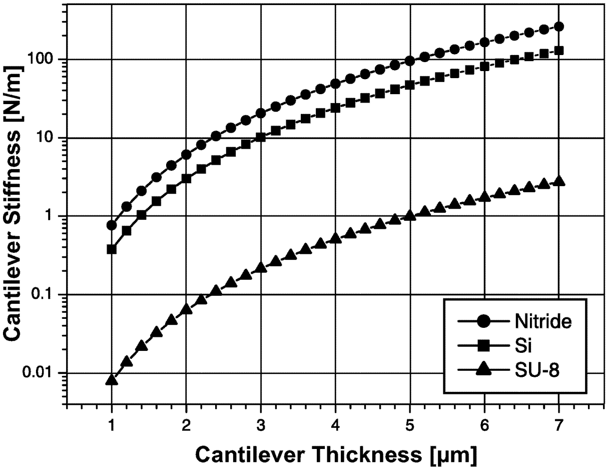

Figure 4.6: *Calculated spring constant of silicon, silicon nitride and SU-8 cantilevers as a function of thickness. Cantilevers have a length of 156 µm and a width of 30 µm.*

In order to take advantage of the small Young's modulus of the SU-8, short photoplastic cantilever beams with a small spring constant are investigated. Cantilevers with 1 N/m are first designed to demonstrate the feasibility of the concept.

In the first design, three different cantilevers beams are presented. The geometries and the corresponding calculated resonant frequencies and spring constants are listed in table 4.2. A cantilever thickness t of 5 μm and a spring constant k of 1 N/m are chosen as fixed common parameters. Different values for the width w are chosen, leading through the constraints on t and k to calculated values for the length l and resonant frequency f for the different probes.

Table 4.2: Mechanical characteristics of the designed SU-8 AFM cantilevers

ID ♯	k (N/m)	t (μm)	w (μm)	E (GPa)	ρ (g/cm^3)	l (μm)	f (kHz)
SL1	1	5	30	4	1.2	155	61.5
SL2	1	5	40	4	1.2	171	50.7
SL3	1	5	50	4	1.2	184	43.7

As will be described in paragraph 4.4.5, a fixed thickness was chosen due to the fabrication process using spin-coating. Table 4.2 shows that short levers can be obtained with a fairly large thickness and a low spring constant using a material with a small Young's modulus.

4.4.3 Photoplastic Tip

Tips for atomic force microscopy can be produced by either direct [84] or indirect tip technologies [85]. In the indirect method tip, shaped holes are etched in a silicon substrate, and thereafter filled with the desired tip/cantilever materials. Later, the tips are released by etching away the silicon wafer, which only serves as a mold substrate. In the direct method the tips are etched directly in the tip material, normally by undercutting an etch mask.

Integrated photoplastic tips are obtained indirectly by casting the photoresist into a prestructured mold on the substrate. A pyramidal tip is made using a pyramidal hole etched in the silicon substrate using potassium hydroxide (KOH, 40% wt) at 60° C for 1 h. At this temperature, the etch rate of silicon in the [100] direction is approximately 16 μm/h. For 8.5 μm deep holes, the 1 h etch duration represents enough overetching time (~90%) to ensure that the four $\langle 111 \rangle$ planes delimiting the pyramidal hole intercept each other. The KOH etching starts from circular openings in a silicon dioxide mask, this shape being chosen in order to get a better lateral dimension control of the tip by avoiding misalignments with the planes of the silicon wafer. After cleaning of the residues due to KOH etching in buffered hydrofluoric acid (BHF), a low-temperature thermal wet oxidation (950° C, 4h 30 min, 700 nm) is performed in order to sharpen the bottom of the pyramidal holes [86]. Nonuniform oxide growth in the bottoms of pits and other highly nonplanar regions occurs because there is less surface area available for oxidizing species to be incorporated, allowing fewer of them to reach the oxide/silicon interface to react with the available silicon atoms. Thus the local oxidation rate is depressed in comparison to rates in flat areas. At high oxidation temperature (1100–1200°C), this geometric effect is less significant since viscous flow of the oxide film tends to increase the radius of curvature of the nonplanar regions such that the surface area of the oxide film is more comparable to the area at the oxide/silicon interface [87]. The oxidation time is chosen to yield an SiO_2 thickness of 700 nm on the $\langle 100 \rangle$ planes of the substrate. The actual oxide thicknesses on the $\langle 111 \rangle$ planes of the pyramidal hole are actually thicker due to a dependence of the oxidation kinetics on the crystallographic orientation [88].

Figure 4.7 illustrates the effect of the low-temperature thermal wet oxidation at the bottom of etched pyramidal trenches. Oxidation sharpens the bottom of the trenches, thus leading to sharper tip molds. In the case of a pyramidal pit, the effect may be larger, as oxidation occurs on the four sides of the pit compared to the two sides of a trench, but it cannot be visualized so easily.

Releasing the tips from the mold is a critical operation for the tip sharpness. The use of a sacrificial layer (see chapter 3) facilitates the releasing, but depositing material in the hole reduces the sharpness of the mold. A sacri-

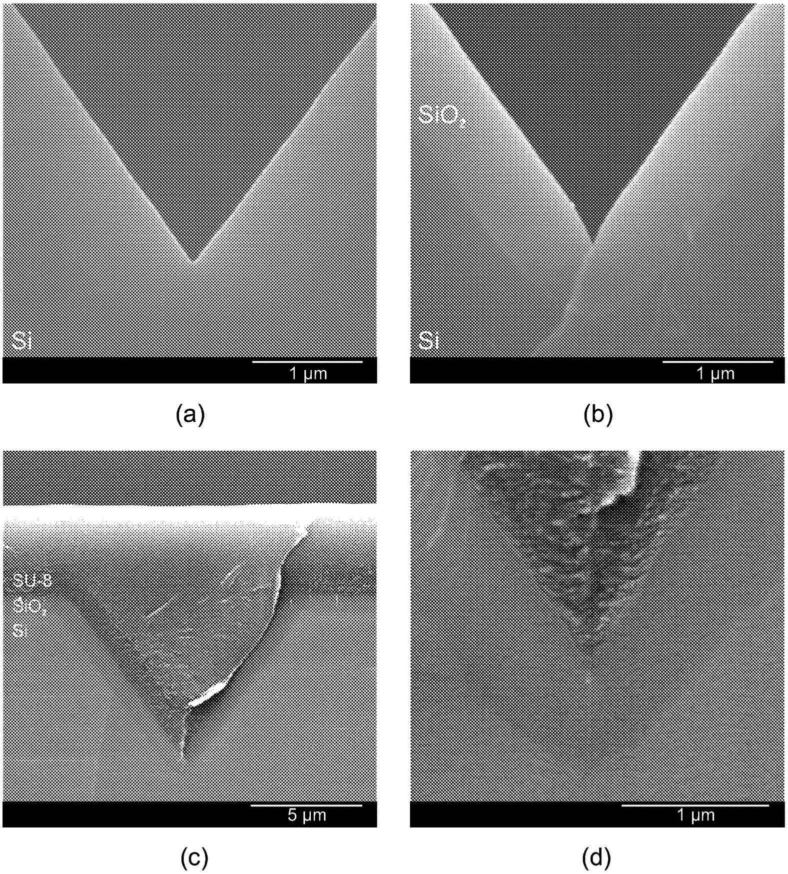

Figure 4.7: *SEMs of the bottom of pyramidal trenches simulating the bottom of a tip mold. (a) Tip mold without oxidation sharpening. The sharpness of the mold is given by the abruptness of the* $\langle 111 \rangle$ *planes intersection. (b) Tip mold after low-temperature thermal oxidation sharpening. The sharpness of the mold has increased and the cone angle at the apex has been reduced. (c) Molded SU-8 in a pyramidal hole after resist spin-coating and wafer cleaving, showing the planarization of the SU-8 layer. (d) Closeup of the bottom of the pyramidal hole. SU-8 is molded into the nanometer pit.*

ficial layer can be selectively deposited under the structure to be released, but not in the mold, by protecting the pyramidal pit during the deposition of the sacrificial layer using lift-off techniques.

Tips produced in this manner have been measured to have radii of curvature of less than 15 nm. Such values have been determined by scanning electron microscopy (SEM) measurements of released tips after 20 nm of gold had been sputtered on them, so that the actual radii of curvature of the photoplastic tips are somewhat smaller than indicated by SEM measurements. Figure 4.8 shows a SU-8 photoplastic pyramidal tip. Note that since the mold determines the tip shape, this method is not necessarily restricted to pyramids. Other mold shapes can be produced using oxidation, oxide removal, or isotropic silicon etching, for example.

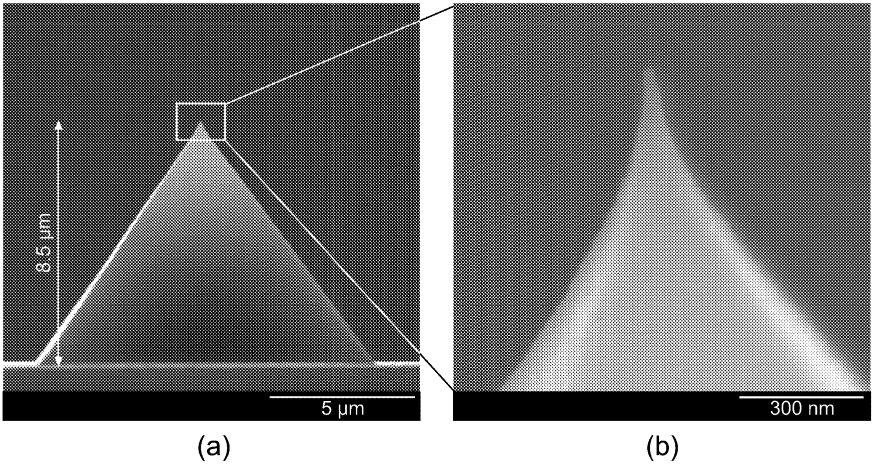

Figure 4.8: *SEMs of a pyramidal photoplastic molded tip after releasing from the mold. (a) The tip height is given by the depth of the pyramidal hole, in this case 8.5 μm. (b) Closeup of the tip. Radii of curvature smaller than 15 nm have been measured.*

4.4.4 Fabrication

The fabrication process of SU-8 photoplastic cantilevers is based on the multiple spin-coating, exposure and development of SU-8 photoresist on a prestructured silicon wafer. These steps are repeated for subsequent layers [89]. Hence, cantilevers with integrated tips are fabricated in a very similar manner as that in which Albrecht *et al.* made silicon nitride cantilevers [79].

The initial material is a 100-mm ⟨100⟩ single-side polished silicon wafer with 1 μm of thermally grown oxide on both sides. Circular openings are patterned in the top-side oxide using CHF_3/O_2 reactive ion etching (RIE) to form the mask for the tip molds etching. Pyramidal holes are etched in the silicon wafer using KOH anisotropic wet etching, and the mold is oxidation sharpened (for details, see paragraph 4.4.3). The final tip sharpness depends mainly on the quality of this mold.

After sputter–deposition of a 20-nm thick sacrificial aluminum layer, Figure 4.9(c), a first layer of SU-8 is spin coated onto the wafer. The tips are defined by the resist filling up the sharpened pyramidal holes. A contact mask exposure with a near-UV light source and subsequent development leave crosslinked photoplastic cantilevers on the silicon substrate. The cantilever's thickness is determined by the thickness of this first resist layer as shown in Figure 4.9(d). In order to get a fully crosslinked material for the cantilever, a hardbake step is performed in an oven at 200° C for 6 minutes. Thicker layers of photoresist are then spin coated, exposed, and developed to form the body of the chip, Figure 4.9(g,h,i). Afterwards, the levers are released by etching the sacrificial layer, and the chips are mechanically removed from the silicon wafer mold without damaging it, Figure 4.9(j). After a cleaning procedure using a combination of H_2SO_4:H_2O_2, 3:1 wet etching, and O_2 plasma etching, the mold can subsequently be reused for the fabrication of a new batch. This is a very important step to minimize the cost of these plastic probes. Finally, 40 nm of gold is evaporated on the backside of the levers to achieve sufficient reflection for optical detection.

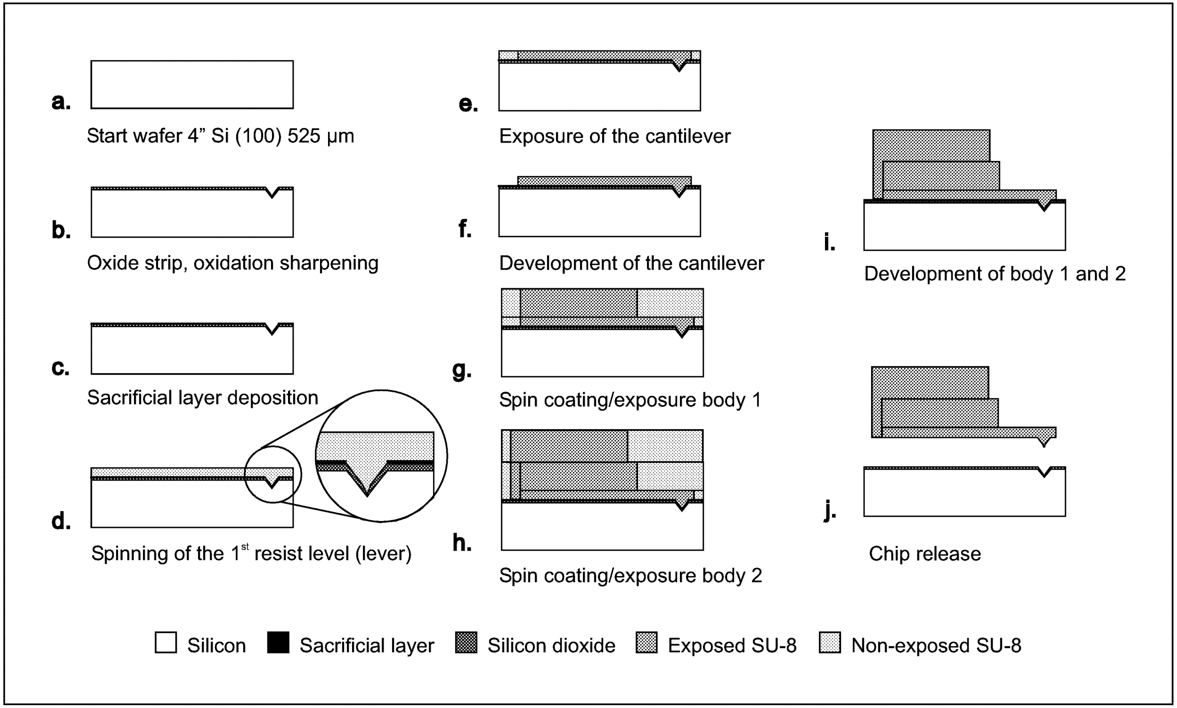

Figure 4.9: *Outline of the process sequence for the fabrication of photoplastic AFM probes; for details refer to text.*

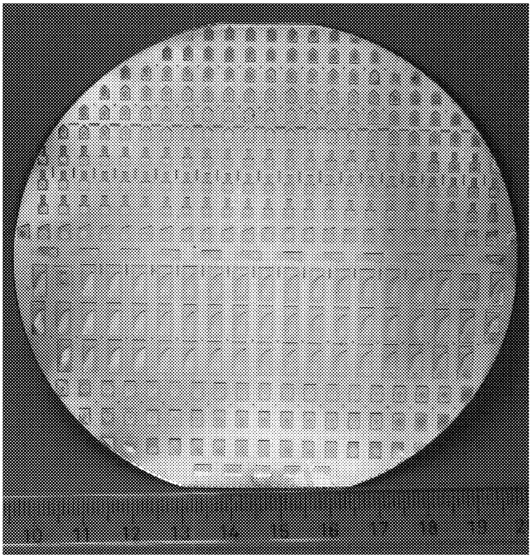

Figure 4.10: *Optical micrograph of a 100–mm silicon wafer with microfabricated photoplastic SU-8 microstructures.*

Figure 4.10 shows a 4-in. silicon wafer with fabricated photoplastic microstructures, whereas Figure 4.11 shows SEMs of a fabricated photoplastic SU-8 SFM probe with integrated sharp pyramidal tips. The thickness, width, and length of the levers are 6.6 μm, 31 μm, and 150 μm, respectively, which yield a calculated spring constant of 2.64 N/m and a resonant frequency of 87 kHz. Actual measured resonant frequencies differ up by 5% from these theoretical values. The discrepancy is due mainly to the limited measurement accuracy of the lever dimensions and the approximations of the density and Young's modulus of SU-8 material. A Q factor in air of about 30 was deduced from the frequency response of one such cantilever (Figure 4.12).

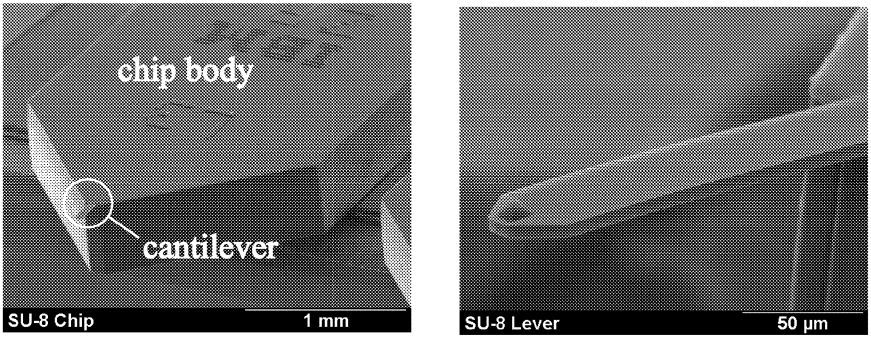

(a) (b)

Figure 4.11: *(a) General view of an SU-8 AFM probe. (b) Closeup of an SU-8 lever with integrated tip at the end. The tip is 8.5 μm high.*

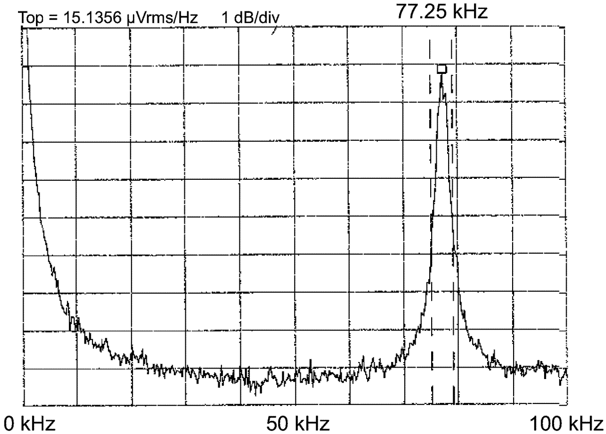

Figure 4.12: *Frequency response of an SU-8 cantilever. Resonant has been found to be 77.25 kHz. A Q factor of 30 has been deduced from the curve.*

4.4.5 Process Control and Flexibility

Controlling the cantilever thickness is a major challenge in AFM probe fabrication, because the spring constant is proportional to the third power of the thickness. The thickness of the photoplastic cantilevers described here is determined by the SU-8 spin-coating parameters. Uniformity and reproducibility of photoresist spin-coating processes are known to be very good, hence the stiffness and resonant frequency of photoplastic levers are well defined and controlled. Figure 4.13 illustrate the thickness uniformity of photoplastic cantilevers over a 100–mm wafer. For a target cantilever thickness of 6 μm, a mean value of 5.91 μm with a standard deviation of 0.079 μm has been measured, resulting in a standard deviation of the spring constant of 0.073 N/m assuming nominal length and width. The cantilever thicknesses were measured directly on the wafer after development of the cantilever layer, using a profilometer tool [90].

Because it is based on two subsequent photolithography steps, the SU-8 AFM cantilever fabrication process exhibits a high degree of flexibility. It is for instance possible to fabricate different probe batches with different geometrical characteristics, hence different mechanical characteristics, with the same photolithographic masks. Lever thickness can be changed easily by modifying the spin-coating parameters. Figure 4.14 shows SU-8 cantilevers with 1 μm and 6 μm thicknesses. Spinning speed and resist viscosity were adjusted to obtain an SU-8 layer of 1 and 6 μm. The same mask was used to expose these different cantilevers.

A careful design of the mask layers enables other kinds of freedom in lever fabrication. As illustrated for instance in Figure 4.15, lever lengths can be adapted by shifting the chip body layer in the y direction with respect to the cantilever layer.

This fabrication flexibility has been used to correct a problem that occurred during AFM imaging with the first fabricated cantilevers. In order to mechanically release the probe with tweezers, the chip body needs to have a certain minimal thickness, typically around 400 μm. Typically, the

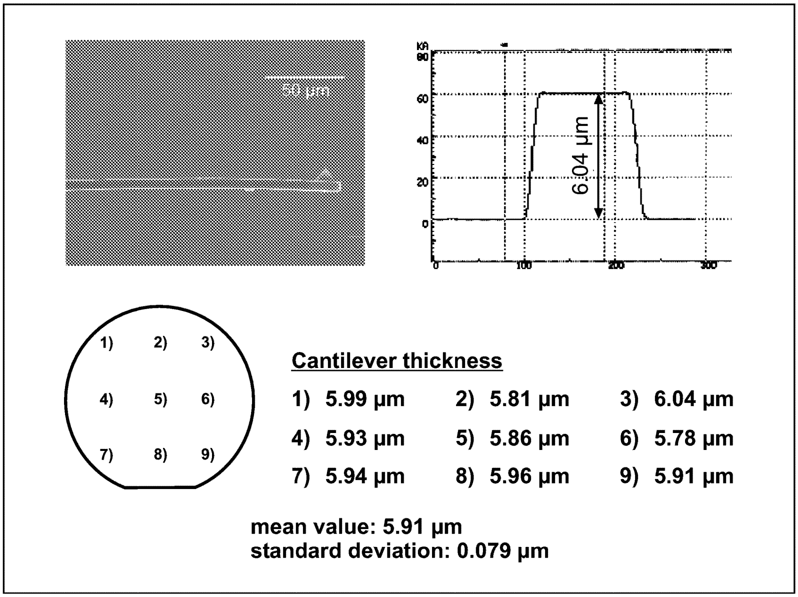

Cantilever thickness

1) 5.99 µm	2) 5.81 µm	3) 6.04 µm
4) 5.93 µm	5) 5.86 µm	6) 5.78 µm
7) 5.94 µm	8) 5.96 µm	9) 5.91 µm

mean value: 5.91 µm
standard deviation: 0.079 µm

Figure 4.13: *Cantilever thickness uniformity mapping over a 100–mm silicon wafer.*

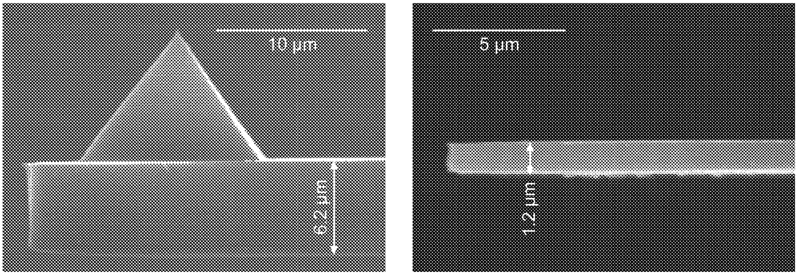

(a) (b)

Figure 4.14: *(a) 6.2–µm thick SU-8 cantilever with integrated tip. (b) 1.2–µm-thick SU-8 cantilever without tip. Spin-coating parameters and resist viscosity have been chosen to obtain the different thicknesses.*

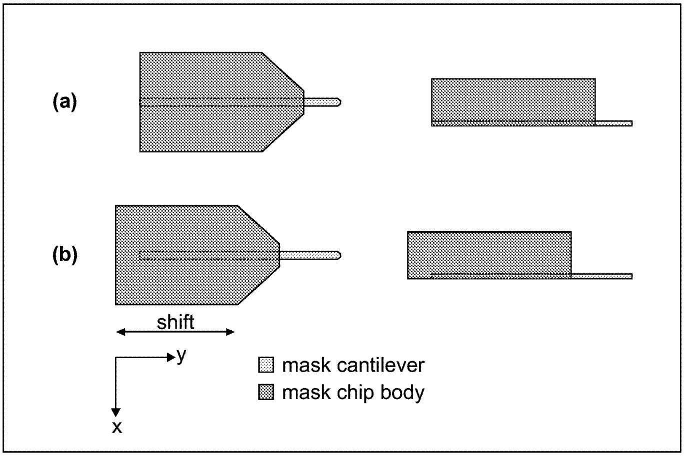

Figure 4.15: *SU-8 cantilever fabrication flexibility. Lever lengths can be easily modified by a simple shift of the chip body mask in the y direction. No additional mask is necessary. As SU-8 is a negative photoresist, polarity on real chromium masks is inverted (e.g. gray parts are transparent)*

approach of the sample with the cantilever probe is made under an angle α to ensure a large clearance at all points except the tip (this angle is typically between 10° and 15°). Because short levers were designed, there was a risk that the laser beam would not be reflected off the backside of the cantilever due to a shadowing of the chip body, as illustrated in Figure 4.16. If the lever beam is reflected at 2/3 of the lever of length l, the maximum allowable chip thickness t_{max} is given by

$$t_{max} = \frac{2}{3} \cdot \frac{l}{\tan \alpha} \tag{4.5}$$

where α is the approach angle.

As the first batch of fabricated probes presented this problem, due to a fairly thick body layer, it was first attempted to clear a path for the laser beam by hand–cutting the edge of the probe body with a scalpel. Clearly, this method is not a reliable or batch approach. To overcome this prob-

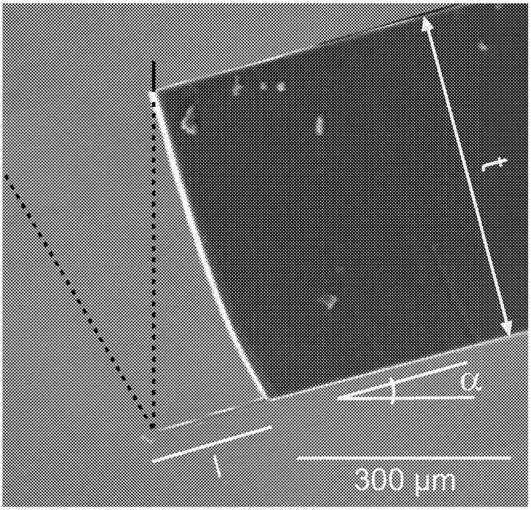

Figure 4.16: *Illustration of the shadowing effect, consequence of a large chip body. Laser beam is not reflected onto the backside of the cantilever. The shadowing depends on the approach angle α, the body thickness t and the cantilever length l. In this example, α, t and l are 15°, 465 μm and 175 μm, respectively.*

lem, the chip body has been divided into two offset layers: after spin-coating and exposure of a first, 200–μm thick body layer, a second body layer is spin coated. Before exposure of this second body layer, the mask is shifted backwards by 180 μm, thereby providing the necessary clearance for the laser beam, while maintaining a total thickness of the body layers that still allows simple mechanical release with tweezers. The process sequence depicted in Figure 4.9 illustrates this two–step body fabrication. In this way, the shadowing problem can be easily solved without needing a new design or new masks. Figure 4.17 shows SEMs of a chip cut by hand with a scalpel and of the clearance provided by using an offset second body layer.

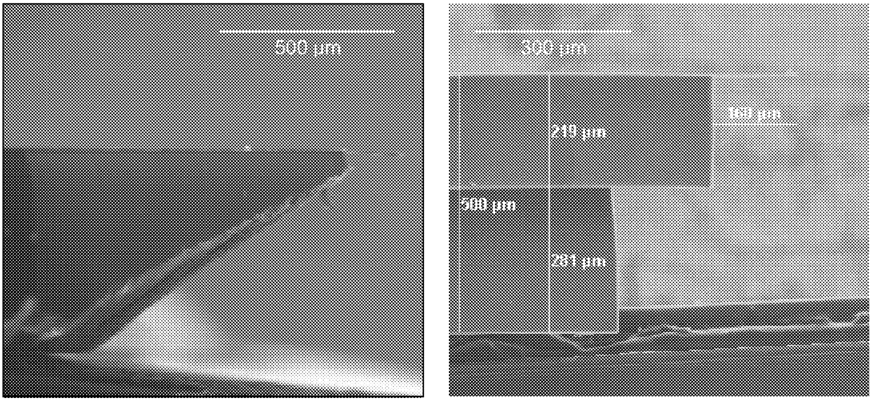

(a) (b)

Figure 4.17: *SEMs of fabricated thick chips with enough clearance for the laser beam to be reflected off the cantilever's backside. (a) The clearance is obtained by cutting the probe edge with a scalpel. (b) The clearance is obtained by using two body layers shifted by 180 μm.*

4.4.6 AFM Experiments

The performance of the epoxy cantilevers in terms of handling and resolution has been investigated in atomic force microscopy (AFM) experiments on so-called soft condensed-matter samples. These tests were made in tapping mode, under ambient conditions, on samples of mixed Langmuir–Blodgett films on silicon (Figure 4.18), DNA–plasmid molecules (Figure 4.19), and M13 bacteriophage (Figure 4.20). The resonance frequency was set to about 70 kHz, close below the mechanical eigen resonance of the cantilever. Figure 4.18 clearly shows the coexisting hydrocarbon and fluorocarbon molecular phases (or domains) which are delineated by regions of different hydrophobicity (surface energy). The lateral resolution can be estimated from Figure 4.19, where the width of the imaged DNA strand is 5–6 nm. The vertical resolution was found to be of the order of 0.1 nm. The background of Figure 4.19 reveals contamination due to aging of the sample. The image of the M13 phages (Figure 4.20) clearly shows the habitus of the individual viruses (1 μm long and 10 nm thick). Even the periodicity along the virus can be seen.

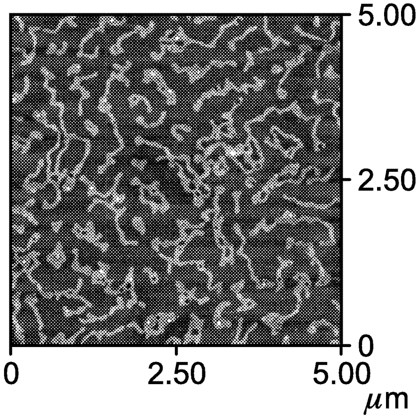

Figure 4.18: *AFM image (5 × 5 μm^2) of a mixed Langmuir-Blodgett film with coexisting hydrocarbon and fluorocarbon molecular domains. The image z range corresponds to 5 nm.*

Experiments with single levers in solutions of various pH showed a very good stability of the resonant frequency over time. The cantilever's resonant frequency response was first observed in a solution with a pH of 7, Figure 4.21(a). The cantilever was then immersed in a solution in which the pH was adjusted to 4 by adding a phtalate buffer. The resonant frequency response was measured directly after immersion, and after 2 hours in the solution, Figure 4.21(b). After rinsing, the cantilever was dipped in a solution in which the pH was brought to 10 by adding a borax buffer. In this basic solution, the cantilever's resonant frequency response was measured directly after immersion and after 50 min., Figure 4.21(c). A comparison of the different resonant frequency response curves of the cantilever in the different solutions and after different times shows that no change occurred, demonstrating the chemical stability of the photoplastic probes.

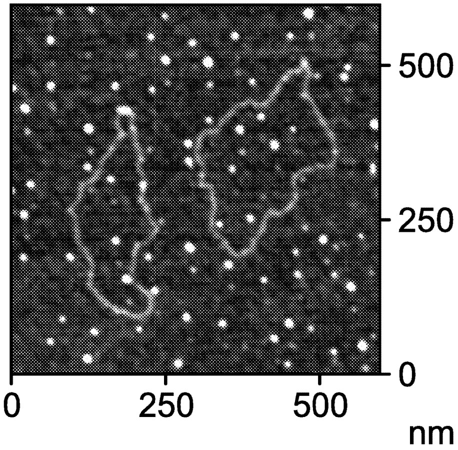

Figure 4.19: *AFM image (0.6 × 0.6 μm^2) of DNA–plasmid molecules (pGEM–3Zf vector from Promega Corporation, Madison, WI, USA). The width of the DNA strand is 5–6 nm. The z-scale was color-adjusted to 1.5 nm.*

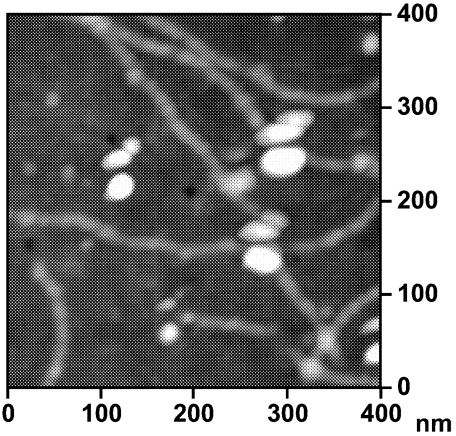

Figure 4.20: *AFM image (0.4 × 0.4 μm^2) of M13 bacteriophages. A periodicity of 17 nm along the virus strand is resolved.*

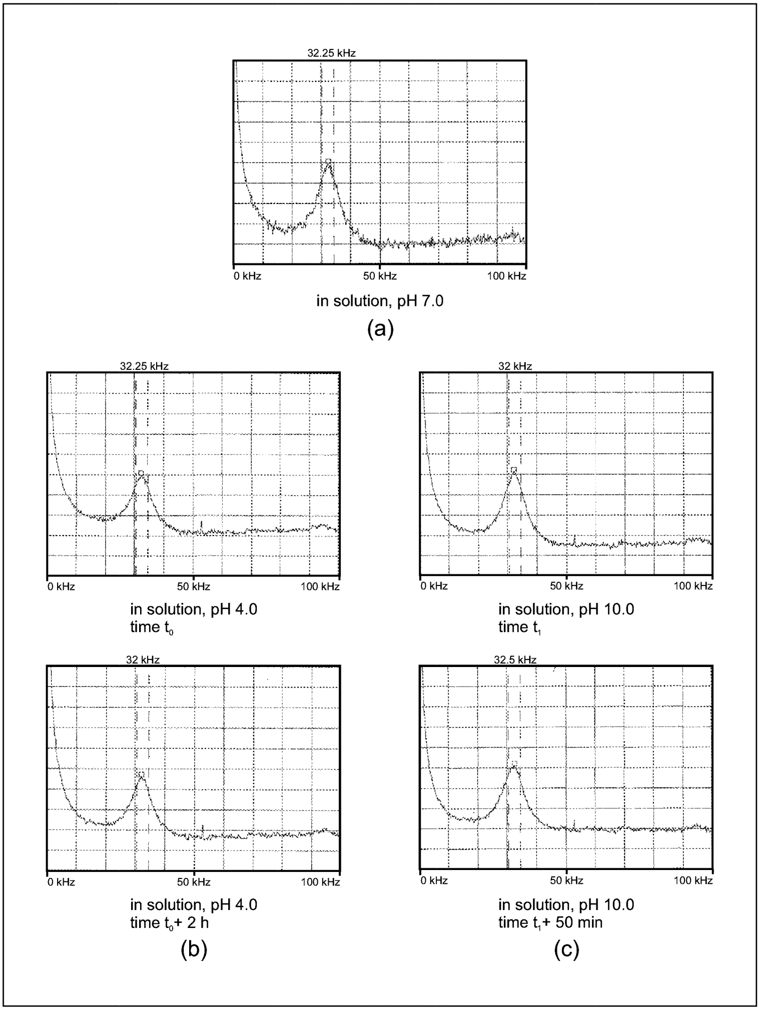

Figure 4.21: *Chemical stability of the SU-8 cantilevers. (a) Resonant frequency response in a solution with a pH of 7. (b) Resonant frequency responses in a solution with a pH of 4, directly after immersion and after 2 hours. (c) Resonant frequency responses in a solution with a pH of 10, directly after dipping and after 50 min. The curves show no change.*

4.4.7 Tip Wear and Tip Overcoating

Photoplastic tips are made of soft material, hence they are more subject to wear than silicon or silicon nitride tips. Depending on the operation mode used and of the hardness of the substrate, wear of SU-8 tips can be a major problem. Figure 4.22 shows a tip before and after imaging of a silicon dioxide sample in contact mode. The tip shows clear evidence of wear. In tapping mode, where the tip just lightly hits the sample, wear is less critical, but the tip performance can also be degraded when it does occur. On the other hand, a soft tip is advantageous for imaging fragile samples like biological materials, because the risk of damaging the investigated sample is reduced. Figure 4.23 illustrates that the tip showed no wear after images such as those in Figures 4.18 and 4.19 were taken in tapping mode.

Tip wear can be avoided or reduced by using a hard material overcoating. Photoplastic tips have been successfully coated with Diamond Like Coating (DLC) and used for imaging. Preliminary results show that the coating seems to improve the hardness of the tips, thus reducing the wear problem, without affecting the image quality [91]. However, further carefully designed experiments need to be done to confirm these results.

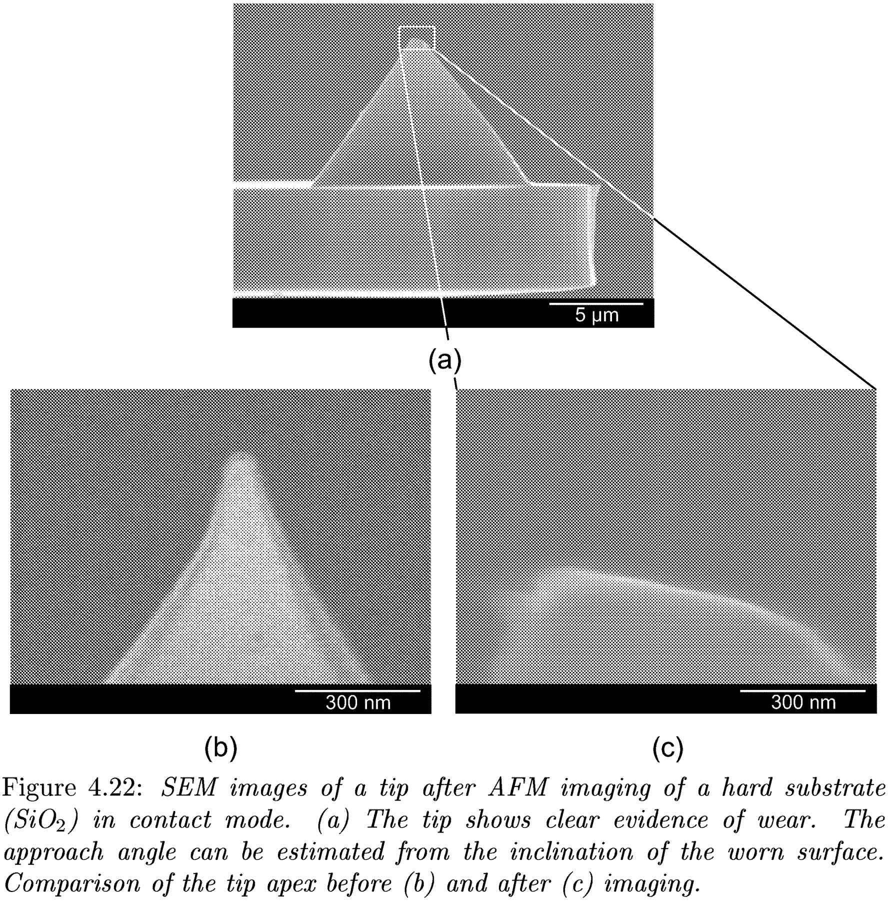

Figure 4.22: *SEM images of a tip after AFM imaging of a hard substrate (SiO_2) in contact mode. (a) The tip shows clear evidence of wear. The approach angle can be estimated from the inclination of the worn surface. Comparison of the tip apex before (b) and after (c) imaging.*

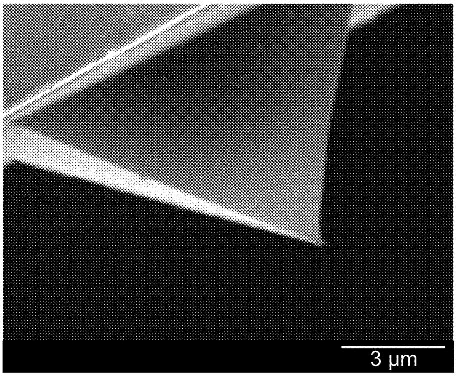

Figure 4.23: *SEM image of a tip after AFM imaging of soft samples in tapping mode. The tip shows no wear after imaging. The double tip comes from material that has been picked-up from the sample during imaging.*

4.5 Conclusions and Perspectives

The fabrication of a new kind of soft photoplastic SFM probes with integrated tips has been demonstrated. The simple molding and replication techniques employed show potential for the fabrication of low-cost, large-volume photoplastic AFM probes with soft tips. In contrast with more conventional fabrication methods, probe releasing allows mold substrates to be reused several times and avoids the need to etch through, or dissolve, an entire wafer. The possibility of spin-coating thin layers (< 1 μm) also holds promise for the fabrication of very soft cantilevers. In addition, tip hardening by use of overcoating is expected to reduce the wear issue, and may lead to very broad applications for such probes. Finally, the integration of sensing elements on the lever could lead to far more versatile probes. Such integrated sensing could be achieved by depositing piezoelectric [68] or piezoresistive layers on the lever, like tin oxide (SnO_2) [92], graphite/polyimide thin films [93], or even doped SU-8.

Chapter 5

AFM Cantilever Cassette

5.1 Introduction

In scanning probe microscopy (SPM), single cantilevers are mounted in the microscope and used as long as their tips perform well for the image resolution required. Defective cantilevers are replaced by mounting a new cantilever probe in the apparatus. This change of cantilever requires readjustments of the laser detection system and of the operation parameters, which can be rather time consuming. This is even more problematic when operating the cantilever in a nonconventional environment where cantilever replacement is difficult or impossible. A cassette of cantilevers with several spare probes can greatly reduce the time required to replace and adjust damaged cantilevers. The cassette, in conjunction with an appropriate holder, allows the damaged cantilever to be broken off and replaced with a new spare with the same mechanical properties.

5.2 Cantilever Cassette Design

A one-dimensional (1D) array arrangement of cantilevers allows spare cantilevers to be integrated on the same chip as the front cantilever, which is used to scan the sample, Figure 5.1(a). Whenever the front one needs to be replaced, because the tip or cantilever is damaged or dirty, a stylus is pushed down from the above to break off the front lever, and the next lever is pushed into operating position, Figure 5.1(b). This concept of having spare cantilevers relies on the integration of several probes with very similar properties on the same chip, in order to make the cantilever replacement and adjustment much easier. Precise alignment grooves and notches on the cantilever cassette and sample holder allow for a self-aligned positioning of the next lever into the operation position of the removed front lever. The cantilever cassettes presented were fabricated using SU-8 photoplastic material for the entire chip, that is for the tips, the levers, and the body of the probe.

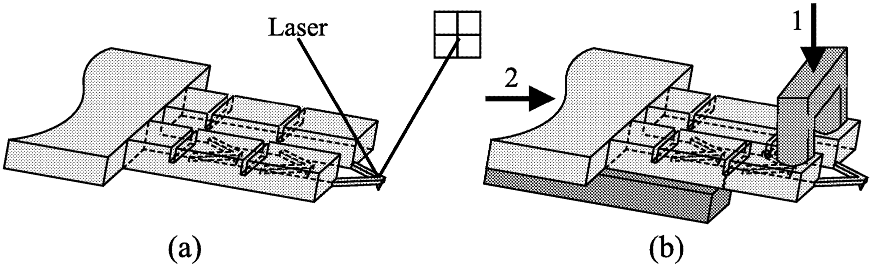

Figure 5.1: *Cantilever cassette principle. (a) The first cantilever is used for scanning and spare cantilevers are arranged in a 1D column array behind the first one. (b) A stylus (1) is pushed down to break off the damaged cantilever so that the first spare cantilever can be pushed (2) into the same position as the old one. This working position is precisely determined by mechanical alignment structures on cassette and holder.*

5.3 Fabrication

The fabrication process for photoplastic cantilever cassettes is similar to that for the single lever photoplastic AFM probes described in chapter 4.4 and is based on spin-coating, near-UV exposure, and development of SU-8 photoresist on a prestructured silicon wafer, as shown in Figure 5.2. In order to facilitate alignment of the thick resist layers, alignment marks are first etched into the back side of a double-side polished 100 mm ⟨100⟩ silicon wafer, (Figure 5.2(a)). After tip mold definition on the front side of the silicon wafer, oxidation sharpening and sacrificial layer deposition (Figure 5.2(b)), the cantilevers are defined by a first photoresist layer on the prestructured wafer, (Figure 5.2(c)). After development of the levers layer (Figure 5.2(d)), a thicker layer (about 200 μm) of SU-8 is spin coated to yield the first body layer, (Figure 5.2(e)). After exposure of this layer, another thick (200–300 μm) body layer is spin coated and exposed, (Figure 5.2(f)). Both layers are then simultaneously developed, (Figure 5.2(g)). Finally, the chips are released mechanically from the silicon wafer mold, (Figure 5.2(h)). The purpose of the second body layer is to clearly define the breaking-off position between cantilevers by means of well-defined trenches. After releasing of the chips, the wafer mold is cleaned to be ready for reuse.

Figure 5.3 shows SEMs of a fabricated SU-8 SFM cantilever cassette with integrated sharp tips. On this design, each cassette is composed of 5 identical cantilevers. Cantilevers with different shapes can also be integrated on the same chip. The only limitation is that they will all have the same thickness. Both triangular and beam–shaped cantilevers have been fabricated.

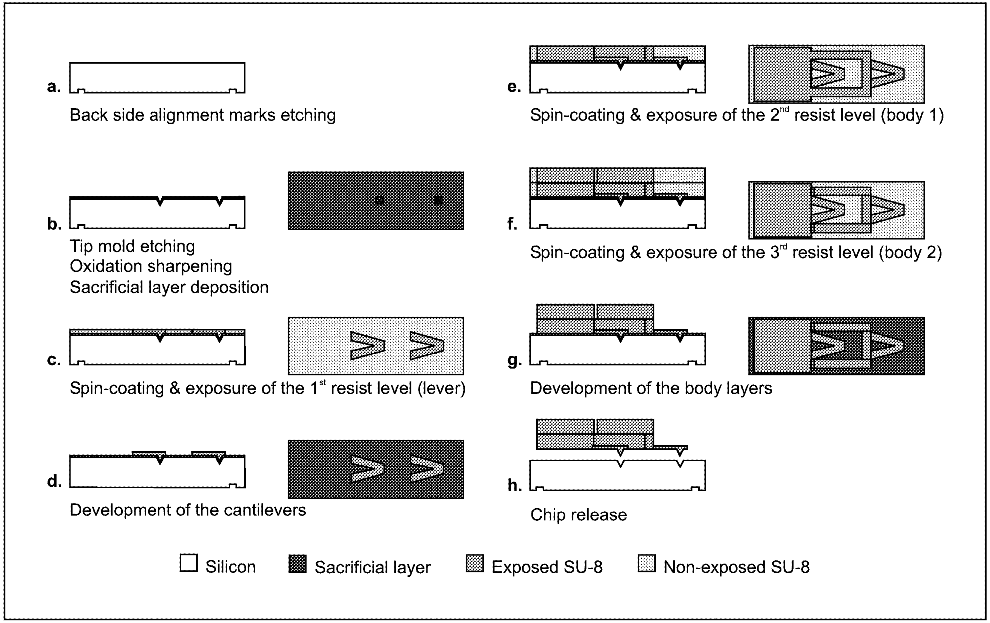

Figure 5.2: *Outline of the process sequence for the fabrication of photoplastic AFM cantilever cassette probes. (a) Alignment marks are etched into the back side of the wafer for easier alignment of thick resist layers. (b) Pyramidal hole formation, oxidation sharpening and sacrificial layer deposition. (c) Spin-coating and exposure of SU-8 cantilevers; integrated tips are formed by the resist filling the pyramidal pit. (d) Development of the cantilevers. (e) Spin-coating and exposure of the first layer for the body. (f) Spin-coating and exposure of the second body layer with trenches to allow tips to be broken off. (g) Development of the two body layers. (h) Demolding of the entire cassette chip.*

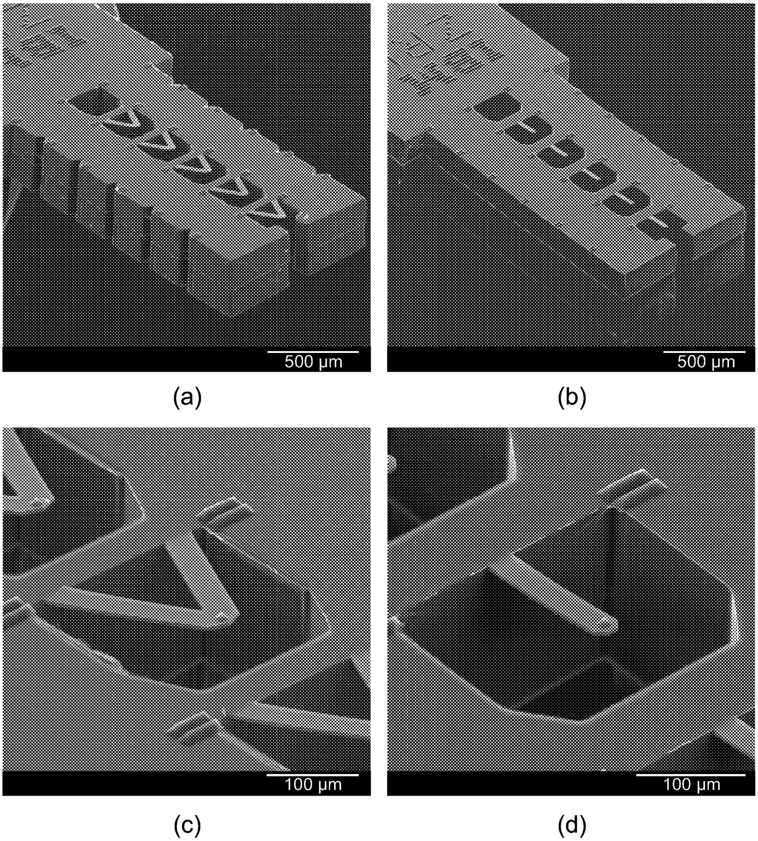

(a) (b) (c) (d)

Figure 5.3: *SEMs of fabricated SU-8 cantilever cassette probes. Each cassette is composed of 5 identical levers. The first lever is protected for ease of handling. (a) Cassette with triangular cantilevers. (b) Cassette with rectangular beam cantilevers. (c) Closeup of a triangular cantilever with integrated tip. The lever is 190 μm long, 40 μm wide and 5.3 μm thick. (d) Closeup of a rectangular beam cantilever with integrated tip. The lever is 160 μm long, 30 μm wide and 5.3 μm thick.*

5.4 Probe Characteristics

Cantilevers presented in Figure 5.3 are 190 μm long, 40 μm wide for the triangle-shaped levers (Figure 5.3(c)), and 160 μm long, 30 μm wide for the beams (Figure 5.3(d)). The thickness of both types of cantilevers is around 5.3 μm. These dimensions yield a theoretical stiffness of 0.86 and 1.1 N/m, respectively, with corresponding resonant frequencies of 43.5 and 61.4 kHz. Measured resonant frequencies differ by less than 3% from the theoretical ones. This difference is mainly due to the limited measurement accuracy of the lever dimensions and of the resonant frequencies, as well as to uncertainties on the mechanical properties of the SU-8 material. The close proximity and the well-controlled lever thickness given by the spin-coating process yield uniform mechanical characteristics of the levers within a cassette, as shown by the frequency responses in Figure 5.4: cantilevers within the cassette have a mean resonant frequency of 69 kHz and a mean Q factor of 30, with a very good uniformity as can be deducted from the similar shape of the curves. The resonant frequencies of the different levers are within 2% of the average value of the resonant frequency for the cassette. This uniformity of the mechanical properties is also very good between cassettes fabricated on a 4-in. silicon wafer mold (Figure 5.5). This excellent reproducibility of the mechanical properties within and between cassettes is important for practical use because it implies that only slight changes of the cantilever driving parameters are needed after changing the probes.

5.4.1 Breaking-off Position

Breaking-off location and control as well as cassette positioning accuracy is of great importance for the practical use of multiple single-lever probes. In the 1D array arrangement presented, cantilevers are attached to the chip body via two supporting arms. Breaking-off positions are defined by locally weakening the supporting arms between each cantilever. Breaking-off is performed by applying a force onto the sliding arms. If adequate support is present under

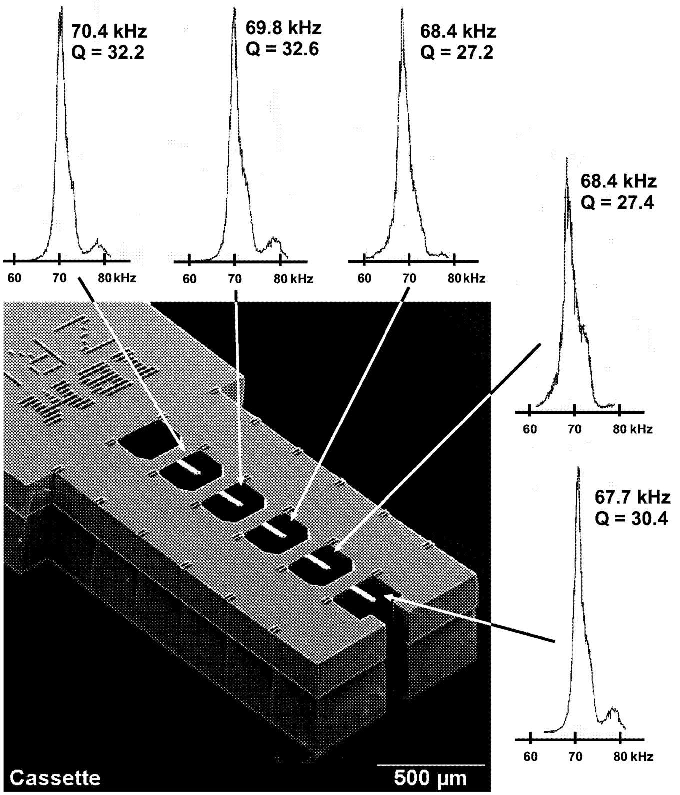

Figure 5.4: *Normalized resonant frequency responses of cantilever beams within a same cassette. The mean resonant frequency of the cantilevers is 69 kHz and the mean Q factor is 30. The standard deviation within the cassette for resonant frequencies and Q factor are 1.1 kHz and 2.3, respectively.*

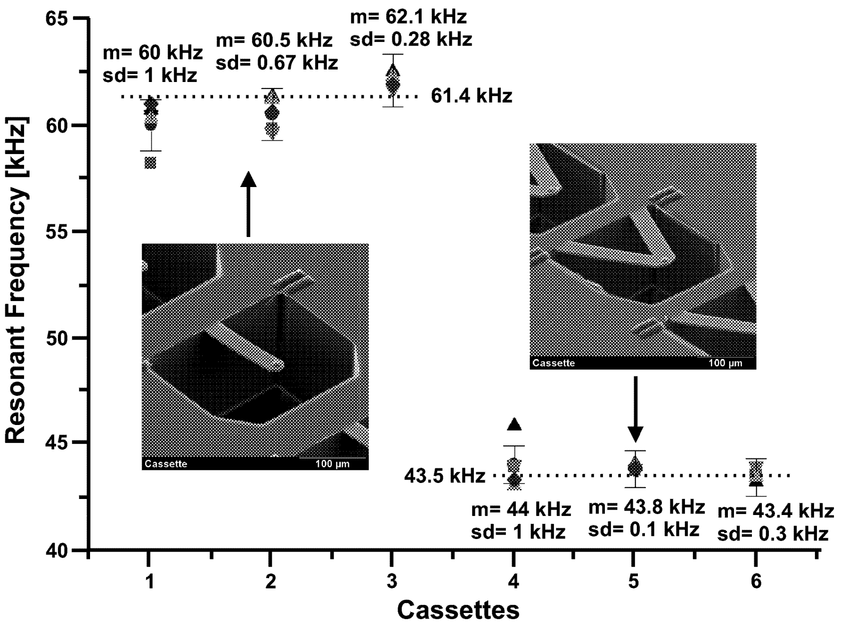

Figure 5.5: *Uniformity of the resonant frequency of the cantilevers (beam and triangle shape) within a cassette and between different cassettes. The error bar for each cassette was set to 2% of the average value of the resonant frequency of the levers of the cassette. The theoretical resonant frequency for the beams and triangle levers of the measured cassettes are 61.4 and 43.5 kHz respectively. The mean value and standard deviation of the resonant frequency of each of the six cassettes measured are shown.*

the weak zone of the part of the sliding arm to be broken off, a well-controlled fracture can be produced, see Figure 5.6.

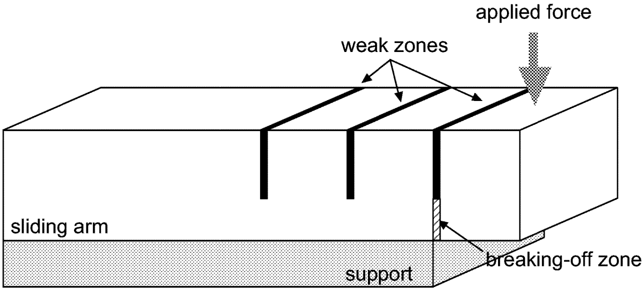

Figure 5.6: *Schematic of the breaking-off principle. A support is positioned under the sliding arm so that its edge is underneath the weak zone to be broken off. Application of a force on the part to be removed breaks the sliding arms at the location defined by the first weak zone.*

In a first design, the chip body was formed only by one SU-8 layer. Weak zones were defined by partially developed trenches structured into the sliding arms. The development depth of these trenches was controlled indirectly via the limited aspect ratio obtainable with SU-8. A maximum aspect ratio of 17 has been demonstrated with a 43-μm wide trench. (see Figure 5.7 [25]). Weak zones based on 30-μm wide trenches were designed across the supporting arms, while making the body layers thick enough so that the trenches are not completely developed. This approach for determining the breaking-off location proved very difficult to control because the photoresist exposure depends strongly on the thickness of the chip body resist layer. Moreover, reproducible development of thick SU-8 trenches is very difficult to achieve. Hence, breaking-off does not always occur at the weak zone, the latter being unsufficiently defined with this method, Figure 5.8.

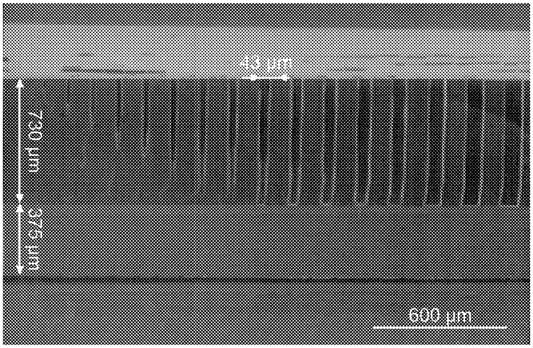

Figure 5.7: *An maximum aspect ratio of 17 is demonstrated with a 43-µm wide and 730-µm deep developed trench. Adapted from [25] with permission.*

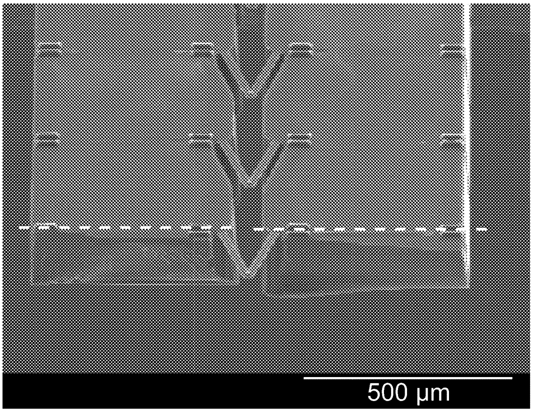

Figure 5.8: *SEM of a cassette after breaking-off of a cantilever. The dashed line indicates the weak zone defined by the partially developed trench. A breaking force was applied from the other side of the chip, opposite to the cantilevers, breaking-off does not occur exactly where desired.*

In a second design, a 2–layer approach for chip body formation has been investigated. A first body layer that holds the cantilever to the sliding arms is patterned without trenches. A second body layer, patterned with trenches, is then used to define the breaking-off locations. The well-defined trench in the second body layer allows a much more controllable breaking-off. Figure 5.9(a) shows a cassette after successful breaking-off of a defective cantilever. In the geometry used, new cantilevers are attached to the chip body through the first resist layer. Figure 5.9(b) shows a closeup of a defined weak zone.

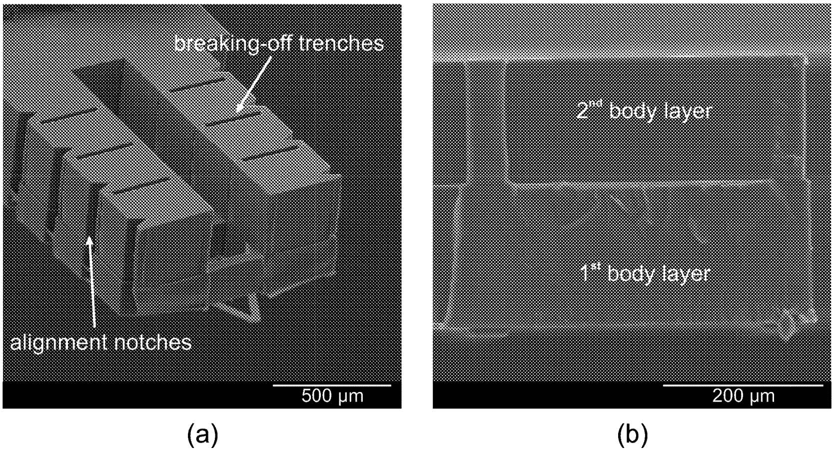

Figure 5.9: *SEMs of a cassette after breaking-off of a defective cantilever. (a) The first body layer holds the levers to the chip. The second body layer with well-defined trenches locates precisely breaking-off positions. Notches on the side of the sliding arms allows accurate alignment of the cantilever cassette. (b) Front view of a sliding arm after breaking-off. Trench depth is given by the second body layer's thickness.*

5.5 Concept Demonstration

Previous experiments with photoplastic single levers (see paragraph 4.4.6) have shown a lateral resolution of 5–6 nm and a vertical resolution of about 0.1 nm. The performance of the epoxy cantilever cassettes has been investigated in similar atomic force microscopy experiments on DNA-plasmid molecules, using tapping mode under ambient conditions. The cassettes contained rectangular cantilever beams. The resonant frequencies of the cantilever cassettes tested were found to be around 61–62 kHz, and very uniform. For the tapping mode AFM experiments reported, the driving frequency was typically set 1 kHz below resonance. The uniformity in resonant frequency from one cantilever to another was so accurate that we were able to run the various experiments at a preset driving frequency of 60.9 kHz for all cantilevers tested.

As a standard experiment, DNA-plasmids (pGEM-3Zf vector from Promega Corporation, Madison) immobilized on NH_2-functionalized glass were imaged (Figure 5.10). The cassette concept was demonstrated by imaging DNA-plasmids with different cantilevers of a cassette. Figure 5.11(a) shows a single DNA molecule imaged with a deteriorated tip, whereas Figure 5.11(b) shows the same molecule scanned by the first spare cantilever of a cassette, at full resolution. This imaging of the same molecule by two different levers was done with small positional adjustments and without any changes in the operating conditions. Imaging performance with a cantilever from a cassette probe was found to be similar than to that with a single lever photoplastic SFM probe. This demonstrates the potential of the cassette concept for a better ease of operation. It is important to note that the full potential of the cassette concept for future automated applications can only be fully exploited when the cassette is used with a dedicated holder.

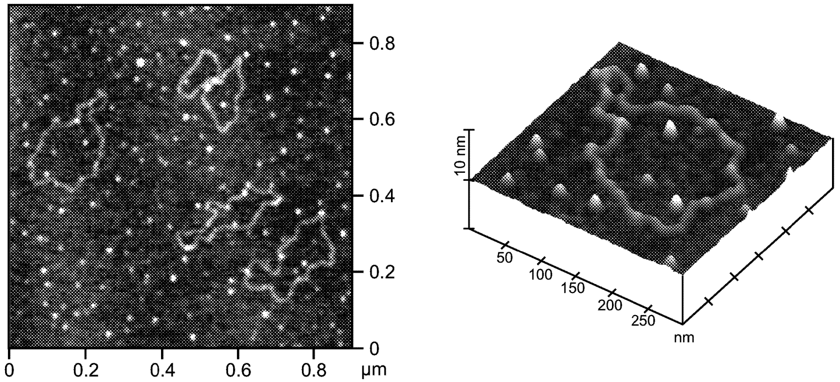

(a) (b)

Figure 5.10: *(a) AFM image (0.9 × 0.9 μm^2) of DNA-plasmid molecules (see the text for details). (b) 3-D Closeup (0.3 × 0.3 μm^2) of a DNA molecule. The width of the DNA is 9 nm. The z scale was color adjusted to 1.5 nm.*

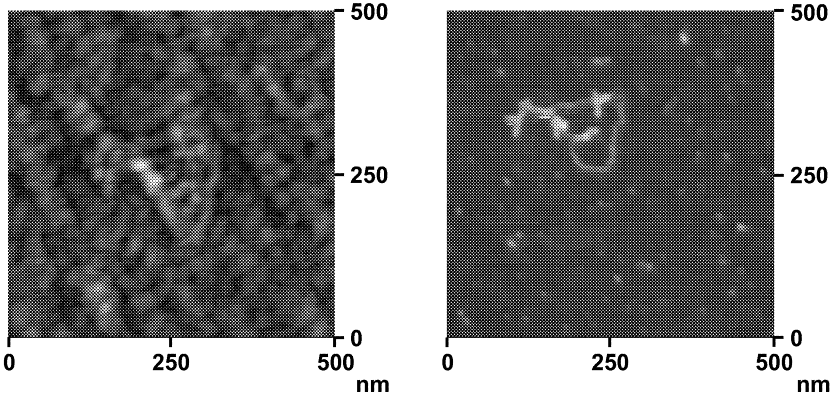

(a) **(b)**

Figure 5.11: *DNA-plasmid molecule imaged with different cantilevers. The z scale was color adjusted to 5 nm. (a) Image of the molecule with a deteriorated tip of the first lever of a cassette. The resolution is very poor. (b) Image of the same molecule with the second lever of a cassette, using a fresh tip.*

5.6 Conclusions

The simple molding and replication techniques used for fabricating low-cost soft AFM cantilevers probes can be extended to more complicated microstructures. The cantilever cassette concept using SU-8 processing demonstrates such possibilities. By introducing a well–defined break–off geometry while maintaining an excellent uniformity of the cantilevers, it shows great potential for future automated applications.

Chapter 6

Photoplastic SNOM Probes

6.1 Introduction

SU-8 technology provides an alternative for the fabrication of Scanning Near-Field Optical Microscopy (SNOM) probes by allowing the combination of well–defined microfabricated features with wave guide elements. SNOM is a scanning probe microscopy technique that allows optical imaging with resolution beyond the diffraction limit of conventional optics. It provides information on the local properties of the sample on a nanometer scale. With conventional optics, the fundamental diffraction limit of resolution, the Abbe barrier [94], is essentially given by the wavelength of the employed radiation λ and the numerical aperture $N.A.$:

$$\Delta x > 0.61 \frac{\lambda}{N.A.} \tag{6.1}$$

which is ~200 nm for visible light. This diffraction limit is not fundamental, and Fourier optics can be used [95, 96] to demonstrate that this limit arises from the assumption that the detection element is typically many wavelengths away from the sample of interest. The electromagnetic field emitted or reflected by a surface consists of propagating modes, which transport energy and evanescent modes of higher spatial frequency. These however, diminish exponentially with distance from the emitting surface. By approaching a probe very close to the surface, that is into the near-field, evanescent modes can be transformed into propagating modes containing optical information of very high spatial frequency. By laterally scanning a source or detector of light in close proximity to the sample, one can generate an image at a resolution which is not limited by diffraction. The image depends on only the probe size and the probe-to-sample separation, each of which can be made much smaller than the wavelength of light (Figure 6.1). Thus, SNOM enables subwavelength resolution by relying on nanoscopic probes that localize the optical interaction to sub-wavelength dimensions [97]. There are many different ways to implement near-field optical imaging, but the most common are the illumination and the collection modes (Figure 6.2). A good overview of the different techniques can be found in Ref. [98].

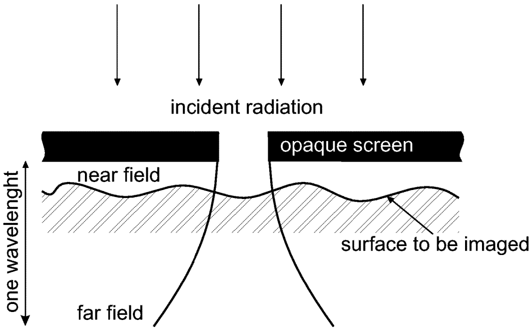

Figure 6.1: *Schematic representation of a radiation emanating from a subwavelength diameter aperture. The size of the beam passing through the aperture is defined by the aperture size in the vicinity of the aperture. Resolution depends on aperture size and aperture–sample separation.*

Like other SPMs, basic elements of a SNOM consist of 1) a probe that localizes the interaction region to subwavelength dimensions, 2) a scanning mechanism that allows the sample to be moved under the probe, and 3) a distance regulation system that controls probe–sample spacing. However,

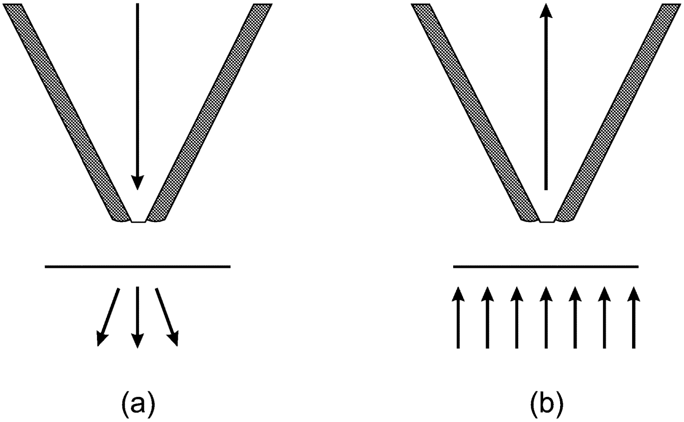

Figure 6.2: *Most common modes of SNOM. (a) SNOM in illumination mode: a probe illuminates the sample, the light is collected in the far field. (b) SNOM in collection mode: a probe collects the light coming through the sample and the sample is illuminated from the far field.*

unlike conventional optical or other scanning probe microscopies, SNOM has to date not evolved into a widely established imaging technique. This is mainly due to the low quality of the probes. It has been especially difficult to fabricate and reproduce well-controlled tips and apertures.

6.2 SNOM Probes

A SNOM probe consists of a subwavelength aperture which is brought in close proximity (a few nanometers) to the sample. Most SNOM probes use a pulled [99, 100] or chemically etched [101] optical fiber which is coated with a thin layer of aluminum. Such probes exhibit easy light coupling and collection of optical information from the tip. The optical aperture can be defined by a shadow when angle evaporating metal on the fiber, or by etching away metal at the tip apex. But it is challenging to fabricate well-controlled, reproducible apertures by these methods, mainly due to the difficulty of obtaining an opaque metallic layer of sufficient quality. Pinholes in the aluminum layer and grains protruding at the tip apex are common flaws responsible for poor probe performance. Various aperture fabrication techniques based on microtechnology have been proposed to overcome these problems and improve the fabrication of probes with well-determined shape and size. Microfabricated silicon nitride tips attached to optical fibers have been proposed [102]. Microfabricated probes can also combine AFM and SNOM techniques, by defining an optical aperture at the apex of an AFM tip. Silicon [103], silicon nitride [104], silicon oxide [105], solid quartz (fused silica) [106], and molded metallic [107] tips at the end of a silicon cantilever have been fabricated and used for imaging.

In this chapter, a technique based on micromachining technology for fabricating well-defined, reproducible, subwalength photoplastic probes with integrated apertures is presented. In order to combine both the wave guide properties of optical fibers and the reproducibility of batch-processing techniques, we first developed a hybrid probe consisting of a photoplastic part attached to an optical fiber (Figure 6.3) [108]. This hybrid arrangement allows light to be guided through the fiber to within a few micrometers of the well-defined, smooth tip. The fabrication techniques used can be easily extended for the fabrication of a combined AFM/SNOM probe using photoplastic cantilevers.

6.3 Design and Fabrication of the Photoplastic Probe

The micromachined photoplastic part of the probe consists of a tip centered with a ring–shaped guiding structure for easy and accurate tip–fiber alignment and assembly. In designing the photoplastic part, two major points have been focused on: the tip size and the circular guiding structure for aligning the optical fiber and the tip.

Absorption losses of SU-8 are very small in the dimensions of the tip and

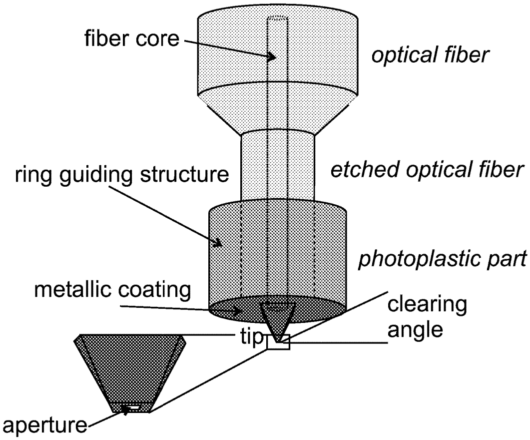

Figure 6.3: *Schematic of the hybrid SNOM probe with a photoplastic part attached to a partially etched optical fiber and an aperture formed at the tip apex.*

for the wavelengths used. The attenuation factor is 1 to 1.5 dB/mm for light wavelengths λ of 500 nm to 1580 nm, and the refractive index is 1.599 [109]. This gives a transmission of more than 99 % through a 20-μm thick SU-8 layer of light coming from the glass fiber, and light absorption can be neglected. A simple ray-tracing analysis was performed to determine the optimal tip size. When the tip base diameter is exactly the same as the fiber core size (4 μm), 20 % of the light is transmitted. By increasing the tip diameter, transmission increases to reach a theoretical maximal value given by any diameter above 16 μm. In order to have minimum losses from material and geometry, a minimum tip base of 12 μm, which gives a tip height of 8.5 μm and a transmission of 95% of the coupled light has been chosen.

To improve the mechanical response of the probe and achieve sufficient probe–sample clearance, the lateral dimensions of the guiding structure have to be small. This has been achieved by chemically etching 125-μm fibers down to diameters of less than 50 μm [110], thus reducing the outer diameter of the probe. Figure 6.4 illustrates the gain in clearing angle obtained by using optical fibers with reduced outer diameter.

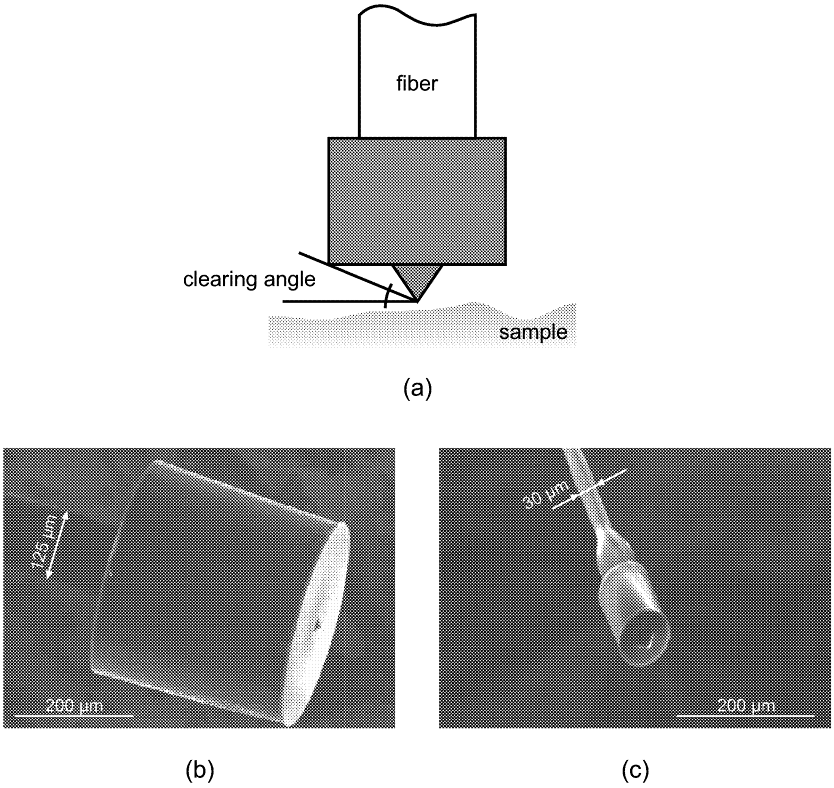

(a)

(b) (c)

Figure 6.4: *(a) Clearing angle depends on both the outer diameter of the ring guiding structure and the tip height. (b) A 125-μm fiber attached to a 370-μm ring gives a clearing angle < 3 ° for a 8.5-μm high tip. (c) Partially etched optical fiber permits to have a ring guiding structure with a much smaller outer diameter. A 30-μm fiber allows to have a ring as small as 80 μm, leading to a clearing angle of 12 °.*

6.4 Fabrication and Assembly

The fabrication process for the photoplastic part of the SNOM probe uses standard microfabrication techniques and is similar to that for photoplastic probes for scanning force microscopy (see sections 4.4 and 5.3), but with additional steps for the aperture formation. Figure 6.5 describes the process sequence for the fabrication of hybrid SU-8 SNOM probes with integrated apertures. The starting substrate is a 4-in., ⟨100⟩–oriented, 525-μm thick Silicon-On-Insulator (SOI) wafer with a 10-μm thick Si membrane and a 0.5-μm buried oxide layer (BOX), (Figure 6.5(a)). To combine aperture and photoplastic fabrication, a pyramidal hole is first etched in the device layer through a thermally grown and structured oxide mask using a combination of potassium hydroxide (KOH) and tetramethyl ammonium hydroxide (TMAH) anisotropic wet etching. Etching in KOH (40%wt, 60°C) is performed until the four (111) planes of the pyramidal hole intercept each other but before reaching the BOX of the wafer. Controlled overetching of the (111) planes using TMAH (25%wt, 85°C) is then performed until a 200 to 300-nm platform is formed on the BOX, (Figure 6.5(b)). TMAH wet etchant is used for the fine tuning of the platform size because of its slow etching rate of the Si (111) planes of 1.3 μm/h. The platform dimensions are measured by means of a SEM investigation. A cavity is then formed at the bottom of the pyramidal mold by etching away the buried oxide using buffered hydrofluoric acid (BHF), (Figure 6.5(c)). After deposition of a sputtered Au/Cr sacrificial layer (see chapter 3), the aperture is defined by evaporating aluminum in the pyramidal hole. Sidewalls of the inverted pyramids are aluminum coated, and an opening is formed at the bottom of the tip owing to the cavity in the BOX, (Figure 6.5(d)).

Next, the first layer of 6 μm of SU-8 is spin-coated onto the wafer, UV-exposed and developed. The photoplastic probe tip is defined by the resist that fills up the etched pyramidal hole, (Figure 6.5(e)). The alignment guide for the fiber is made by spin-coating, exposing, and developing a second, 160-μm thick layer of SU-8, (Figure 6.5(f)). The guide is centered with respect to the tip with the micrometer precision given by the overlay capability of the optical exposure tool. This results in an accurate fiber-to-probe alignment assembly. Once the photoplastic probes have been fabricated on a wafer scale, an optical fiber of reduced diameter is dipped into glue and inserted into the photoplastic guide using micropositioners, (Figure 6.5(g)). SU-8 is also used as glue in the fiber-photoplastic part of the attachment to avoid refractive index-matching problems given by interfaces along the light path. After curing of the SU-8, the sacrificial layer is etched and the glued fiber is retracted, thereby releasing the photoplastic tip and the metallic aperture from the mold, (Figure 6.5(h)). After cleaning, the silicon mold is ready for reuse.

The fibers used for attachment to the photoplastic parts are partially etched monomode fibers with an original cladding diameter of 125 μm and a core diameter of 4 μm. Fibers are etched in hydrofluoric acid (HF, 40% wt) at room temperature to diameters 1–2 μm smaller than the hole diameter of the ring guiding structures, which have nominal diameters of 30, 40, and 50 μm. The etch rate of the fiber in HF is around 2.2 μm/min. Fiber diameter etching is very well-controlled and takes 35–55 min. for the desired final diameters (Figure 6.6).

Figure 6.7 shows a fabricated photoplastic part of the probe on the wafer (cf. Figure 6.5(f)) ready for to be attached to an optical fiber for releasing. The ring-shaped guiding structure is well-defined by a simple masked exposure and subsequent development of a layer of SU-8. Ring guiding structure SU-8 layer fabrication parameters have been optimized to obtain nearly vertical sidewalls.

Figure 6.8 shows SEMs of fabricated and released hybrid SU-8 SNOM probes with a metallic aperture and a flat end. Metallic coating of very good quality is transferred from the mold to the underside of the SU-8 probe upon etching of the sacrificial layer during releasing steps. Figure 6.9 shows optical images of the bottom of probes with and without metallic coating.

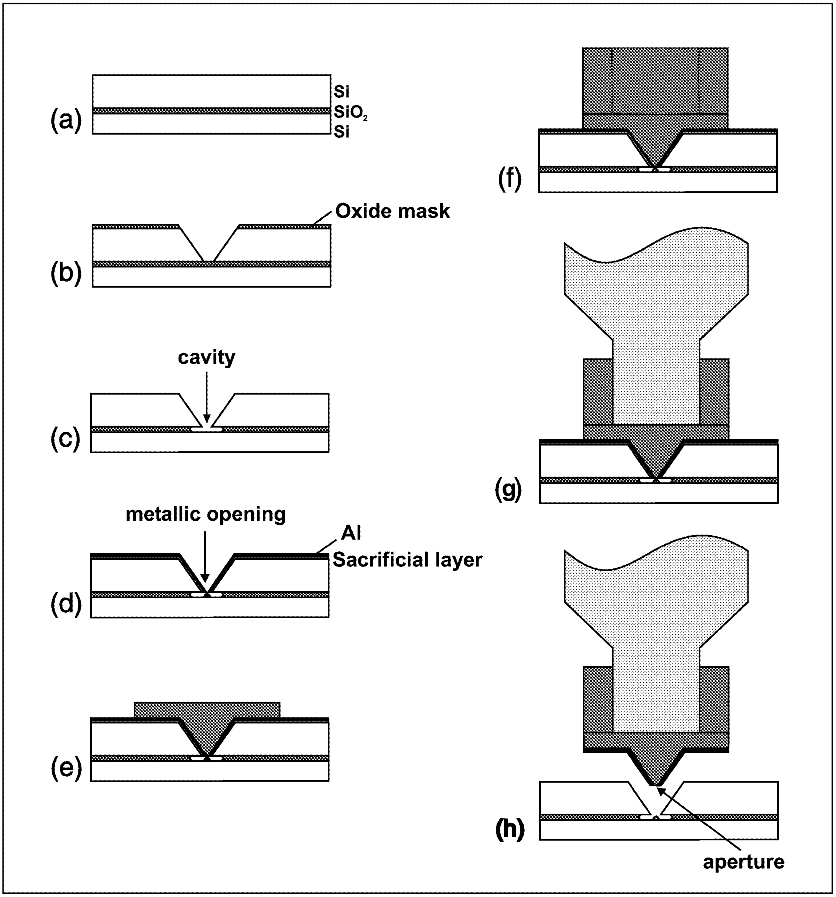

Figure 6.5: *Process sequence for the fabrication and assembly of the hybrid photoplastic/optical fiber SNOM probe. (a) The starting substrate is a* ⟨100⟩*-oriented, 525-μm thick SOI wafer with a 10-μm thick Si membrane and a 0.5-μm buried oxide layer. (b) Pyramidal holes are first etched in the membrane of the SOI wafer through an oxide mask until a 200 to 300-nm platform remains on the BOX. (c) The BOX is etched to form a cavity at the bottom of the pyramidal pit. (d) The sacrificial layer and aluminum are deposited, thus defining the aperture. (e)–(f) Photoplastic part is fabricated on the prestructured SOI wafer. (g) Etched optical fiber is approached and glued to the tip. (h) Tip and aperture are released by etching the sacrificial layer and retracting the fiber.*

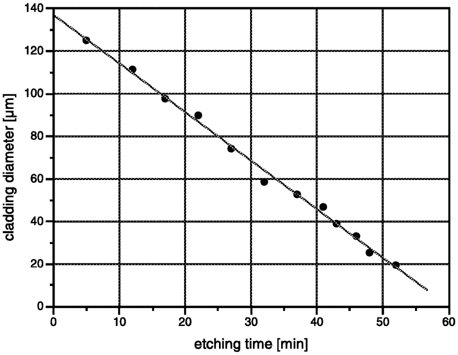

Figure 6.6: *Optical fiber cladding etching. Linear etching allows a good control on the final fiber diameter. Etching is performed in HF 40% wt at room temperature.*

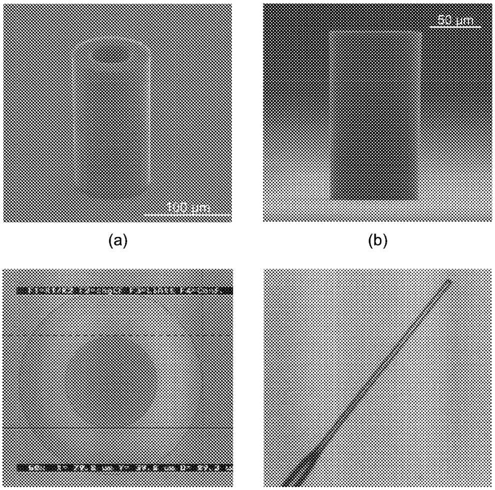

(a) (b)

(c) (d)

Figure 6.7: *SU-8 photoplastic probe part on the wafer prior to attachment to an optical fiber and releasing. (a) SEM of a tube. The guiding structure is 160 µm high. The outer diameter of the guide is 90 µm and the hole diameter is 45 µm. (b) SEM of the sideview of the tube showing the vertical sidewalls of the structure. (c) Optical image of a tube from the top. Outer diameter is 80 µm, and inner diameter is 40 µm. (d) Optical micrograph of a pre-etched optical fiber ready to be introduced into the photoplastic part of the probe.*

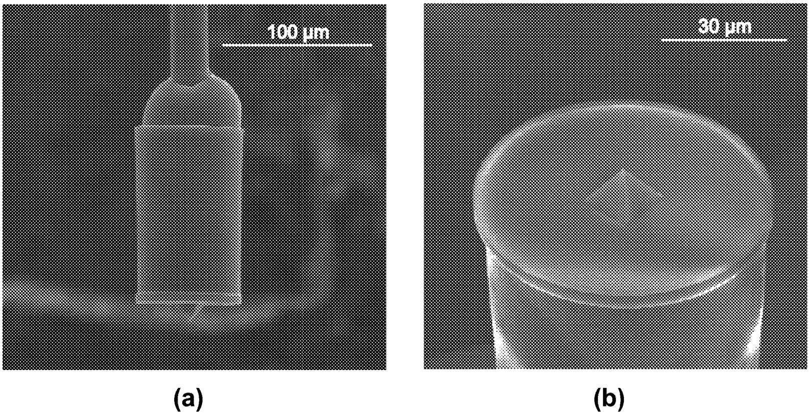

Figure 6.8: *SEMs of a fabricated SNOM probe. (a) General view of a photoplastic probe attached to a partially etched optical fiber. (b) View of the coated tip.*

The same method can be extended to the fabrication of an integrated AFM/SNOM probe [104, 105, 107, 110]. In such a concept, simpler distance regulation and topographical imaging are possible by using a cantilever deflection. Fabrication process is similar to that for photoplastic cantilevers. The tip mold is made with an SOI wafer with prestructured apertures. The ring guiding structure of the fiber-based probe is replaced by the chip body of the cantilever probe. Figure 6.10 demonstrates a possible adaptation of the process showing the process sequence and fabricated photoplastic cantilevers with an aluminum coating on the underside which was transferred during release from the mold. This process extension shows good potential for combined arrays of AFM/SNOM probes. These cantilever-based SNOM probes have not been tested as a new SNOM set-up, where light is focused at the end of the lever, has yet to be assembled.

6.5 Aperture Formation

Subwavelength apertures at the end of a SNOM tip are used to eliminate far-field contributions to the optical signal. Optical aperture formation is

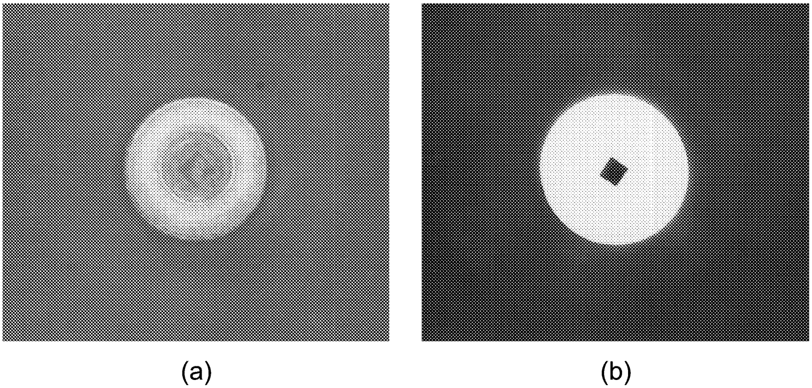

Figure 6.9: *Optical micrographs of the underside of photoplastic probes. (a) No aluminum was deposited on top of the sacrificial layer at the wafer level, hence no coating is on the probe after releasing. (b) Aluminum deposited on top of the sacrificial layer is transferred to the probe during releasing. Homogeneous metallic coating is on the all underside of the probe, including the tip.*

thus a key process for obtaining high quality SNOM probes. In fiber-based probes, such apertures are obtained by evaporating metal (usually aluminum) onto the fiber from an angle perpendicular to the fiber axis while rotating the fiber. This results in coated sidewalls of the fiber while the tip end remains uncoated. However, the evaporation process is difficult to control and commonly results in deficiencies such as an undetermined shape and size of the opening and light transmitting pinholes on the sidewalls of the fiber probe. Additionally, it creates voluminous metal clusters protruding irregularly from the aperture rim. Those may lead to a larger than optimal separation of fiber tip and sample. The absence of a clean opening also results in low throughput of the probe and poor optical resolution of the SNOM. Moreover, the angle-evaporation procedure is very time consuming and does not lead to a batch fabrication of reproducible, well-defined apertures.

A complete coating of the tip followed by a local etching of the tip's

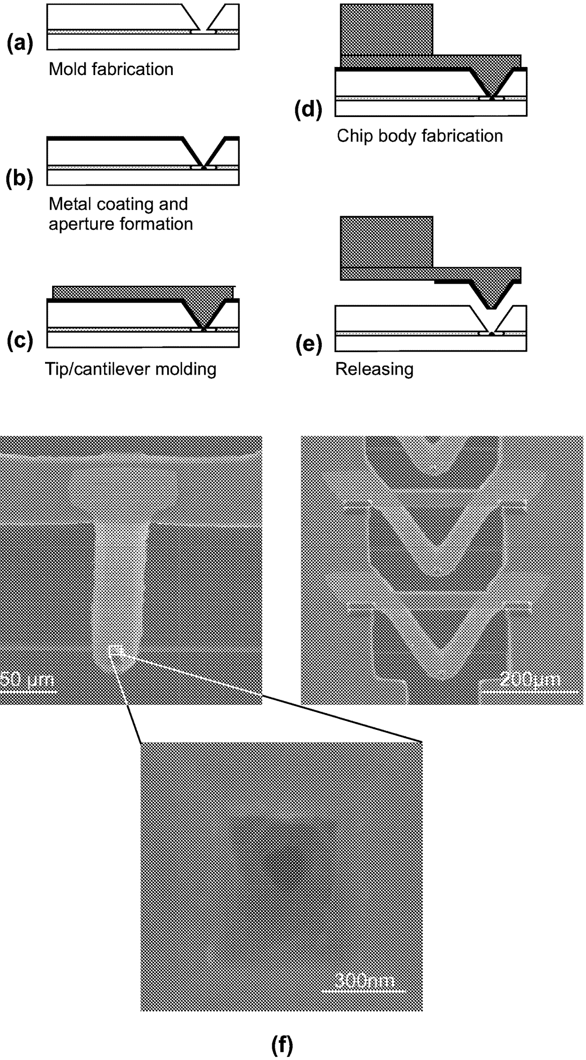

Figure 6.10: *Process sequence for the fabrication of a combined AFM/SNOM probe using photoplastic cantilevers. (a) Mold with a cavity at the bottom of a pyramidal pit is first defined in the wafer (cf. fiber-based SNOM probes). (b) Sacrificial and optical barrier layers deposition. (c)-(d) Photoplastic and chip body fabrication. (e) Probe releasing. (f) SEMs of fabricated single and multiple single levers with the metallic coating transferred, and view of an aperture at the tip apex.*

apex allows fabrication of well-defined apertures with flat ends. Electrolytic erosion [111] or Focused Ion Beam (FIB) milling [112, 113, 114] of the tip's apex lead to small, metal free apertures with flat ends. Nevertheless, even with these techniques, each probe needs to be treated separately, preventing batch fabrication.

We developed a technique based on micromachining and thin film technology to fabricate optical apertures for photoplastic SNOM probes on a wafer level. Aperture fabrication steps are described in detail in section 6.4. A critical processing step is the platform formation. Controlled overetching of the (111)–planes has to be performed in order to obtain a small platform on the BOX of the SOI (see Figure 6.5(b)). This platform determines the size of the cavity. (111)–plane etching is monitored using test structures, so that overetching can be stopped when the desired platform size is obtained. Figure 6.11(a) shows the cavity at the bottom of a pyramidal hole. Figure 6.11(b) shows the same cavity after deposition of sacrificial layer and aluminum coating to leave a small aperture. The aperture size is then strongly dependent on the quantity of aluminum deposited and on the platform dimensions.

Figure 6.12(a) shows a 200-nm×200-nm aperture, whereas Figure 6.12(b) shows a 50-nm×130-nm aperture, which demonstrates the potential of our technique for fabricating small apertures. Rectangular apertures are due to some asymmetries during platform formation. As the aperture is formed during metal evaporation onto the mold, no postprocessing is necessary.

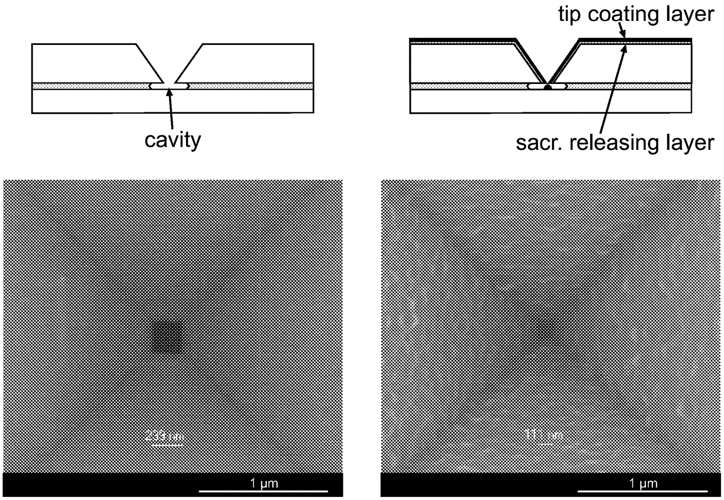

(a) (b)

Figure 6.11: *SEMs of the bottom of a pyramidal hole during aperture formation. (a) After controlled overetching of the (111)–planes of the pyramidal pit, BOX is etched to form a cavity with a 200 to 300-nm opening. Measurement indicates a hole of ∼240 nm. (b) Deposition of sacrificial layer and aluminum coating reduces the opening to form the optical aperture at the bottom of the mold. Measurement indicates an aperture of ∼110 nm*

6.6 Probe Mechanical Characterization

6.6.1 Theory

As the hybrid, fiber-based probe also serves to measure sample topography and regulate probe–sample distance using the shear-force technique, it is important to know its mechanical characteristics.

As described in Appendix A, the equation of motion for the free vibrations of a prismatic beam is given by

$$\frac{EI}{\rho S(x)}\frac{\partial^4 y(x,t)}{\partial x^4}+\frac{\partial^2 y(x,t)}{\partial t^2}=0. \tag{6.2}$$

where E, I, ρ and $S(x)$ are the Young's modulus of the material, the moment of inertia, the material's density, and the beam's cross section area,

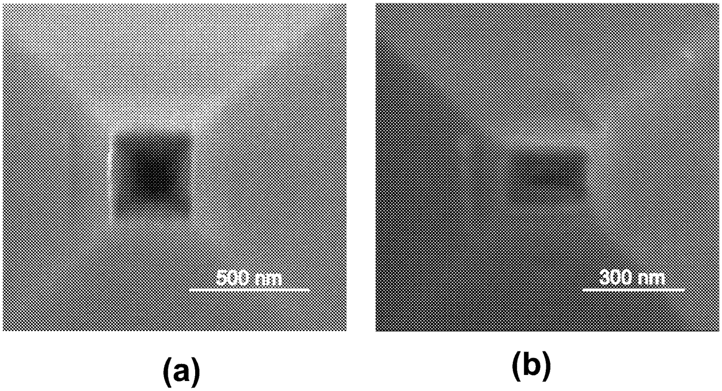

Figure 6.12: *SEMs of the tip apex of released probes. (a) Closeup of a 200-nm×200-nm aperture (d) Closeup of a 50-nm×130-nm aperture.*

respectively.

To avoid the integration of Equation 6.2, we can determine the angular frequency ω of a characteristic vibration mode (usually the fundamental mode) using the Rayleigh method, assuming that:

1. The mode is of the form

$$y(x,t) = y(x)\cos\omega t, \tag{6.3}$$

2. $y(x)$ is chosen to fulfill the boundary conditions on the beam,
3. the maximum potential and kinetic energies are equal during one period (i.e. the oscillation is dissipationless).

The maximum kinetic energy of an element of the beam of mass $dm = \mu_l\, dx$, where μ_l is the cantilever material linear density, can be written as

$$\mathrm{d}T = \frac{1}{2}\mu_l \mathrm{d}x \left(\frac{\partial y}{\partial t}\right)^2_{max} = \frac{1}{2}\mathrm{d}m\ v^2_{max} \tag{6.4}$$

From the first assumption $y(x,t) = y(x)\cos(\omega t)$, we find

$$\frac{\partial y}{\partial t} = -\omega y(x)\sin(\omega t) \Rightarrow \left(\frac{\partial y}{\partial t}\right)_{max} = -\omega y(x) \tag{6.5}$$

Substitution of Equation 6.5 into Equation 6.4 gives

$$\mathrm{d}T = \frac{1}{2}\omega^2 \mu_l y^2(x)\mathrm{d}x. \tag{6.6}$$

Thus, a beam of length L and constant cross-section will have a maximum kinetic energy of

$$T = \frac{1}{2}\omega^2 \mu_l \int_0^L y^2(x)\mathrm{d}x. \tag{6.7}$$

The maximum potential energy due to the bending moment M_b is given by

$$V = \int \frac{{M_b}^2(x)}{2EI}\mathrm{d}x. \tag{6.8}$$

The bending moment is proportional to the second derivative of the deformation $y''(x)$

$$M_b(x) = -EIy''(x) \tag{6.9}$$

which gives

$$V = \frac{1}{2}EI \int_0^L y''^2(x)\mathrm{d}x. \tag{6.10}$$

Equations 6.7 and 6.10 are then equated and solved to determine the angular frequency ω.

The fiber attached to a ferrule is like a cantilever beam of circular cross-section (Figure 6.13).

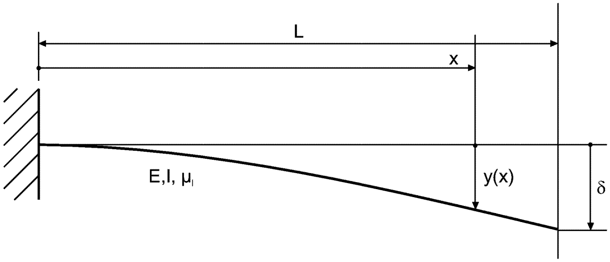

Figure 6.13: *Flexure of a cantilever beam.*

Assuming that fiber deformation $y(x)$ is

$$y(x) = \delta(1 - \cos\frac{\pi x}{2L}) \tag{6.11}$$

we have

$$\frac{\mathrm{d}^2 y(x)}{\mathrm{d}x^2} = \frac{\pi^2\delta}{4L^2}\cos\frac{\pi x}{2L} \tag{6.12}$$

This function satisfies the boundary conditions of the fiber in the ferrule: $y(0) = 0$ and $y'(0) = 0$. From Equations 6.7 and 6.10, we find

$$T = \frac{3\pi - 8}{4\pi}\omega^2\mu_l\delta^2 L, \qquad V = \frac{\pi^4}{64}\frac{EI\delta^2}{L^3}. \tag{6.13}$$

Equating,

$$T = V \Rightarrow \omega = \frac{\pi^2\sqrt{\pi}}{4\sqrt{3\pi - 8}L^2}\sqrt{\frac{EI}{\mu_l}} = \frac{3.664}{L^2}\sqrt{\frac{EI}{\mu_l}}. \tag{6.14}$$

Note however, that adding the photoplastic part at the end of the fiber alters the mechanical properties of the probe. Moreover, the gluing operation can leave some residue along the fiber in the form of small droplets, Figure 6.14(a).

Influence of the ring guiding structure and the residual droplets on the probe mechanical properties can be monitored by a comparison of the different resonant frequencies. The resonant frequency ω_0 of a fiber without SU-8 ring guiding structure at its end is given by Equation 6.14. Ring guiding structure and SU-8 droplets can be approximated by n discrete masses m_i along the fiber. The kinetic energy is then given by

$$T = \frac{1}{2}\omega^2\mu_l\int_0^L y^2(x)\mathrm{d}x + \frac{1}{2}\omega^2\sum_{i=1}^{n} m_i y^2(x_i) \tag{6.15}$$

The potential energy is equal to the fiber without a probe at the end if the size of the droplets or of the ring guiding structure is assumed to be zero, that is the moment of inertia of the fiber is constant.

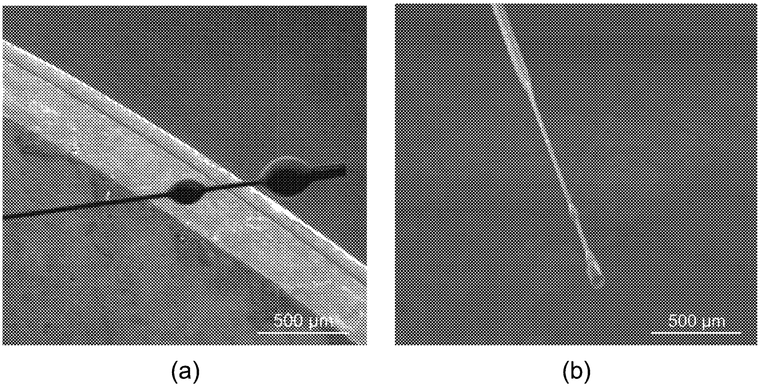

Figure 6.14: *SEMs images of photoplastic parts glued to optical fibers of reduced diameter. (a) Residual droplets along the fiber consequence of poor gluing quality. (b) Optimal gluing, very small residual droplets are visible.*

6.6.2 Fiber without Probe

The fiber without ring guiding structure glued at its end is considered as a cantilever with a constant circular cross-section of radius R and moment of inertia $I = \pi R^4/2$. For a fiber with a length to the ferrule L of 4 mm and a radius R of 20 μm, we find

$$\omega_0 = \frac{3.664}{L^2}\sqrt{\frac{EI}{\mu_l}} = 18.7\ kHz \tag{6.16}$$

with the Young's modulus $E = 80\ GPa$ and the linear density of the fiber material[1] $\mu_l = 3 \times 10^{-6}\ kg/m$.

6.6.3 Fiber with Probe

The photoplastic ring guiding structure is approximated by a discrete mass m_p located at a distance $x = L$ on the fiber.

---

[1] $\rho_{fiber} = 2400$ kg/m^3.

The kinetic energy is then given by

$$T = \frac{1}{2}\omega^2 \mu_l \int_0^L y^2(x)\mathrm{d}x + \frac{1}{2}\omega^2 m_p\, \delta^2. \tag{6.17}$$

Equation 6.17 and Equation 6.10 give an angular frequency of the fiber with the ring guiding structure ω_p of

$$\omega_p = \frac{2\pi^2}{8L}\sqrt{\frac{\pi EI}{L((3\pi - 8)\mu_l L + 2\pi m_p)}}. \tag{6.18}$$

A typical ring guiding structure of mass $m_p = 1.2 \times 10^{-12}\ kg$ changes the resonant frequency to $\omega_p = 15.6\ kHz$, or about 15%.

6.6.4 Fiber with Probe and residual Droplets

The gluing operation has to be done carefully. The high viscosity of the SU-8 used can produce residual droplets along the fiber. These droplets alter the resonant frequency of the probe. As an example, the resonant frequency of a fiber with a ring guiding structure of mass $m_p = 1.2 \times 10^{-12}\ kg$ at $x = L$ and two residual droplets of $3 \times 10^{-12}\ kg$ and $0.6 \times 10^{-12}\ kg$ at $x = 0.9 \times L$ and $0.6 \times L$ respectively is calculated to be $\omega_{p2} = 12.4\ kHz$, or about a 35% effect.

Hence, in order to obtain the predictable probe mechanical characteristics, the gluing operation has to be done carefully, so that no residual droplets remains on the fiber.

6.6.5 Approximation Error

In Appendix A, the resonance of a cantilever beam was found to be

$$\omega_0 = \frac{3.516}{L^2}\sqrt{\frac{EI}{\rho S}} = \frac{3.516}{L^2}\sqrt{\frac{EI}{\mu_l}} \tag{6.19}$$

The relative error due to the Rayleigh method used to calculate the effect of the SU-8 ring guiding structure on the probe mechanical characteristics is small at

$$\varepsilon = \frac{\omega - \omega_0}{\omega_0} = \frac{3.664 - 3.516}{3.516} \simeq 4.2\%, \tag{6.20}$$

so this method is appropriate for numerical approximations.

6.7 Probe Optical Characterization

6.7.1 Introduction

The optical quality of the probe is one of the determining factors in SNOM resolution. Manufacturing imperfections that can lead to image artifacts need to be easily recognized. A method for probe characterization is described in Ref. [115]. Transmission ratio and angular light intensity distribution of the SNOM probe can be made using the far-field set-up shown in Figure 6.17, whereas aperture size and tip apex geometry can be evaluated by mounting the probe to an actual SNOM. The pyramidal geometry of the photoplastic tips introduces unknowns that need to be analyzed. A far–field characterization of probes with pyramidal tips allows a determination of the long–range effects of tip shape.

6.7.2 Far-field Model

An image of the tip in the far–field can be made using Fourier analysis [95] if some simplifications are made. The simplified model used for the calculations is depicted in Figure 6.15. Light entering the tip is assumed to be a collimated beam with uniform distribution, and the tip is approximated by a thin element of maximal height h. Light passing through the tip is phase shifted, but the absolute value of its amplitude remains unchanged.

In reality, the light entering the tip is a Gaussian beam, and the assumption of a collimated beam with uniform distribution is not correct. However, the Gaussian beam can be approximated by masking the uniform beam before it enters the tip, so that Fourier analysis can still be used. This

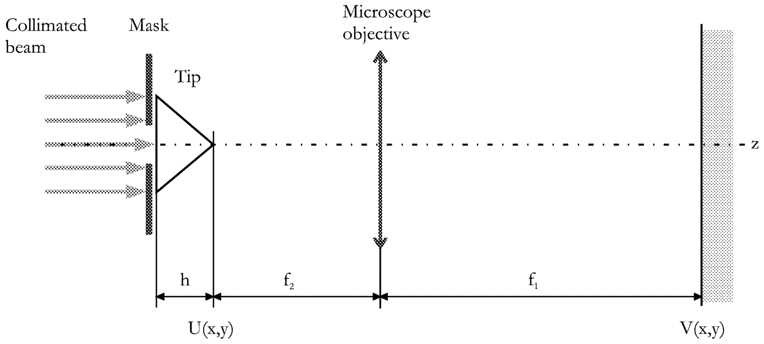

Figure 6.15: *Simplified model used for far–field calculations.*

is done by using a circular aperture mask with a diameter corresponding to the width of the Gaussian beam at half its maximum intensity.

The difference in optical path imposed by the tip produces a phase distribution within the beam which reaches the $x - y$ plane. This optical path difference is equal to the elevation of the pyramidal tip $\Delta(x, y)$ at coordinates (x, y). The total phase delay suffered by the wave at coordinates (x, y) when passing through the tip may be written as

$$\Phi(x,y) = kn\Delta(x,y) + kn_{air}\left[h - \Delta(x,y)\right] \tag{6.21}$$

where $k = 2\pi/\lambda$ the is the modulus of wave vector $\mathbf{k}$, n is the index of refraction of the tip material, $kn\Delta(x, y)$ is the phase delay introduced by the tip, and $kn_{air}\left[h - \Delta(x, y)\right]$ is the phase delay introduced by the remaining region of free space between the two planes. Equivalently, the tip may be represented by a multiplicative phase transformation of the form

$$t_{tip}(x,y) = \exp\left[jkh\right]\exp\left[jk(n - n_{air})\Delta(x,y)\right]. \tag{6.22}$$

The amplitude of the transmitted beam can thus be written as

$$U(x,y) = U_0 \exp\left[j\Phi(x,y)\right]. \tag{6.23}$$

where U_0 is the unperturbed amplitude.

The image at the back focal plane of the objective $V(x,y)$ is proportional to the two–dimensional Fourier transform $\mathcal{F}$ of the amplitude distribution at the front focal plane $U(x,y)$ evaluated at the spatial frequencies $x/\lambda f_1$ and $y/\lambda f_1$

$$V(x,y) \propto \mathcal{F}\left[U\left(\frac{x}{\lambda f_1},\frac{y}{\lambda f_1}\right)\right]. \tag{6.24}$$

This scalar approximation is valid only for a field evaluated at distances longer than λ.

The intensity

$$I(x,y) = |V(x,y)|^2 \tag{6.25}$$

has been numerically calculated for a tip having a base length of 12 μm. The intensity distribution is shown in Figure 6.16. The pyramidal shape tip produces intensity peaks located at the four corners of the tip. The intensity distribution is almost unchanged for tips with a larger base, as light is concentrated within an area much smaller that the tip base.

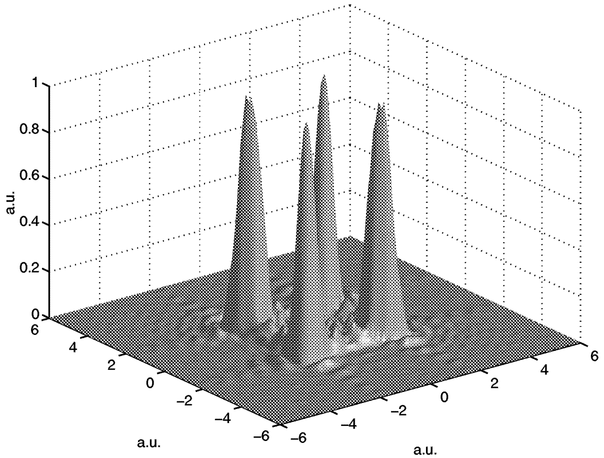

Figure 6.16: *Calculated intensity distribution of a collimated beam after passing through the tip and a microscope objective. The distribution is represented at the back focal plane of the objective.*

6.7.3 Far–field Experimental Characterization

A simplified setup used for far–field characterization is shown in Figure 6.17. A HeNe laser source ($\lambda = 633$ nm) is coupled into an optical fiber, and the beam is split up with a 50/50 coupler. One half, which serves as reference, is guided to detector 1. The other half is guided to the SNOM tip to be characterized. The tip is placed at the focal point of microscope objective 2 by means of a micropositioner. The beam is then analyzed by detector 2, which can be a photodiode when the transmission ratio of the probe is to be determined. An image of the intensity distribution is obtained by replacing the photodiode by a CCD–camera. A polarizer positioned between the objective and detector 2 can be used to measured the polarization of the light emitted by the probe.

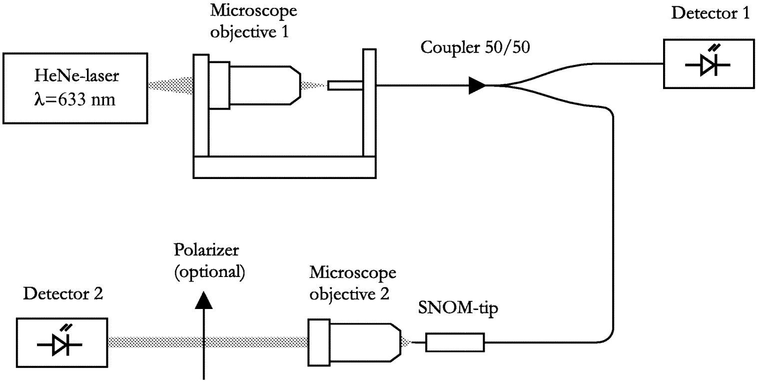

Figure 6.17: *Experimental setup for far–field characterization of SNOM probes.*

The transmission ratio of photoplastic probes without metallic coating has been measured to be 1.2 to 1.5×10^{-3}. The transmission ratio of coated tips has been found to be around 1.8×10^{-4} (the transmission ratio for conventional etched SNOM probes is in the range of 1.8×10^{-3}). Images of the intensity distribution for photoplastic probes with pyramidal tips is depicted in Figure 6.18. For non–coated tips, four preferential directions can be seen. They corresponds to the four edges of the pyramid and are in good correspondence with the simulation. For coated tips, the intensity is concentrated within a much smaller area. However, the aperture imaged is not ideally circular and does not produce a single spot.

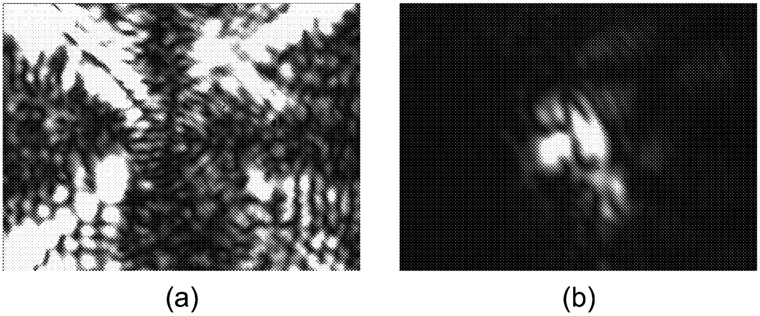

Figure 6.18: *Far–field images of photoplastic probes with pyramidal tips. (a) Image of a non–coated probe. (b) Image of a coated probe.*

6.8 SNOM Experiments

Photoplastic hybrid probes have been tested with SNOM using a shear-force technique for distance regulation [116]. In this technique, the probe laterally oscillates close to its resonant frequency. At a distance to the sample of some tens of nanometers, the interaction force between probe and sample reduces the oscillation amplitude. Shear-force detection has been made by using an external cavity laser interferometer [117]. The lateral resonant frequencies of the photoplastic–based probes are in the order of 5 kHz, and the Q-factors are around 50. Imaging of a chromium-on-glass test grating with a periodicity of 3 μm (2-μm line, 1-μm space, 80-nm step) has been performed. Figure 6.19 displays a near-field optical image of the transmission through the grating, recorded in illumination mode, with a laser source at 593 nm coupled into the optical fiber. The upper part of Figure 6.19 shows the topography of the grating, measured on a 8 μm × 1 μm area, while the lower image displays the simultaneously recorded corresponding transmitted intensity. The full width at half maximum of both topographical and optical signals yields the correct value of the grating pitch of 1 μm.

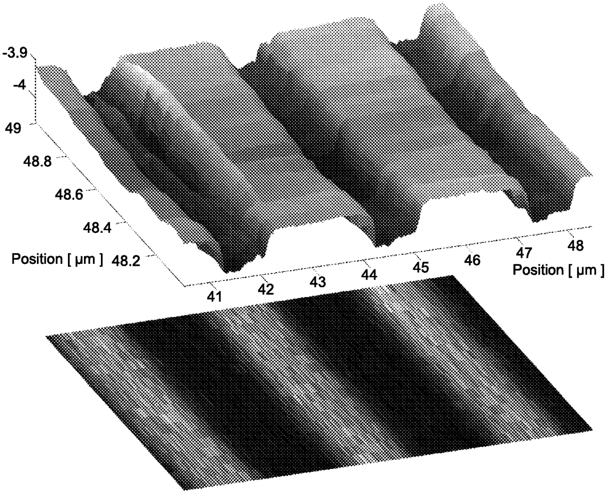

Figure 6.19: *Topography and optical transmission image of a 3-μm periodic test grating (2-μm Cr line, 1-μm glass, 80-nm step) demonstrating the potential of the photoplastic probe for SNOM imaging.*

These results were obtained with a probe with a 300-nm aperture size (as determined by a SEM measurement). It has yet not been possible to measure samples with smaller apertures. Coupling losses between the fiber and the tip, and back reflection of light inside the tip are the main problems. Back reflection is associated with coating quality of the tip. A metallic coating is first deposited onto the silicon mold, and then it is transferred to the tip upon releasing. The external coating surface quality is given by the quality of the (111)–planes of the pyramidal holes, which should be very smooth. But, depending on the metallic thickness needed for small apertures, coating surface quality of the internal side can be rough. Metal deposition must be performed so that a smooth surface is produced inside the inverted pyramids. This will reduce unwanted back reflection due to the grainy structure of the coating. Figure 6.20 shows a thick aluminum layer deposited on a pyramidal hole tip mold. Large grains produce back reflection of the light inside the tip.

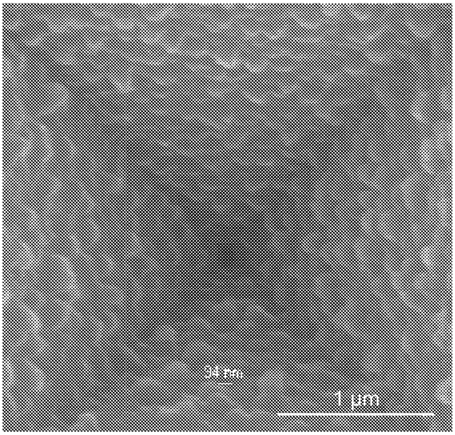

Figure 6.20: *SEM of a coated inverted pyramidal hole. Thick aluminum layer produces a grainy structure on the sides of the pyramid. The grains are responsible for back reflection of light inside the tip. Aperture size is smaller than 100 nm.*

6.9 Conclusions and further Development

In this chapter, a batch-fabrication technique for well-defined flat apertures for SNOM probes that requires no post-processing steps has been presented. Apertures are formed directly by probe fabrication, which avoids angle evaporation of aluminum and leads to much smoother external tip surface. Imaging of a test grating demonstrated the potential of imaging with such photoplastic-fiber hybrid probes. Investigations using probes with smaller apertures still needs to be done. Issues such as the influence of the aperture geometry on the image information have not been addressed in this thesis.

Chapter 7

Other Photoplastic–based Microstructures

7.1 Introduction

Photoplastic microstructure fabrication is not restricted to probes for SPMs. Combined with enhanced sacrificial layer etching and other micromachining techniques, photoplastic–based devices can be fabricated for a large variety of applications. These technologies open up the field to the fabrication of diversely sized plastic microstructures with complex shapes and nanometer features. This chapter gives a brief overview of some other microstructures fabricated using photoplastic techniques which are still under investigation at the IBM Zurich Research Laboratory. It describes probes with additional functionalities and other micromechanical structures.

7.2 SNOM Array

Photoplastic technology is envisioned to be used to fabricate entire arrays of SNOM probes. Such arrays offer interesting new perspectives for future SNOM applications: parallelism opens the way to faster imaging over larger distances, thereby overcoming some drawbacks of single probe imaging.

Figure 7.1 shows a first example of a fabricated 2 × 2 array of photoplastic SNOM probes which are meant to be attached to optical fibers. This fiber approach to the parallel operation of SNOM probes may not be the simplest to apply, but such a device demonstrates the design flexibility given by SU-8 structuring.

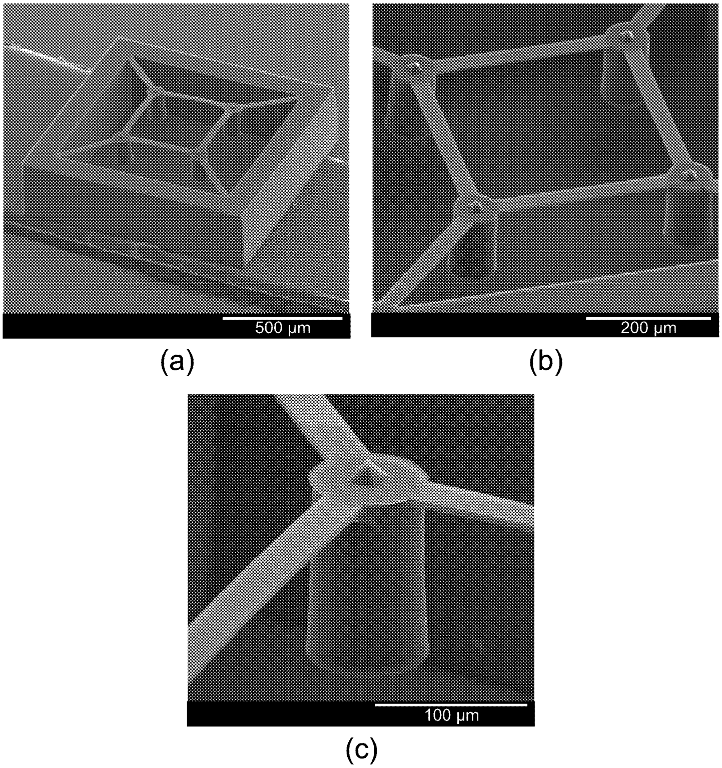

Figure 7.1: *SEM images of photoplastic SNOM probes in a 2 × 2 arrangement, showing potential for SNOM arrays. (a) Overall view of the chip, which is 1 × 1 mm^2 in size. (b) Closeup of the four coupled probes. The distance between two tips is 370 µm. (c) Closeup of a single probe.*

7.3 Mirror Lever

Photoplastic AFM probes are used with laser beam detection techniques. A more compact integrated sensing scheme could be provided by an adaptation of the fiber–optic interferometer displacement sensor presented in Ref. [129]. A vertical mirror located at the base of the cantilever forms an interferometric cavity with the end of the optical fiber. A cantilever displacement produces a displacement of the mirror, thereby measurably changing the optical path length in the interferometric cavity. Figure 7.2 shows the concept of the horizontal interferometric sensor for photoplastic AFM probes using a vertical mirror. The entire chip is made of SU-8, and the fabrication process is very similar to that of simple photoplastic AFM probes. A coating of the mirror may be necessary in order to obtain a sufficient reflection of the light beam.

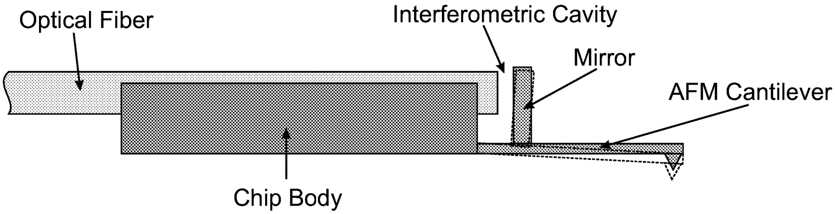

Figure 7.2: *Concept of the horizontal interferometric measurement system using a vertical mirror on the cantilever. An optical fiber is positioned horizontally on the chip body. An interferometric cavity is defined by the fiber end facet and the vertical mirror located at the base of the cantilever. The chip body, cantilever, tip and mirror are all made of SU-8 photoresist.*

Figure 7.3 shows a first fabricated and assembled prototype of such an AFM probe with the fiber end glued to the chip body. Fiber positioning is achieved by using prestructured grooves in the chip body.

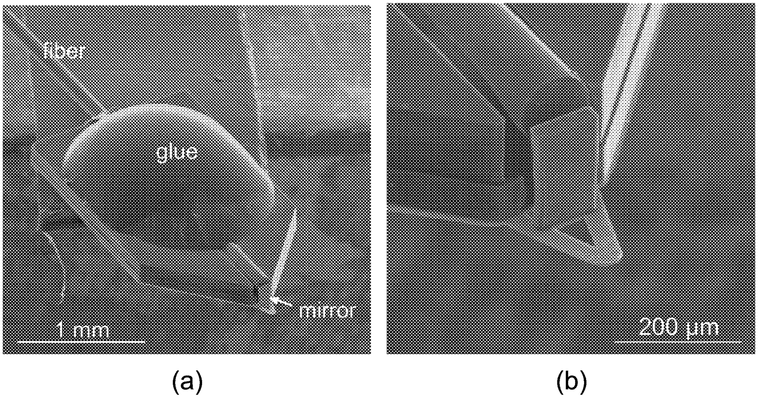

Figure 7.3: *SEMs of a prototype photoplastic AFM probe for interferometric sensing. (a) An optical fiber is mounted horizontally and glued onto the chip. The chip body, the cantilever and the mirror are made of SU-8. (b) Closeup of the cantilever. The fiber end and the mirror forming the interferometric cavity are visible.*

7.4 Tips Array

Another example of photoplastic microstructure fabrication combined with an efficient releasing technique is shown in Fig. 7.4. A large array of photoplastic tips has been fabricated and completely released from a silicon mold. The total width of the structure is 1.4 mm. Pyramids are 12 μm at their base. The array is fabricated using the same simple molding technique used for SFM tips, extended to millimeter–large chip dimensions. Such arrays could serve as diffraction gratings, or as calibration samples for scanning probe microscopy.

7.5 Microscanner

The mobile part of an electromagnetic microscanner for scanning probe microscopy can be fabricated by embedding copper coils in an SU-8 photoplastic

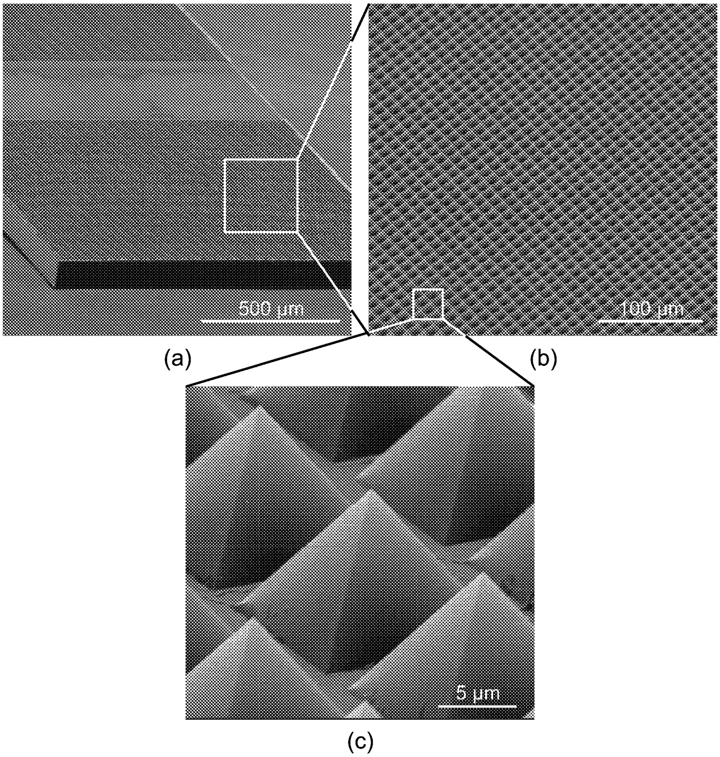

Figure 7.4: *SEMs of a fabricated and released array of photoplastic tips. (a) General view of the chip, which is 1.4 × 3 mm^2 in size. (b) and (c) Closeups of the tip array. The pyramidal tips are 8.5 μm high and 12 μm wide at their base.*

platform [130]. This electro–mechanical component demonstrates the ability to combine photoplastic structuring with electroplating and sacrificial release. In this case, the capability to release a cm–large device is crucial in order to avoid complete dissolution of the carrier wafer. Figure 7.5 shows fabricated copper coils embedded in SU-8 photoplastic, while Figure 7.6 shows the photoplastic mold before copper electroplating. The high aspect ratio and the vertical sidewalls achievable with this photoresist are clearly demonstrated.

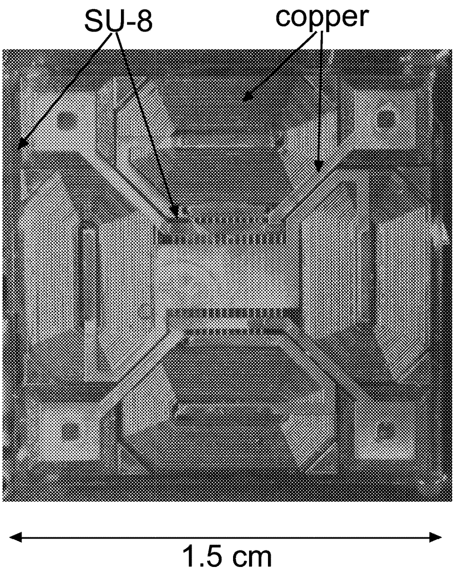

Figure 7.5: *Optical micrograph of multi–layered copper coils embedded in SU-8 photoplastic. This structure constitutes the mobile part of an electromagnetic microscanner for SPM.*

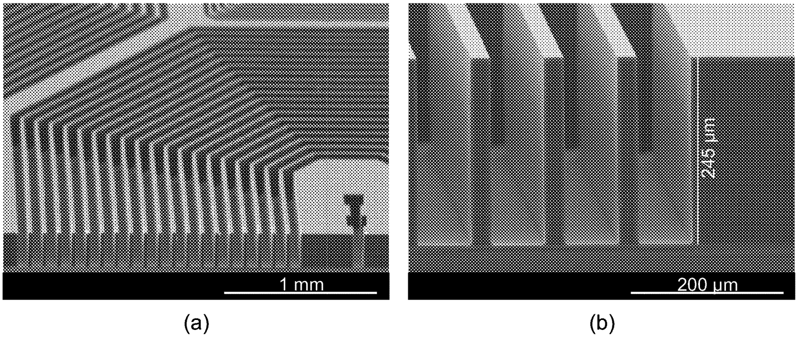

(a) (b)

Figure 7.6: *SU-8 mold for copper electroplating. The SU-8 is 245 μm thick and the lines are 25 μm wide.*

7.6 Artificial Cochlea

SU-8 mechanical properties are interesting for low stiffness microstructures. A "basilar membrane" meant to be used in an artificial cochlea (an organ of the inner ear) has been fabricated using SU-8 technology combined with an enhanced sacrificial layer release [131]. This structure is composed of several photoplastic layers with different thicknesses. The SU-8 cochlea is made out of a very thin (∼500–nm thick) spiral membrane across which are structured ∼2–μm thick cantilevers. These elements are supported by a ∼ 200–μm thick rigid frame. Figure 7.7 shows a life–sized microfabricated SU-8 cochlea.

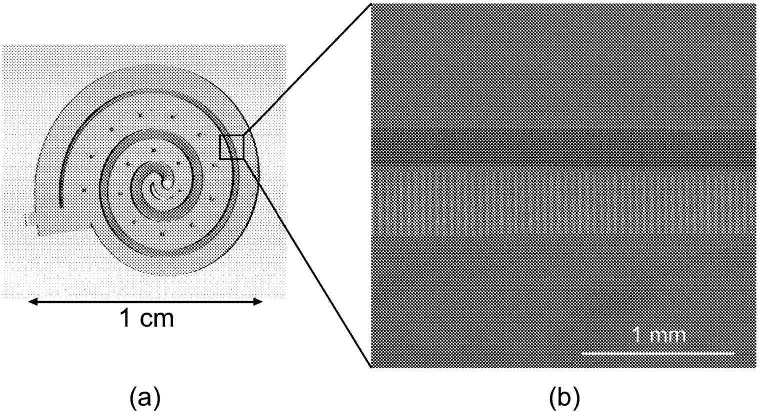

Figure 7.7: *(a) Optical micrograph of an SU-8 cochlea on the substrate. (b) SEM image of the cochlea membrane with the levers (released structure).*

7.7 Outlook

Photoplastic microstructuring is a versatile technique which allows the simple creation of complicated, three–dimensional, micromechanical devices. However, all the components mentioned in this thesis (with the exception of the microscanner) are passive. The integration of sensing and actuating functionality into the photoplastic structures could open a new dimension in micromechanical systems design. By use of sacrificial layer techniques, simple sensing and actuating elements fabricated separately on a wafer scale could be transferred and embedded to the photoplastic part of a device by release. Modified photoplastic materials could also provide a solution for completely functionalized, all–plastic, micromechanical devices. Most importantly, the simple batch processing of photoplastic components is well-suited for mass–producing as well as for rapid prototyping. It can facilitate the development of new applications, for example in today's active domain of micro–fluidic networks. Finally, the simple release and transfer of complicated MEMS microstructures will be very attractive for the hybridization of CMOS and photoplastic devices.

Chapter 8

Conclusions

In this thesis, I have presented different photoplastic fabrication techniques and devices based on high aspect ratio photoresist micromachining, molding, and releasing. The use of photoplastic material creates the possibility of microfabrication of low-cost devices with interesting mechanical properties. The major part of this thesis was concentrated on the fabrication of probes for scanning probe microscopy.

Low-cost probes for AFM have been fabricated using a simple fabrication method. The molding replication technique combined with photolithographic steps allowed the fabrication of cantilevers with integrated tips. Cantilever thickness can be easily tailored by modifying the spin–coating parameters. Sharp pyramidal tips have been obtained by oxidation sharpening of the silicon mold.

The freedom of design given by photoplastic microstructure fabrication has been illustrated with the fabrication of multiple cantilevers in a cassette arrangement. Such a complicated device would have been very difficult to obtain using standard silicon technologies. The cassette also demonstrates the well-controlled processing of SU-8 material through the uniformity of the cantilevers. The cassette of probes could be an important component in a completely automated AFM instrument.

The quality of the AFM probes has been demonstrated by imaging biological samples. The softness of photoplastic tips bring advantages for fragile samples, and tip overcoating would allow more customized applications.

The possibility of combining SU-8 technique with standard micromachining technology has been demonstrated with the fabrication of photoplastic–based hybrid SNOM probes. Probes with integrated apertures have been developed using a combination of etching, thin film deposition and molding techniques. This device also clearly showed the necessity for an efficient releasing method. A sacrificial layer technique based on electrochemical enhancement has been developed. This technique permits the demolding and releasing of large microstructures fabricated on a substrate. Finally, it has been shown that SU-8 devices are not restricted to probes for SPMs. Three–dimensional micromechanical elements with complicated shapes can be fabricated on a wafer scale.

Hence, SU-8 material is very suitable for the fabrication of micromechanical devices. Further research work is required to explore the possibilities to integrate sensing and actuating functionality into photoplastic structures. This will open up the potential for even greater capabilities of photoplastic–based microsystems technology.

Appendix A

Analytical Resonant Frequency Calculation

The equation of motion for a prismatic beam, with a Young's modulus E and a moment of inertia I constant, subject to a tansverse load $p(x,t)$, is given by

$$EI\frac{\partial^4 y(x,t)}{\partial x^4} = p(x,t) \tag{8.1}$$

with $y(x,t)$ the deflection of the beam at position x and time t along the beam.

To derive the equation of motion for the transverse vibration of a bar, the *D'Alembert Principle* is applied to Equation 8.1. An "inertia force" is added to the external force $p(x,t)$. The "inertia force" per unit length of the bar is given by

$$-\rho S(x)\frac{\partial^2 y(x,t)}{\partial t^2} \tag{8.2}$$

where ρ is the density of the material of the beam and $S(x)$ is its cross sectional area. The equation of motion is then

$$EI\frac{\partial^4 y(x,t)}{\partial x^4} = p(x,t) - \rho S(x)\frac{\partial^2 y(x,t)}{\partial t^2}. \tag{8.3}$$

For the case of free vibrations, $p(x,t) = 0$, and Equation 8.3 becomes

$$EI\frac{\partial^4 y(x,t)}{\partial x^4} = -\rho S(x)\frac{\partial^2 y(x,t)}{\partial t^2}. \tag{8.4}$$

To solve Equation 8.4 the method of separation of variables is employed, where we assume that

$$y(x,t) = X(x)f(t). \tag{8.5}$$

Substituting Equation 8.5 into Equation 8.4 and separating variables, we obtain the equation

$$\frac{EI}{\rho S(x)X(x)}\frac{\mathrm{d}^4 X(x)}{\mathrm{d}x^4} = -\frac{1}{f(t)}\frac{\mathrm{d}^2 f(t)}{\mathrm{d}t^2} = \omega^2 \tag{8.6}$$

where ω^2 is a constant of the motion.

From Equation 8.6, the two ordinary differential equation for $X(x)$ and $f(t)$ follow

$$\begin{aligned} EI\frac{\mathrm{d}^4 X(x)}{\mathrm{d}x^4} - \omega^2 \rho S(x)X(x) &= 0, & (8.7)\\ \frac{\mathrm{d}^2 f(t)}{\mathrm{d}t^2} + \omega^2 f(t) &= 0. & (8.8) \end{aligned}$$

The general solution of Equation 8.8 is

$$f(t) = A\cos(\omega t) + B\sin(\omega t). \tag{8.9}$$

If the bar has constant cross section, then S(x) and I(x) are constants, and Equation 8.7 becomes

$$\frac{\mathrm{d}^4 X}{\mathrm{d}x^4} - \alpha^4 X = 0 \tag{8.10}$$

where

$$\alpha^2 = \sqrt{\frac{\omega^2 \rho S}{EI}}. \tag{8.11}$$

The general solution of Equation 8.10 is a linear combination of the functions $\sin kx$, $\cos kx$, $\sinh kx$ and $\cosh kx$. The solution can be expressed in the form

$$\begin{aligned} X(x) = {} & C_1[\cos(\alpha x) + \cosh(\alpha x)] + C_2[\cos(\alpha x) - \cosh(\alpha x)] \\ & + C_3[\sin(\alpha x) + \sinh(\alpha x)] + C_4[\sin(\alpha x) - \sinh(\alpha x)] \quad (8.12) \end{aligned}$$

where C_1, C_2, C_3 and C_4 are arbitrary constants depending on the boundary conditions.

In the case of a cantilever beam with one end clamped and the other free, we have specific boundary conditions. At the fixed end ($x = 0$) the displacement and the slope of the deflection curve must be zero, and at the free end ($x = L$) the bending moment and the shearing force must be zero:

$$\left.\begin{array}{ll} y(0,t) = 0; & \dfrac{\partial y}{\partial x}(0,t) = 0 \\ \dfrac{\partial^2 y}{\partial x^2}(L,t) = 0; & \dfrac{\partial^3 y}{\partial x^3}(L,t) = 0 \end{array}\right\} for\ t \geq 0. \tag{8.13}$$

These boundary conditions lead to the following frequency equation

$$\cos(\alpha L)\cosh(\alpha L) = -1. \tag{8.14}$$

To each frequency

$$\omega_n = \alpha_n^2 \sqrt{\frac{EI}{\rho S}} \tag{8.15}$$

corresponds the characteristic function

$$X_n(x) = \cosh(\alpha_n x) - \cos(\alpha_n x) - \frac{\cos(\alpha_n L) + \cosh(\alpha_n L)}{\sin(\alpha_n L) + \sinh(\alpha_n L)}[\sinh(\alpha_n x) - \sin(\alpha_n x)] \tag{8.16}$$

and the characteristic vibration

$$y_n(x,t) = X_n(x)[A_n \cos(\omega_n t) + B_n \sin(\alpha_n x)] \tag{8.17}$$

The general solution is the sum of the characteristic vibrations. The coefficients A_n and B_n depend on the initial conditions.

The first root $\alpha_1 L$ of the frequency equation is equal to 1.875 [132], so that

$$\omega_1 = \alpha_1^2 \sqrt{\frac{EI}{\rho S}} = \left(\frac{1.875}{L}\right)^2 \sqrt{\frac{EI}{\rho S}} = \frac{3.5156}{L^2}\sqrt{\frac{EI}{\rho S}}. \tag{8.18}$$

which is the first angular resonance frequency of the cantilever beam.

Appendix B

AFM Photoplastic Cantilevers Fabrication. Process Sequence.

Shown overleaf.

Step #	Operation	Parameters	Notes
10	starting wafer	4-in. ⟨100⟩ Si wafer	mold substrate
20	thermal wet oxidation	piranha clean thermal oxidation, @1000°C ~1 μm SiO_2	mask for KOH etching
30	litho *tip*	standard clean dehydratation @ 200°C > 30 min priming HMDS 3000 rpm 20 s spinning AZ 6612 4000 rpm 50 s prebake hotplate @110°C 50 s exposure LVC 33 mJ/cm^2 development AZ 400 K:H_2O/1:4 20 s postbake @90°C 20 min	
40	SiO_2 etching	RIE CHF_3/O_2 45 min	mask for tip etching
50	photoresist stripping	Ac+US 5 min, IPA + US 5 min, DI-H_2O 5 min	
60	tip-mold etching	KOH 40%, @60°C, 55 min	pyramidal holes
70	wafer cleaning	piranha clean 5 min	
80	SiO_2 stripping	BHF 7:1, 12 min 30 s	remove SiO_2 mask
90	wafer cleaning	piranha clean 5 min RCA2 clean 10 min BHF 7:1 1 min	
100	tip-mold sharpening	low-*T* thermal wet oxidation @950°C, 4 h 30 min, ~650 nm	
120	Al sputtering	Al "sacrificial" layer 5 min, 10 W, 6.8 μbar, ~20 nm	
140	litho *lever*	no dehydration spinning SU-8 10 6400 rpm 40 s PB hotplate @95°C 6 min exposure LVC 130 mJ/cm^2 PEB hotplate @95°C 15 min development PGMEA new 20 s IPA rinse	
150	lever thickness control	α-step	
160	lever hardening	HB oven 200°C 6 min	
170/1	no dehydratation	spinning 4 ml SU-8 50 500 rpm 10 s, 700 rpm 40 s leave on leveled surface PB hotplate @95°C 2h exposure SC 780 mJ/cm^2 PEB hotplate @95°C 15 min cool down slowly	litho block (part 1)
170/2	2nd body layer	spinning 4 ml SU-8 50 500 rpm 40 s leave on leveled surface PB hotplate @95°C 2 h 30 min exposure SC 1000 mJ/cm^2 PEB hotplate @95°C 15 min cool down slowly	litho block (part 2)
180	development block	PGMEA old 15 min with stirring PGMEA new 5 min IPA rinse	
190	Al etch	TMAH @65°C rinse DI, IPA dry hotplate @85°C	chip releasing
200	tweezer releasing		

Bibliography

[1] G. T. A. Kovacs, Micromachined Transducers Sourcebook, McGraw-Hill Companies, Inc., New York, NY, 1998.

[2] D. F. Moore and R. R. A. Syms, in *Electronics & Communication Engineering Journal*, December 1999.

[3] M. Madou, Fundamentals of Microfabrication, CRC Press, Inc., Boca Raton, FL, 1997.

[4] M. Lutwyche, C. Andreoli, G. Binnig, J. Brugger, U. Drechsler, W. Haeberle, H. Rohrer, H. Rothuizen, and P. Vettiger, in *Proceedings of the IEEE 11th International Workshop on Micro Electro Mechanical Systems (MEMS '98)*, Heidelberg, Germany, January 1998, 8.

[5] J. A. Walker, J. Micromech. Microeng. **10**, R1, (2000).

[6] A. Neukermans and R. Ramaswami, in *IEEE Communications Magazine* **39**, January 2001, 62.

[7] S. C. Minne, Ph. Flueckiger, H. T. Soh, and C. F. Quate, J. Vac. Sci. Technol. B **13**, 1380, (1995).

[8] S. C. Minne, S. R. Manalis, A. Atalar, and C. F. Quate, J. Vac. Sci. Technol. B **14**, 2456, (1996).

[9] R. Berger, E. Delamarche, H.-P. Lang, C. Gerber, J. K. Gimzewski, E. Meyer, and H.-J. Güntherodt, Science **276**, 2021, (1997).

[10] J. Fritz, M. K. Baller, H. P. Lang, H. Rothuizen, P. Vettiger, E. Meyer, H.-J. Güntherodt, Ch. Gerber, J. K. Gimzewski, Science **288**, 316, (2000).

[11] E. Delamarche, A. Bernard, H. Schmid, B. Michel, and H. Biebuyck, Science **276**, 779, (1997).

[12] A. Bernard, B. Michel, and E. Delamarche, Anal. Chem. **73**, 8, (2001).

[13] C. T.-C. Nguyen, in *Proceedings of the IEEE 11th International Workshop on Micro Electro Mechanical Systems (MEMS '98)*, Heidelberg, Germany, January 1998, 1.

[14] K. E. Petersen, in *Proceedings of the IEEE* **70**, 420, (1982).

[15] G. Kaminsky, J. Vac. Sci. Technol. B **3**, 1015, (1985).

[16] E. H. Klaassen, K. Petersen, J. M. Noworolski, J. Logan, N. I. Maluf, J. Brown, C. Storment, W. McCulley, and G. T. A. Kovacs, in *Proceedings of the IEEE 8th International Conference on Solid-State Sensors and Actuators (Transducers '95)*, Stockholm, Sweden, June 1995, 556.

[17] V. Lehmann and H. Föll, J. Electrochem. Soc. **137**, 653, (1990).

[18] R. T. Howe, J. Vac. Sci. Technol. B **6**, 1809, (1988).

[19] J.-Å. Schweitz, K. Larsson, G. Thornell, H. Björkman, and F. Nikolajeff, Mat. Res. Soc. Symp.Proc. **605**, 57, (2000).

[20] E. W. Becker, W. Ehrfeld, P. Hagmann, A. Manner, and D. Münchmeyer, Microelectronic Eng. **4**, 35, (1986).

[21] M. Despont, H. Lorenz, N. Fahrni, J. Brugger, P. Renaud, and P. Vettiger, in *Proceedings of the IEEE 10th International Workshop on Micro Electro Mechanical Systems (MEMS '97)*, Nagoya, Japan, January 1997, 518.

[22] N. LaBianca and J. D. Gelorme, in *Advances in Resist Technology and Processing XII (Ed. R. D. Allen), Proceedings SPIE* **2438**, Bellingham, WA, 846, (1994).

[23] K. Y. Lee, N. LaBianca, S. A. Rishton, S. Zolgharnain, J. D. Gelorme, J. Shaw, and T. H.-P. Chang, J. Vac. Sci. Technol. B **13**, 3012, (1995).

[24] U.S. Patent 4882245, 1989, and others.

[25] H. Lorenz, M. Despont, N. Fahrni, J. Brugger, P. Vettiger, and P. Renaud, Sensors and Actuators A **64**, 33, (1998).

[26] R. K. Vestergaard and S. Bouwstra, in *Proceedings of the IEEE International Conference on Solid-State Sensors and Actuators (Transducers '99)*, Sendai, Japan, June 1999, 480.

[27] L. Dellmann, S. Gautsch, G.-A. Racine, and N. F. de Rooij, in *Proceedings of the IEEE International Conference on Solid-State Sensors and Actuators (Transducers '99)*, Sendai, Japan, June 1999, 1752.

[28] L. J. Guérin, A. Torosdagi, P. Eichenberger, and Ph. Renaud, in *Proc. of Eurosensors XII, the 12th European Conference on Solid-State Transducers*, Southampton, UK, September 1998, 11.

[29] D. J. Strike, Ph. E. Michel, E. L'Hostis, G. C. Fiaccabrino, N. F. de Rooij, and M. Koudelka-Hep, in *Proceedings of the IEEE International Conference on Solid-State Sensors and Actuators (Transducers '99)*, Sendai, Japan, June 1999, 130.

[30] T. Hamano, V. M. Lubecke, and K. Mizuno, in *Proceedings of the IEEE International Conference on Solid-State Sensors and Actuators (Transducers '99)*, Sendai, Japan, June 1999, 484.

[31] A. Bertsch, H. Lorenz, and P. Renaud, in *Proceedings of the IEEE 11th International Workshop on Micro Electro Mechanical Systems (MEMS '98)*, Heidelberg, Germany, January 1998, 18.

[32] L. J. Guérin, M. Bossel, M. Demierre, S. Calmes, and Ph. Renaud, in *Proceedings of the IEEE International Conference on Solid-State Sensors and Actuators (Transducers '97)*, Chicago, June 1997, 1419.

[33] F. E. H. Tay, J. A. van Kan, F. Watt, and W. O. Choong, J. Micromech. Microeng. **11**, 27, (2001).

[34] A. L. Bogdanov and S. S. Peredkov, Microelectronic Eng. **53**, 493, (2000).

[35] H. Lorenz, M. Despont, N. Fahrni, N. LaBianca, P. Renaud, and P. Vettiger, J. Micromech. Microeng. **7**, 121, (1997).

[36] L. Dellmann, S. Roth, C. Beuret, G.-A. Racine, H. Lorenz, M. Despont, P. Renaud, P. Vettiger, and N. F. de Rooij, in *Proceedings of the IEEE International Conference on Solid-State Sensors and Actuators (Transducers '97)*, Chicago, June 1997, 641.

[37] H. Lorenz, M. Laudon, and P. Renaud, Microelectronic Eng. **41/42**, 371, (1998).

[38] M. Ghantasala, J. P. Hayes, E C. Harvey, and D. K. Sood, J. Micromech. Microeng. **11**, 133, (2001).

[39] E. Richter, S. Hien, and M. Sebald, Microelectronic Eng. **53**, 479, (2000).

[40] J. A. van Kan, A. A. Bettiol, B. S. Wee, T. C. Sum, T. Osipowicz, and F. Watt, in *Proc. of Eurosensors XIV, the 14th European Conference on Solid-State Transducers*, Copenhagen, Denmark, August 2000, 451.

[41] G. Binnig, H. Rohrer, Ch. Gerber, and E. Weibel, Phys. Rev. Lett. **49**, 57, (1982).

[42] See for example: H. K. Wickramasinghe, J. Vac. Sci. Technol. A **8**, 363, (1990).

[43] G. Binnig, C. F. Quate, and Ch. Gerber, Phys. Rev. Lett. **56**, 930, (1986).

[44] N. A. Burnham, R. J. Colton, and H. M. Pollock, Nanotechnology **4**, 64, (1993).

[45] Y. Martin and H. K. Wickramasinghe, Appl. Phys. Lett. **50**, 1455, (1987).

[46] C. M. Mate, G. M. McClelland, R. Erlandsson, and S. Chiang, Phys. Rev. Lett. **59**, 1942, (1987).

[47] Y. Martin, D. W. Abraham, and H. K. Wickramasinghe, Appl. Phys. Lett. **52**, 1103, (1988).

[48] C. C. Williams, W. P. Hough, and S. A. Rishton, Appl. Phys. Lett. **55**, 203, (1989).

[49] C. F. Quate, Surface Science **386**, 259, (1997).

[50] E. S. Snow and P. M. Campbell, Appl. Phys. Lett. **64**, 1932, (1994).

[51] D. Wang, L. Tsau, K. L. Wang, and P. Chow, Appl. Phys. Lett. **67**, 1295, (1995).

[52] A. Majumdar, P. I. Oden, J. P. Carrejo, L. A. Nagahara, J. J. Graham, and J. Alexander, Appl. Phys. Lett. **61**, 2293, (1992).

[53] H. J. Mamin and D. Rugar, Appl. Phys. Lett. **61**, 1003, (1992).

[54] H. Kado and T. Tohda, Appl. Phys. Lett. **66**, 2961, (1995).

[55] T. Hidaka, T. Maruyama, M. Saitoh, N. Mikoshiba, M. Shimizu, T. Shiosaki, L. A. Wills, R. Hiskes, S. A. Dicarolis, and J. Amano, Appl. Phys. Lett. **68**, 2358, (1996).

[56] P. Vettiger, M. Despont, U. Drechsler, U. Dürig, W. Häberle, M. I. Lutwyche, H. E. Rothuizen, R. Stutz, R. Widmer, and G. K. Binnig, IBM J. Res. Develop. **44**, 323, (2000).

[57] T. Akiyama, S. Gautsch, N. F. de Rooij, U. Staufer, Ph. Niedermann, L. Howald, D. Müller, A. Tonin, H.-R. Hidber, W. T. Pike, and M. H. Hecht, in *Proc. Solid-State Sensor and Actuator Workshop*, Hilton Head Island, SC, June 2000, 267.

[58] S. A. C. Gould, B. Drake, C. B. Prater, A. L. Weisenhorn, S. Manne, H. G. Hansma, P. K. Hansma, J. Massie, M. Longmire, V. Elings, B. Dixon Northern, B. Mukergee, C. M. Peterson, W. Stoeckenius, T. R. Albrecht, and C. F. Quate, J. Vac. Sci. Technol. A **8**, 369, (1990).

[59] P. Perfetti, A. Cricenti, and R. Generosi, Surf. Rev. Lett. **7**, 411, (2000).

[60] Y. Martin, C. C. Williams, and H. K. Wickramasinghe, J. Appl. Phys. **61**, 4723 (1987).

[61] D. Rugar, H. J. Mamin, R. Erlandson, J. E. Stern, and B. D. Terris, Rev. Sci. Instrum. **59**, 2337, (1988).

[62] N. M. Amer and G. Meyer, Bull. Am. Phys. Soc. **33**, 319 (1988); G. Meyer and N. M. Amer, Appl. Phys. Lett. **53**, 2400 (1988).

[63] T. Göddenhenrich, H. Lemke, U. Hartmann, and C. Heiden, J. Vac. Sci. Technol. A **8**, 383, (1990).

[64] G. Neubauer, S. R. Cohen, G. M. McClelland, D. Horne, and C. M. Mate, Rev. Sci. Instrum. **61**, 2296, (1990).

[65] N. Blanc, J Brugger, N. F. de Rooij, and U. Dürig, J. Vac. Sci. Technol. B **14**, 901, (1996).

[66] M. Anders and C. Heiden, J. Micros. **152**, 643, (1988).

[67] J. Tansock and C. C. Williams, Ultramicroscopy **42-44**, 1464, (1992).

[68] T. Itoh and T. Suga, Nanotechnology **4**, 218, (1993).

[69] T. Itoh and T. Suga, J. Vac. Sci. Technol. B **12**, 1581, (1994).

[70] M. Tortonese, H. Yamada, R. C. Barrett, and C. F. Quate, in *Proceedings of IEEE Transducers '91*, San Francisco, CA, June 1991, 448.

[71] M. Tortonese, R. C. Barrett, and C. F. Quate, Appl. Phys. Lett. **62**, 834, (1993).

[72] T. Akiyama, A. Tonin, H. R. Hidber, J. Brugger, P. Vettiger, U. Staufer, and N. F. de Rooij, in *Proceedings of the IEEE 10th International Workshop on Micro Electro Mechanical Systems (MEMS '97)*, Nagoya, Japan, January 1997, 146.

[73] S. C. Minne, S. R. Manalis, and C. F. Quate, Appl. Phys. Lett. **67**, 3918, (1995).

[74] G. Binnig, M. Despont, U. Drechsler, W. Häberle, M. Lutwyche, P. Vettiger, H. J. Mamin, B. W. Chui, and T. W. Kenny, Appl. Phys. Lett. **74**, 1329 ,(1999).

[75] H. J. Mamin, B. D. Terris, L. S. Fan, S. Hoen, R. C. Barrett, and D. Rugar, IBM J. Res. Dev. **39**, 681, (1995).

[76] T. R. Albrecht, P. Grütter, D. Horne, and D. Rugar, J. Appl. Phys. **69**, 668, (1991).

[77] O. Wolter, Th. Bayer, and J. Greschner, J. Vac. Sci. Technol. B **9**, 1353, (1991).

[78] T. R. Albrecht and C. F. Quate, J. Vac. Sci. Technol. A **6**, 271, (1988).

[79] T. R. Albrecht, S. Akamine, T. E. Carver, and C. F. Quate, J. Vac. Sci. Technol. A **8**, 3386, (1990).

[80] R. Pechmann, J. M. Köhler, W. Fritzsche, A. Schaper, and T. M. Jovin, Rev. Sci. Instrum. **65**, 3702, (1994).

[81] S. Timoshenko, Strength of Materials, Krieger Publishing Company, Malabar, FL, 1983.

[82] G. Y. Chen, R. J. Warmack, T. Thundat, D. P. Allison, and A. Huang, Rev. Sci. Instrum. **65**, 2532, (1994).

[83] See for example: http://www.nanosensors.com/products.htm, or http://www.olympus.co.jp/LineUp/Technical/Cantilever/levertopE.html

[84] A. Boisen, O. Hansen, and S. Bouwstra, J. Micromech. Microeng. **6**, 58, (1996).

[85] A. Boisen, J. P. Rasmussen, O. Hansen, and S. Bouwstra, Microelectronic Eng. **30**, 579, (1996).

[86] S. Akamine and C. F. Quate, J. Vac. Sci. Technol. B **10**, 2307, (1992).

[87] R. B. Marcus and T. T. Sheng, J. Electrochem. Soc. **129**, 1278, (1982).

[88] B. E. Deal, J. Electrochem. Soc. **125**, 576, (1978).

[89] Int'l Patent Application WO 99/56176, Low-cost photoplastic cantilever.

[90] The profilometer used is an *Alpha-Step*® from Tencor Instruments.

[91] personal communication, Marc Neuhaeuser, IBM SSD Mainz, Germany.

[92] Y. Onuma, Z. Wang, H. Ito, M. Nakao, and K. Kamimura, Jpn. J. Appl. Phys. **37**, 963, (1998).

[93] A. B. Frazier and M. G. Allen, J. Appl. Phys. **73**, 4428, (1993).

[94] E. Abbe, Archiv. Mikroskop. Anat. **9**, 413, (1873).

[95] J. W. Goodman, Introduction to Fourier Optics, McGraw-Hill, San Francisco, 1968.

[96] G. A. Massey, Appl. Optics **23**, 658, (1984).

[97] D. W. Pohl, W. Denk, and M. Lanz, Appl. Phys. Lett. **44**, 651, (1984).

[98] H. Heinzelmann and D. W. Pohl, Appl. Phys. A **59**, 89, (1994).

[99] E. Betzig and J. K. Trautman, Science **257**, 189, (1992).

[100] G. A. Valaskovic, M. Holton, and G. H. Morrison, Appl. Optics **34**, 1215, (1995).

[101] P. Lambelet, A. Sayah, M. Pfeffer, C. Philipona, and F. Marquis-Weible, Appl. Optics **37**, 7289, (1998).

[102] W. Noell, M. Abraham, K. Mayr, A. Ruf, J. Barenz, O. Hollricher, O. Marti, and P. Güthner, Appl. Phys. Lett. **70**, 1236, (1997).

[103] G. Schürmann, W. Noell, U. Staufer, and N. F. de Rooij, Ultramicroscopy **82**, 33, (2000).

[104] A. G. T. Ruiter, M. H. P. Moers, N. F. van Hulst, and M. de Boer, J. Vac. Sci. Technol. B **14**, 597, (1996).

[105] P. N. Minh, T. Ono, and M. Esashi, Appl. Phys. Lett. **75**, 4076, (1999).

[106] R. Eckert, J. M. Freyland, H. Gersen, H. Heinzelmann, G. Schürmann, W. Noell, U. Staufer, and N. F. de Rooij, Appl. Phys. Lett. **77**, 1, (2000).

[107] C. Mihalcea, W. Scholz, S. Werner, S. Münster, E. Oesterschulze, and R. Kassing, Appl. Phys. Lett. **68**, 3531, (1996).

[108] Int'l Patent Application WO 00/03302, Low-cost, simple mass production of light-guiding tips.

[109] H. Lorenz, Ph. D. dissertation N^o 1770, Département de Microtechnique, Ecole Polytechnique Fédérale de Lausanne, (1998).

[110] D. Drews, W. Ehrfeld, K. Mayr, W. Noell, S. Schmitt, and M. Abraham, Nanotechnology **10**, 61, (1999).

[111] D. Mulin, D. Courjon, J.-P. Malugani, and B. Gauthier-Manuel, Appl. Phys. Lett. **71**, 437, (1997).

[112] M. Muranishi, K. Sato, S. Hosaka, A. Kikukawa, T. Shintani, and K. Ito, Jpn. J. Appl. Phys. **36**, L942, (1997).

[113] S. Pilevar, K. Edinger, W. Atia, I. Smolyaninov, and C. Davis, Appl. Phys. Lett. **72**, 3133, (1998).

[114] J. A. Veerman, A. M. Otter, L. Kuipers, and N. F. van Hulst, Appl. Phys. Lett. **72**, 3115, (1998).

[115] M. Pfeffer, Ph. D. dissertation N^o 1842, Département de Microtechnique, Ecole Polytechnique Fédérale de Lausanne, (1998).

[116] E. Betzig, P. L. Finn, and J. S. Weiner, Appl. Phys. Lett. **60**, 2484, (1992).

[117] M. Pfeffer, P. Lambelet, and F. Marquis-Weible, Rev. Sci. Instrum. **68**, 4478, (1997).

[118] J. Bühler, F.-P. Steiner, and H. Baltes, J. Micromech. Microeng. **7**, R1, (1997).

[119] C. Burbaum, J. Mohr, P. Bley, and W. Ehrfeld, Sensors and Actuators A **25-27**, 559, (1991).

[120] A. Maciossek, B. Löchel, H.-J. Quenzer, B. Wagner, S. Schulze, and J. Noetzel, Microelectronic Eng. **27**, 503, (1995).

[121] A. B. Frazier, C. H. Ahn, and M. G. Allen, Sensors and Actuators A, **45**, 47, (1994).

[122] Z. Cui and R. A. Lawes, J. Micromech. Microeng. **7**, 128, (1997).

[123] M. Bartek and R. F. Wolffenbuttel, J. Micromech. Microeng. **8**, 91, (1998).

[124] H.-J. Suh, P. Bharathi, D. J. Beebe, and J. S. Moore, J. Microelectromechanical Syst. **9**, 198, (2000).

[125] P. Steiner, A. Richter, and W. Lang, J. Micromech. Microeng. **3**, 32, (1993).

[126] G.-A. Racine, G. Genolet, P.-A. Clerc, M. Despont, P. Vettiger, and N. F. de Rooij, in *Proc. of Eurosensors XI, the 11th European Conference on Solid-State Transducers*, Warsaw, Poland, September 1997, 285.

[127] B. J. Kim, G. M. Kim, M. Liebau, J. Huskens, D. N. Reinhoudt, and J. Brugger, in *Proceedings of the IEEE 14th International Workshop on Micro Electro Mechanical Systems (MEMS '01)*, Interlaken, Switzerland, January 2001, 106.

[128] European patent application 01810141.0 with title "Enhanced Sacrificial Layer Etching Technique for Microstructure Release" (2001).

[129] D. Rugar, H. J. Mamin, and P. Guethner, Appl. Phys. Lett. **55**, 2588, (1989).

[130] H. Rothuizen *et al.* in preparation.

[131] W. Hemmert *et al.*, in preparation.

[132] W. C. Young, Roark's Formulas for Stress and Strain, McGraw-Hill Companies, Inc., 1989.

Acknowledgments

First of all I would like to thank my advisor Prof. Nico de Rooij for giving me the opportunity to do research in the exciting field of microtechnology. My stay at IBM would not have been possible without his continuous and enthusiastic support. My warmest thanks go to Peter Vettiger, my manager at IBM, who gave me the opportunity to work for this thesis in the Micro/-Nanomechanics group at the IBM Zurich Research Laboratory. Working with him was a great experience. We had a lot of interactions and many interesting discussions concerning work, sports or everyday life. His advice and tendency to always look further had me working really hard sometimes, but we certainly had a good time. Thanks also to Paul Seidler at IBM for his continuous support during my stay.

I am particularly indebted to Michel Despont, who constantly followed my work and was always present for help or advice. His friendship is anchored well beyond the context of this work. My deepest thanks go to all the other members of the Micro/-Nanomechanics group: to Gerd Binnig, Graham Cross, Ute Drechsler, Urs Dürig, Walter Häberle, Hugo Rothuizen, Richard Stutz, and Roland Widmer; the former members of the group, Jürgen Brugger, Werner Hemmert, Bill King, and Mark Lutwyche and the more recent arrivals, Mark Lantz and Teddy Loeliger. They helped me extend my knowledge of microfabrication technologies and showed me how fascinating research can be. Working in such a friendly and heterogeneous group was a real pleasure and a great experience.

Interacting with multidisciplinary colleagues has been a great opportunity for me to expand my horizon and to find sometimes more original solutions as well as getting a better understanding of physical and chemical phenomena that were not always clear from my engineer's point of view. In this context, it is a pleasure to acknowledge Marko Baller, Rüdiger Berger, René Beyeler, Emmanuel Delamarche, Roland Germann, David Juncker, Ingmar Meijer, Christophe Rossel, and Heinz Schmid. I am also very thankful to all my colleagues in Rüschlikon for most pleasurable working conditions and valuable help. Special thank is given to Charlotte Bolliger, Nicola Gustafsson, Janet Kägi and Lilli-Marie Pavka of the publications department for helping me publish my results.

During this work, I had the opportunity to interact with many people from different groups, to exchange knowledge, and to develop new ideas. I thank especially

◇ Prof. Dario Anselmetti, now Prof. at the University of Bielefeld in Germany, for sharing with me his expertise in the imaging of biological samples using AFM. Thank you for having taken such nice images with the photoplastic cantilevers.

◇ Urs Staufer and Wilfried Noell from the Institute of Microtechnology of the University of Neuchâtel for their help in developing new concepts for microfabricated SNOM probes.

◇ Prof. Fabienne Marquis-Weible, Maria Pilar-Bernal, Abdellah Boulouz, and Thomas Cueni of the Institute of Applied Optics of the Swiss Federal Institute of Technology in Lausanne for their contributions in developing the photoplastic SNOM probe.

◇ Hubert Lorenz of Mimotec SA in Sion for sharing his knowledge on the SU-8 photoresist.

Prof. F. Marquis-Weible, Prof. P. Renaud, Prof. A. Stemmer, and P. Vettiger are gratefully acknowledged for their acceptance to take part in my defense jury.

Graham Cross, Hugo Rothuizen and Charlotte Bolliger are deeply thanked for their help in manuscript correction and preparation.

Thank also to my friends outside IBM, who helped me relax in the critical phases. Last but not least I would like to thank my family and Kathy wholeheartedly for their unwavering support.

List of Publications

G. Genolet, J. Brugger, M. Despont, U. Drechsler, P. Vettiger, N. F. de Rooij, and D. Anselmetti, *Soft, entirely photoplastic probes for scanning force microscopy*, Rev. Sci. Instrum. **70**, (1999), 2398-2401.

G. Genolet, M. Despont, P. Vettiger, D. Anselmetti, and N. F. de Rooij, *All-photoplastic, soft cantilever cassette probe for scanning force microscopy*, J. Vac. Technol. B **18**, (2000), 617-620.

G. Genolet, T. Cueni, M.-P. Bernal, M. Despont, U. Staufer, W. Noell, P. Vettiger, F. Marquis-Weible, and N. F. de Rooij, *Novel micromachined photoplastic probe for scanning near-field optical microscopy*, Proc. of Eurosensors XIV, The 14^{th} European Conference on Solid-State Transducers, August 27-30, 2000, Copenhagen, Denmark, 641-644.

G. Genolet, M. Despont, P. Vettiger, and N. F. de Rooij, *Micromachined Photoplatic Probes for Scanning Probe Microscopy*, invited paper in Sensors Update 9, **1**, (2001), 3-19, Wiley–VCH.

G. Genolet, M. Despont, P. Vettiger, U. Staufer, W. Noell, N. F. de Rooij, T. Cueni, M.-P. Bernal, and F. Marquis-Weible, *Micromachined photoplastic probe for scanning near-field optical microscopy*, to be published in Rev. Sci. Instrum.

G.-A. Racine, G. Genolet, P.-A. Clerc, M. Despont, P. Vettiger, and N.F. de Rooij, *Porous Silicon Sacrificial Layer Technique for the Fabrication of Free Standing Membrane Resonators and Cantilever Arrays*, Proc. of Eurosensors XI, The 11^{th} European Conference on Solid-State Transducers, September 21-24, 1997, Warsaw, Poland, 285-288.

H. Rothuizen, U. Drechsler, G. Genolet, W. Häberle, M. Lutwyche, R. Stutz, R. Widmer, and P. Vettiger, *Fabrication of a Micromachined Magnetic X/Y/Z Scanner for Parallel Scanning Probe Applications*, Microelectronic Engineering **53**, (2000), 509-512.

M.-P. Bernal, T. Cueni, G. Genolet, M. Despont, P. Vettiger, and F. Marquis-Weible, *Novel micromachined photoplastic near-field probes*, Proc. of NFO-6, The 6^{th} International Conference on Near Field Optics and Related Techniques, August 27-31, 2000, Twente, the Netherlands, 58.

Curriculum Vitae

Grégoire GENOLET
born 31st March 1973 in Sion (VS)
Swiss nationality

Education

1998 — present

Institute of Microtechnology, University of Neuchâtel, Switzerland, and IBM Research Division, Zurich Research Laboratory, Switzerland.
Doctoral thesis on *New Photoplastic Fabrication Techniques and Devices based on High Aspect Ratio Photoresist.*
Advisor: Prof. N. F. de Rooij (IMT-NE).

04/1997 — 09/1997

IBM Zurich Research Laboratory, Micro-/nanomechanics group.
Work related with porous silicon.

1992 — 04/1997

Degree in Microengineering from the Swiss Federal Institute of Technology, Lausanne. Orientation: Integrated Product.
Diploma work entitled: *Microfabrication de microstructures en utilisant le silicium poreux comme couche sacrificielle.*

1987 — 1992

Maturity type C, Lyçée-Collège des Creusets, Sion.

1979 — 1987

Primary and Secondary School, Sion.

Award

Best Paper Award, first prize at Eurosensors XIV, the 14th European Conference on Solid-State Transducers, August 27-30, 2000, Copenhagen, Denmark.